SYHTHESIS AND OPTICAL PROPERTIES OF RARE EARTH SULFIDES AND OXYSULFIDES

by

ADRIANA PAOLA SOTELO MUNOZ

Presented to the Faculty of the Graduate School of

The University of Texas at Arlington in Partial Fulfillment

of the Requirements

for the Degree of

DOCTOR OF PHILOSOPHY

THE UNIVERSITY OF TEXAS AT ARLINGTON

August 2019

Acknowledgements

The past five years as a graduate student have been a very gratifying experience, in part, because of family and friends, scientists, and collaborators with whom I have interacted.

First and foremost I have to thank God for being my strength and guide during my graduate studies. Without Him, I would not have had the wisdom or the physical ability to do so. Also I would like to express my deep gratitude to my husband, Alejandro Pino who always encouraged me to pursue my education and career and took care of my little and precious baby Salome during many nights so that I had more rest to be able to finish my dissertation.

Also I am very thankful for many supportive family members and friends, especially my mother Elvia Munoz, the person I am today is only possible because of all the sacrifice she has made in their life. I would like to thank my brother Manuel Sotelo and sister Maritza Sotelo for being incredible to me and always being there when I need them.

There are many persons at the University of Texas at Arlington to whom I am indebted. My advisor, Dr. Robin Macaluso for her excellent mentorship and support during these years. I greatly appreciate the time she spent sharing her knowledge with me and also encouraging me to pursue my scientific interest, leading by example to motivate me to keep working hard and learning new things every day. I acknowledge Dr. Delphine Gout, the Facility Manager of Shimadzu Institute Center for Nanostructured Materials for encouraging me not just to use the diffractometer for routine data collection, but to analyze the data to solve crystal structures. I must also thank many collaborators: Dr. Krishnan Rajeshwar, Dr. Csaba Janáky, Dr. Claudia Longo, Dr. Mohammad N. Huda and Dr. Miguel T. Galante.

I owe a great deal of gratitude to my research colleagues for all their support, suggestion, invaluable discussions and friendship. Also I would like to thank Dr. Diego Lopez, Mohammad Kabir Hossain, Hori Sarker, Farinaz Firouzan, Dr. Enrique Barragan, Susana Aguirre-Medel, Melissa Orr, Michael Moore, Wafa Tony and Wendy for the camaraderie and support.

I am also very thankful to all my Dissertation Committee Members: Dr. Rasika Dias, Dr. Junha Jeon and Dr. Peter Kroll for their guidance and suggestions to improve the quality of my work.

I would like to extend my gratitude to UT Arlington's staff because without their help, all of this would have not been possible. I would like to thank the Administrative Assistants, Mrs. Jill Howard, Mrs, Debbie Cooke and the graduate program coordinator Stephanie Henry for all their kind help. My great gratefulness also goes to Dr. Brian Edwards and Dr. Roy McDougal for their training and support with the instrumentation. I would like also to thank to our undergraduate lab coordinators Drs. William Cleaver and Cynthia Griffith for their advice and guidance for teaching duties; as well as the Stockroom Supervisor, Mrs. Beth Klimek, for always kindly providing me with all the supplies I needed for my experiments.

May 23, 2019

Abstract

SYHTHESIS AND OPTICAL PROPERTIES OF RARE EARTH SULFIDES AND OXYSULFIDES

Adriana Paola Sotelo Munoz, PhD

The University of Texas at Arlington, 2019

Supervising Professor: Robin T. Macaluso

Ternary and quaternary rare earth chalcogenides have gained prominence in recent years, especially because of their wide array of crystal structures and interesting physical properties attributed to the presence of *f*-electrons [1-3] Among all rare earth chalcogenides, rare earth sulfides of the Ln_2S_3 family has been explored (Rare earth, Ln) in the industry of pigment, thermoelectric and ceramics, however, the study of their *f*-electron chemistry and their photoactivity have not been investigated. In this vein, the work described in this dissertation investigates the structures and role of *f*- electrons in optical properties of the beta and gamma polymorphs of Ln_2S_3. This research is a starting point to enlarge the library of chalcogenides available for optical and electronic applications, especially for applications related to energy conversion where ternary and quaternary chalcogenides have gained prominence in the last years.

Chapter 1 surveys the prior literature of chalcogenides, describing synthesis, crystal structure, applications and significance of rare earth sulfides.

In **Chapter 2,** a greener solid-state synthesis method, not requiring the flow of harmful gases, was applied for the synthesis of the red-orange compound $CaCe_2S_4$. This compound was first synthesized as an inorganic pigment, However, in this chapter the photoelectrochemical behavior is studied for the first time. X-ray diffraction showed that this compound adopts the cubic Th_3P_4 structure (γ-polymorph) with a = 8.614(3) Å. The optical band gap was determined to be ~ 2.1 eV and photoelectrochemical studies showed that $CaCe_2S_4$ is an *n*-type semiconductor.

Chapter 3 presents the study of the role of *f*-electrons over optical properties in the solution solution, $Ca(La_{1-x}Ce_x)_2S_4$ ($0 \leq x \leq 1$). These quaternary compounds showed progressive variations in color ranging from grey in $CaLa_2S_4$ to orange-red in $CaCe_2S_4$. Neutron scattering and synchrotron X-ray revealed that samples maintain the cubic Th_3P_4 structure type described in previous chapter. Optical characterization and DFT calculations showed a shrinking of the energy band gap from the UV to visible range with the progressive addition of cerium into the host $CaLa_2S_4$ structure.

Finally, in **Chapter 4** the synthesis and optical characterization of lanthanide oxysulfides with the composition $(La_{1-x}Ce_x)_{10}OS_{14}$ ($0<x<1$) are described. Powder and single crystal samples were obtained by heating the binary Ln_2S_3 (Ln= La, Ce) compounds. The optical band gaps of $(La_{1-x}Ce_x)_{10}OS_{14}$ are in the range of 1.7 to 2.5 Ev indicating wide band gap semiconductors. Photoluminescence in all samples show red line emission and a red-shift of the lowest energy photoluminescence band as cerium was added into the structure.

References

1. Gschneidner, K. A., Preparation and processing of rare earth chalcogenides. *J Mater Eng Perform* **1998,** *7* (5), 656-660.
2. Flahaut, J., Handbook on the physics and chemistry of rare earths. In *Chapter 31 Sulfides, Selenides and Tellurides*, Elsevier **1979;** Vol. 4, pp 1-88.
3. Hulliger, F.; Vogt, O., Magnetic investigations of new ternary rare-earth chalcogenides. *Phys Lett.* **1966,** *21* (2), 138-140.

Table of Contents

List of Illustrations

List of Tables

Chapter 1 Introduction

1.1 Metal chalcogenides

Metal chalcogenides are compounds consisting of one chalcogenide anion (S, Se, Te) and one metal cation, have become the focal point for a wide range of interesting advanced material applications in renewable energy and computational field.[1-10] These include fuel cell systems,[1-2] photovoltaic,[3-6] thermoelectric (TE) generators,[7-8] lition batteries,[9] and even superconductors and topological insulators.[10] Examples include $CuInGa(S,Se)_2$ and CdTe, which are already commercialized for large-scale photovoltaic manufacturing, offering stable and efficient (above 10%) photovoltaic modules fabricated by scalable thin-film technologies.[11] Alloys such as those in the Fe-Ni-S phase space have shown promise in the search for non-noble metal hydrogen evolution reaction electrocatalysis and the combination of low temperature superconductivity, charge density waves, and transverse fluctuation diamagnetism observed in $NbSe_2$.[12] Although these systems have been the focus of numerous studies, they have received little attention compared with metal oxides. In particular, a subset of metal chalcogenides, namely, rare-earth chalcogenides, are in need of additional study.

1.2 Rare earth chalcogenides

Chalcogenides containing rare-earth elements are particularly interesting because of their diverse structural chemistry and fascinating physical properties, related to the chemistry of 4*f* electrons, that include but are not limited to magnetism, superconductivity, fluorescence, TE and nonlinear optical (NLO).[13-16] As examples of remarkable discoveries of new rare-earth chalcogenides in recent years, $La_8Sb_2S_{15}$ shows second harmonic generation with the intensities of 1.2 times that of the commercially used IR NLO material $AgGaS_2$ at 2.05 μm laser. However, no obvious SHG signal for the Pr-analog was observed which mean that the choice of rare earth metal can profoundly impact the properties; [17-18] Similar phenomena occurred in the series of Ln_4InSbS_9 (Ln=La, Pr, Nd, Sm)[19]and $Ba_2LnInSe_5$ (Ln=Y, Nd, Sm, Gd, Dy, Er)[20] compounds.

Recently, many multinary chalcogenides containing d-block transition metal (M) and *f*-block rare earth elements have been synthesized and exhibited intriguing structures and physical

properties. For example, $ALnMQ_3$ (A=Rb, Cs; Ln=rare-earth metal; M=Mn, Co, Zn, Cd, Hg; Q=S, Se, Te) are magnetic semiconductors offering flexibility in band gap engineering by controlling the composition and crystal orientation.[21-23]

A special feature of rare earth elements is that they can form different bonding environments with chalcogenides. This offers an ideal situation for studies that correlate changes in structural and physical properties with chemical substitution. An example of the application of substitution chemistry in these systems is the syntheses and optical band gap studies of the $ALnMQ_3$ (A = Cs, Rb; Ln = La-Nd, Sm-Yb, Y; M = Mn, Zn, Cd, Hg; Q = S, Se, Te) [24-25] [26-27]compounds where combined substitutions on the Ln, M, and Q sites can change the band gap from 1.6 eV to 2.63 eV.

Chemical substitution of different lanthanide ions is also possible in the binary chalcogenide systems. Mixed lanthanide systems take the general form of ordered solids or solid solutions of the binary structure types. These compounds often display interesting properties different from those of the binary materials, although they have been minimally studied. Investigations have been limited to the magnetic susceptibilities of $ErLn_2Q_4$,[28] β-$LaYbS_3$, and $LnYbSe_3$ (Ln = La, Ce, Pr, Nd, and Sm)[27]. More recently the magnetic susceptibility and optical properties of the ordered γ-LnLn'S_3 (Ln = La, Ce; Ln' = Er, Tm, Yb) [29-30]have been investigated.

1.3 Rare earth sulfides

The rare-earth sulfide materials constitute a special category of the rare earth chalcogenides which have shown interesting physical and chemical properties such as excellent thermal stability, strength and infrared (IR) transmission characteristics The main interest in the study of these class of chalcogenides lies in their complex structural chemistry and in the related physical properties[31].

Several different structure types occur and nonstoichiometry and polymorphism are quite common.[31-32] In the case of the lanthanides sesquisulfides (Ln_2S_3) up to five different crystal structures, depending primarily on ionic radius and annealing temperature have been reported. These five crystal structures are referred to as α, β, γ, δ, and ε polymorphs. The structure and crystal chemistry have been studied intensively particularly by Flahaut and his colleagues.[33]

The α-polymorph sesquisulfide[16] structure is an orthorhombic system with a space group of Pnma. The unit cell contains four formula units with two inequivalent rare earth ions. Figure 1-1 (left) shows the two different kinds of Ln–S polyhedrons. The coordination polyhedra $(Ln1)S_8$ and $(Ln2)S_7$ have the shapes of a bicapped trigonal prism and a distorted monocapped octahedron, respectively.

The β-phase was discovered to be an oxysulfide with the formula $Ln_{10}OS_{14}$.[34] This is the thermodynamically preferred phase at temperatures around 900°C. The crystal structure for the beta phase is tetragonal with space group I41/acd. The structure is built by the motifs of bicapped trigonal prisms of LnS_8 and $LnOS_7$. Rare earth atoms are located in three different atomic positions (Ln1, Ln2 and Ln3) and all coordinated by eight anions forming bicapped-trigonal prisms. These polyhedrons can be observed in figure 1-1 middle. Moreover, the β polymorph at higher temperature is transformed to γ phase which exists in all sesquisulfides from La to Lu. This polymorph is a cubic structure with a space group of *I*-43d adopting a modified Th_3P_4 structure with a decreased Ln site occupancy, consequently, its formula is also written as $Ln_{2.67}V_{0.33}S_4$ (V: vacancy, where $V_{0.33}$ represents the maximum number of metal vacancies); the vacancy can be occupied by an Ln composition up to Ln_3S_4. In this structure the rare earth cations are located on the 12a and sulfur anions in the 16*c* positions. Each rare earth cation is coordinated by eight sulfur anions forming a triangular dodecahedron as is shown in fig 1.1 right. For rare earth element with z<67, this is the last structure they can form.

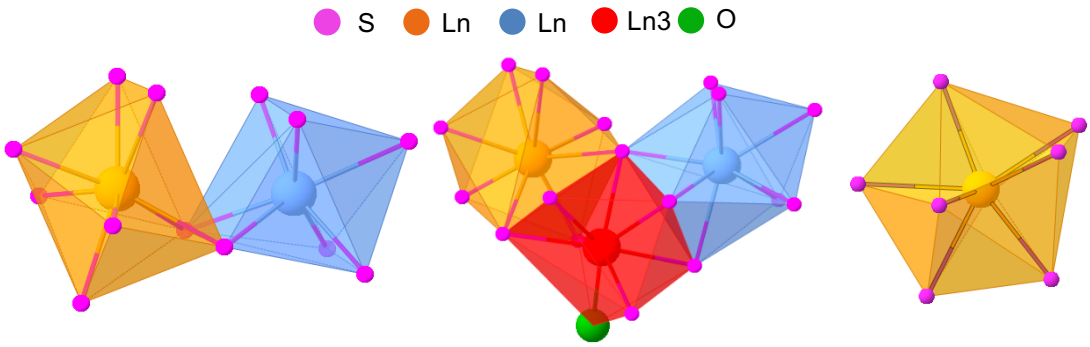

Figure 1-1. Local environments of Ln atoms in the three polymorphs (α, β, γ) of Ln_2S_3. Graphics prepared by CrystalMaker® using crystallographic data from ICDD. Card numbers: 622026, 69740, 79918 respectively.

Sesquisulfides from Dy to Lu exist in the monoclinic δ-polymorph with 6- and 7 coordinate rare earth ions.[35-36]The heavier lanthanides (Tm to Lu) typically give sesquisulfides of the ε-form, having the rhombohedral corundum-type structure, with the lanthanides being 6-coordinated,[37] studies in these two polymorphs have shown intereting properties however in the present thesis we will be concerning about the (α, β, γ) polymorphs.

1.4 Synthesis of rare earth sulfides

Rare earth sulfides can be synthesized from direct reaction of elements in stoichiometric ratios in a sealed tube or reductive gas sulfurization (H_2S or CS_2 gases[38-39]) of rare-earth oxide at temperatures ranging from 600 to 1200 °C. [31-32, 40] However, there are some difficulties for this method because it is difficult to control the partial pressure of rare earths and sulfur to obtain the desired composition and because of the formation of oxysulfide impurities from the oxidation of the rare earth surface or by reaction with the walls of the experimental container (quartz tube).

To improve this method, our lab has synthesized some rare earth sesquisulfides using a tantalum foil where Ln_2O_2S was also formed in the initial stage of reaction, however, the oxygen impurity phase decreased using the foil which avoid reaction with the walls of the quartz tube. Therefore, this methodology was used for all the experimental part of this thesis.

Application of Rare Earth sulfides

Rare earth sulfides have been widely used for luminescent,[41] magnetic and electronic materials [42]. Some examples of its applicability in the industry include refractory, pigment and thermoelectric material.

CeS, Ce_3S_4 and Ce_2S_3, have been consider as refractory materials.[39, 43-44] Their high melting points and high stability to thermal shock make them valuable in manufacturing as high temperature crucibles and for other refractory uses. In the pigment industry, rare earth sesquisulfides doped with at least one alkali/alkaline earth metal have shown good characteristics for the coloration of cosmetic, plastics, paints and rubbers. Novel environmental friendly

colorant/pigment has been prepared via precipitation technology. Similarly, the solid solution Ln_2S_3-Ln_3S_4 (Ln = La, Ce, Pr, Gd, Dy) with cubic structure have been investigated for high temperature thermoelectric conversion materials.[45]

Based on the above analysis, specifically in that the structures and electronic properties of rare earth sulfides are tunable, our interest relies in extending the library of chalcogenide materials available for electronic applications. In this vein the focus of this dissertation is the synthesis and study of rare earth sulfide compounds of the Ln_2S_3 family, exploring the role of *f* effects in their optical and photoelectrochemical properties.

References

4. Feng, Y. J.; Alonso-Vante, N., Nonprecious metal catalysts for the molecular oxygen-reduction reaction. *Phys. Status Solidi B* **2008,** *245*, 1792-1806.
5. Morozan, A.; Jousselme, B.; Palacin, S., Low-platinum and platinum-free catalysts for the oxygen reduction reaction at fuel cell cathodes. *Energy Environ. Sci.* **2011,** *4*, 1238-1254.
6. Bernechea, M.; Miller, N. C.; Xercavins, G.; So, D.; Stavrinadis, A.; Konstantatos, G., Solution-processed solar cells based on environmentally friendly $AgBiS_2$ nanocrystals. *Nat. Photonics* **2016,** *10*, 521-+.
7. Zhou, H. P.; Hsu, W. C.; Duan, H. S.; Bob, B.; Yang, W. B.; Song, T. B.; Hsu, C. J.; Yang, Y., CZTS nanocrystals: a promising approach for next generation thin film photovoltaics. *Energy & Environ. Sci* **2013,** *6*, 2822-2838.
8. Roelofs, K. E.; Herron, S. M.; Bent, S. F., Increased quantum dot loading by pH control reduces interfacial recombination in quantum-dot-sensitized solar cells. *Acs Nano* **2015,** *9*, 8321-8334.
9. Kim, D. H.; Lee, S. J.; Park, M. S.; Kang, J. K.; Heo, J. H.; Im, S. H.; Sung, S. J., Highly reproducible planar Sb_2S_3-sensitized solar cells based on atomic layer deposition. *Nanoscale* **2014,** *6*, 14549-14554.
10. Gao, M. R.; Xu, Y. F.; Jiang, J.; Yu, S. H., Nanostructured metal chalcogenides: synthesis, modification, and applications in energy conversion and storage devices. *Chem. Soc. Rev.* **2013,** *42*, 2986-3017.
11. Fan, F. J.; Wu, L.; Yu, S. H., Energetic I-III-VI2 and I-2-II-IV-VI4 nanocrystals: synthesis, photovoltaic and thermoelectric applications. *Energy Environ. Sci.* **2014,** *7*, 190-208.
12. Zhang, J.; Zhang, Z.; Sun, Y.; Zhang, C.; Tao, X., Anisotropic thermal properties of the polar crystal $Cs_2TeMo_3O_{12}$. *J. Solid State Chem.* **2012,** *195*, 120-124.
13. Hwang, H.; Kim, H.; Cho, J., MoS_2 Nanoplates Consisting of Disordered Graphene-like Layers for High Rate Lithium Battery Anode Materials. *Nano Lett.* **2011,** *11*, 4826-4830.
14. Yoon, H.; Na, S. H.; Choi, J. Y.; Kim, M. W.; Kim, H.; An, H. S.; Min, B. K.; Ahn, S.; Yun, J. H.; Gwak, J.; Yoon, K.; Kolekar, S. S.; van Hest, M.; Al-Deyab, S. S.; Swihart, M. T.; Yoon, S. S., Carbon- and oxygen-free $Cu(InGa)(SSe)_2$ solar cell with a 4.63% conversion efficiency by electrostatic spray deposition. *ACS Appl. Mater. Interfaces* **2014,** *6* , 8369-8377.
15. Gschneidner, K. A., Preparation and processing of rare earth chalcogenides. *J Mater Eng Perform* **1998,** *7*, 656-660.
16. Yin, W.; Zhang, D.; Zhou, M.; Iyer, A. K.; Pöhls, J.-H.; Yao, J.; Mar, A., Quaternary rare-earth selenides $Ba_2REGaSe_5$ and $Ba_2REInSe_5$. *J. Solid State Chem.* **2018,** *265*, 167-175.
17. Kanatzidis, M. G., Discovery-synthesis, design, and prediction of chalcogenide phases. *Inorg. Chem.* **2017,** *56*, 3158-3173.
18. Flahaut, J.; Guittard, M.; Patrie, M.; Pardo, M. P.; Golabi, S. M.; Domange, L., Phases cubiques type Th_3P_4 dans les sulfures les seleniures et les tellurures L_2X_3 et L_3X_4 des terres rares et dans leurs combinaisons ML_2X_4 avec les sulfures et seleniures MX de calcium strontium et baryum . Formation et proprietes cristallines. *Acta Crystallogr. A* **1965**, 14-19.
19. Sleight, A. W.; Prewitt, C. T., Crystal chemistry of rare earth sesquisulfides. *Inorg. Chem.* **1968,** *7*, 2282-&.
20. Zhao, H. J.; Zhong, X. A., Synthesis, crystal structure, and optical properties of the noncentrosymmetric sulfide $Ce_8Sb_2S_{15}$. *J. Solid State Chem.* **2017,** *251*, 65-69.
21. Zhao, H.-J.; Zhou, L.-J., A series of noncentrosymmetric antimony sulfides $Ln_8Sb_2S_{15}$ (Ln = La, Pr, Nd) – Syntheses, crystal and electronic structures, and NLO properties. *Eur. J. Inorg. Chem.* **2015,** *2015*, 964-968.

22. Zhao, H.-J.; Zhang, Y.-F.; Chen, L., Strong Kleinman-Forbidden Second Harmonic Generation in Chiral Sulfide: La_4InSbS_9. *J. Am. Chem. Soc.* **2012,** *134*, 1993-1995.
23. Yin, W.; Feng, K.; Wang, W.; Shi, Y.; Hao, W.; Yao, J.; Wu, Y., Syntheses, Structures, Optical and Magnetic Properties of Ba_2MLnSe_5 (M = Ga, In; Ln = Y, Nd, Sm, Gd, Dy, Er). *Inorg. Chem.* **2012,** *51*, 6860-6867.
24. Yao, J.; Deng, B.; Sherry, L. J.; McFarland, A. D.; Ellis, D. E.; Van Duyne, R. P.; Ibers, J. A., Syntheses, structure, some band gaps, and electronic structures of $CsLnZnTe_3$ (Ln = La, Pr, Nd, Sm, Gd, Tb, Dy, Ho, Er, Tm, Y). *Inorg. Chem.* **2004,** *43*, 7735-7740.
25. Chan, G. H., Sherry, L. J., Van Duyne, R. P. and Ibers, J. A, syntheses, crystal structures, and optical and magnetic properties of some $CsLnCoQ_3$ compounds (Ln = Tm and Yb, Q = S; Ln = Ho and Yb, Q = Se). *Z. anorg. allg. Chem* **2007,** *633*, 1343-1348.
26. Mitchell, K.; Huang, F. Q.; McFarland, A. D.; Haynes, C. L.; Somers, R. C.; Van Duyne, R. P.; Ibers, J. A., The $CsLnMSe_3$ semiconductors (Ln = Rare-Earth Element, Y; M = Zn, Cd, Hg). *Inorg. Chem.* **2003,** *42* , 4109-4116.
27. Schleid, T.; Lissner, F., Single-crystals of ■TM_2S_3 and ■YB_2S_3. *J. Alloys Compd* **1992,** *189*, 69-74.
28. Mitchell, K.; Huang, F. Q.; Caspi, E. N.; McFarland, A. D.; Haynes, C. L.; Somers, R. C.; Jorgensen, J. D.; Van Duyne, R. P.; Ibers, J. A., Syntheses, structure, and selected physical properties of $CsLnMnSe_{(3)}$ (Ln = Sm, Gd, Tb, Dy, Ho, Er, Tm, Yb, Y) and $AYbZnQ_3$ (A = Rb, Cs; Q = S, Se, Te). *Inorg. Chem.* **2004,** *43*, 1082-1089.
29. Mitchell, K.; Haynes, C. L.; McFarland, A. D.; Van Duyne, R. P.; Ibers, J. A., Tuning of optical band gaps: Syntheses, structures, magnetic properties, and optical properties of $CsLnZnSe_3$ (Ln = Sm, Tb, Dy, Ho, Er, Tm, Yb, and Y). *Inorg. Chem.* **2002,** *41*, 1199-1204.
30. Mitchell, K.; Somers, R. C.; Huang, F. Q.; Ibers, J. A., Syntheses, structure, and magnetic properties of several $LnYbQ_3$ chalcogenides, Q = S, Se. *J. Solid State Chem.* **2004,** *177*, 709-713.
31. Hulliger, F.; Vogt, O., Magnetic investigations of new ternary rare-earth chalcogenides. *Phys Lett.* **1966,** *21* (2), 138-140.
32. Carre, D.; Flahaut, J.; Khodadad, P.; Laruelle, P.; Rodier, N.; Vantien, V., Comparative study of crystalline-structures of sulfides containing 2 III-a elements (scandium, yttrium and lanthanides). *J. Solid State Chem.* **1973,** *7*, 321-336.
33. Rodier, N.; Laruelle, P.; Flahaut, J., A new series of rare earth and yttrium sesquisulfides with scandium sesquisulfide. *Comptes Rendus Acad. Sci.* **1969,** *269*, 1391-1395.
34. Flahaut, J., Handbook on the physics and chemistry of rare earths. In *Chapter 31 Sulfides, Selenides and Tellurides*, Elsevier **1979**, 4, pp 1-88.
35. Flahaut, J., Bull. Soc. Chim. Fr. *Bulletin De La Societe Chimique De France* **1966,** *2*, 802-804.
36. Flahaut, J.; Domange, L.; Patrie, M., Combinaisons formees par les sulfures des elements du groupe des terres rares. Vue densemble sur les systemes formes par le sulfure dyttrium avec les sulfures des elements divalents. *Bull. Soc. Chim. Fr* **1962,** *1*, 159-160.
37. Besancon, P.; Carre, D.; Laruelle, P., Mechanism of solid-solutions of rare-earth oxysulfides $La_{10}S_{15-x}O_x$. *Acta Crystallogr. B* **1973,** *B 29*, 1064-1066.
38. Borisov, S. V.; Podberezskaya, N. V.; Pervukhina, N. V.; Magarill, S. K., Crystal structure of polymorphous modifications of Tm_2S_3 and related compounds. *J. Struct. Chem.* **1998,** *39*, 543-548.
39. Landa-Canovas, A. R.; Amador, U.; Otero-Diaz, L. C., Crystal structure and microstructure of delta-Er_2S_3. *J. Alloys Compd* **2001,** *323*, 91-96.
40. Akhmedova, N. R.; Aliev, O. M.; Bakhtiyarly, I. B., Interaction in the Yb_2S_3-In_2S_3 system. *Russ J Inorg Chem* **2006,** *51*, 478-483.

41. Ohta, M.; Hirai, S.; Kuzuya, T., Preparation and Thermoelectric Properties of $LaGd_{1+3}$ and $SmGd_{1+x}S_3$. *J. Electron. Mater.* **2011,** *40*, 537-542.
42. Hirai, S.; Shimakage, K.; Saitou, Y.; Nishimura, T.; Uemura, Y.; Mitomo, H.; Brewer, L., Synthesis and sintering of cerium(III) sulfide powders. *J Am Ceram Soc.* **1998,** *81*, 145-151.
43. Flahaut, J.; Attal, E., Sur loxysulfure et les sulfures de cerium. *Comptes Rendus Acad. Sci* **1954,** *238*, 682-684.
44. Mauricot, R.; DexpertGhys, J.; Evain, M., Photoluminescence of the undoped gamma-Ln_2S_3 and doped gamma- Na Ln_2S_3 rare earth sulfides (Ln=La,Ce). *J. Lumin.* **1996,** *69*, 41-48.
45. Jary, V.; Havlak, L.; Barta, J.; Buryi, M.; Mihokova, E.; Rejman, M.; Laguta, V.; Nikl, M., Optical, Structural and Paramagnetic Properties of Eu-Doped Ternary Sulfides $ALnS_2$ (A = Na, K, Rb; Ln = La, Gd, Lu, Y). *Materials* **2015,** *8*, 6978-6998.
46. Eastman, E. D.; Brewer, L.; Bromley, L. A.; Gilles, P. W.; Lofgren, N. L., Preparation and properties of refractory cerium sulfides. *J. Am. Chem. Soc.* **1950,** *72*, 2248-2250.
47. Eastman, E. D.; Brewer, L.; Bromley, L. A.; Gilles, P. W.; Lofgren, N. L., Preparation and tests of refractory sulfide crucibles. *J Am Ceram Soc.* **1951,** *34*, 128-134.
48. Wood, C., Materials for thermoelectric energy-conversion. *Rep. Prog. Phys.* **1988,** *51*, 459-539.

Chapter 2

Ternary Rare Earth Sulfide $CaCe_2S_4$: Synthesis and Characterization of Stability, Structure, and Photoelectrochemical Properties in Aqueous Media

Abstract

A red-orange rare earth ternary chalcogenide, $CaCe_2S_4$, was prepared in powder form by solid-state synthesis. The structural details of this compound were determined by powder X-ray diffraction. The optical band gap of $CaCe_2S_4$ was determined by diffuse reflectance spectroscopy (DRS) to be ~2.1 eV, consistent with the observed red-orange color. Quantitative colorimetry measurements also support the observed color and band gap of $CaCe_2S_4$. Both direct and indirect optical transitions were gleaned from Tauc analyses of the DRS data. Photoelectrochemistry experiments on $CaCe_2S_4$ films showed n-type semiconductor behavior. Analyses of these data via the Butler-Gärtner model afforded a flat-band potential of -0.33 V (vs. Ag/AgCl/KCl 4 M) in ~pH 9 aqueous sulfite electrolyte. The potential and limitations of this material for solar water splitting and photocatalytic environmental remediation (e.g., dye photodegradation) are finally presented against the backdrop of its photoelectrochemical stability and surface hole transfer kinetics in aqueous electrolytes.

2.1 Introduction

Transition metal chalcogenides are important in a wide spectrum of technology applications such as solar cells, fuel cells, hydrogen generation, lubrication etc. Binary metal sulfides, such as exfoliated nanoparticles of layered sulfides MoS_2 and WS_2 have emerged as promising materials in this regard.[1-8] Of the binary sulfides, perhaps the most thoroughly studied in photoelectrochemical (PEC) and photocatalytic applications is CdS [9]. Its band gap is ~2.4 eV and absorbs wavelengths up to 510 nm. Its valence band edge position is compatible with the requirements for water photooxidation[10] and photocatalytic environmental remediation.[11] However, a major drawback of this material, in terms of practical applicability, is anodic photocorrosion in aqueous media. [12-13]

Ternary (and quaternary) chalcogenides have gained prominence in recent years, especially for applications related to photovoltaic solar conversion. Examples include copper indium gallium sulfide and selenide (CIGS) and copper zinc tin sulfide (CZTS).[14] Alloys such as those in the Fe-Ni-S phase space (e.g., pentlandite or FeNiS) have also shown promise in the search for non-noble metal hydrogen evolution reaction (HER) electrocatalysts.[15]

In this vein, we investigated the ternary sulfide, $CaCe_2S_4$; our results are presented in what follows. This compound was first synthesized because of its relationship to the binary γ-Ln_2S_3 (Ln = La, Ce) prototype as an inorganic pigment; γ-Ln_2S_3 and $CaLn_2S_4$ adopt the Th_3P_4 structure type with the $I\bar{4}3d$ space group. Yellow, red, and green colors have been observed for $CaLn_2S_4$ with Ln = Ce, Pr, and Nd, respectively.[11,16] The optical transition in rare-earth derived chalcogenides is generally accepted as originating from electronic transitions involving localized 4f → 5d orbitals.[17-21] However, the PEC behavior of rare earth-derived chalcogenides such as γ-Ln_2S_3 and $CaLn_2S_4$, has not been investigated, at least to our knowledge. Thus, we describe in this exploratory study, the solid-state synthesis of $CaCe_2S_4$ in powder form and investigate its structural aspects, optical, and PEC behavior. For the PEC measurements, the powder was transferred to Ti substrate electrodes in thin film form. The proclivity toward photocorrosion of $CaCe_2S_4$ was tested in aqueous sulfite and polysulfide electrolytes, and compared with the CdS

benchmark. Finally, thermal analyses of $CaCe_2S_4$ showed the material to be stable at temperatures up to at least ~450°C.

2.2 Materials and Methods

2.2.1 *Synthesis*

Powder samples of $CaCe_2S_4$ were prepared from a stoichiometric ratio of CaS and Ce_2S_3 by grinding the mixture with an agate mortar and pestle. The powders were ground inside a dry box with ultra-high purity argon circulation and then placed in tantalum foil or a graphite crucible. The foil (or crucible) and its contents were placed inside a fused silica ampoule and sealed under vacuum. The ampoule was heated at 7 °C/h to 1100 °C, where it dwelled for 100 h, and then cooled to 25 °C at 20 °C/min. The product was visibly red-orange. Typical yields based on mass were ~90.0%.

2.2.2 *Structural Characterization*

2.2.2.1 Powder X-Ray Diffraction

High resolution synchrotron powder diffraction data were collected using Beamline 11-BM at the Advanced Photon Source, Argonne National Laboratory using an average wavelength of 0.414555 Å. Discrete detectors covering an angular range from -6 to 16º 2θ were scanned over a 34º 2θ range, with data points collected every 0.001º 2θ at a scan speed of 0.01º/s. The 11-BM instrument uses x-ray optics with two platinum-striped mirrors and a double-crystal Si(111) monochromator, where the second crystal has an adjustable sagittal bend. The data were collected at room temperature. X'Pert Plus software package [22] was employed to analyze and refine the synchrotron data. A previously established structural model of $CaCe_2S_4$ ($I\bar{4}3d$) [16] was used as a starting model for this refinement. Global profile refinement parameters included a scale factor, a specimen displacement parameter and parameters of a peak shape function (U, V, W) using the Caglioti function [23] for the peak full-width at half-maximum (FWHM). The peak shape was fit using a pseudo-Voigt function [24] and the background was manually adjusted. Refinement parameters for the structure were unit cell parameters, site occupancies, and anisotropic/isotropic displacement parameters.

2.2.2.2 Elemental Analysis

Since graphite crucibles were used in some cases, elemental analysis (Perkin Elmer, PE 2400 Series-II CHNS/O Analyzer) was employed to check for trace amounts of C. There were no detectable amounts of carbon nor were hydrogen or nitrogen detected.

2.2.2.3 Electron Microscopy

Electron dispersive spectroscopy measurements were performed with a Hitachi S-3000N FE scanning electron microscope. Polycrystalline samples were mounted on carbon tape and placed into an evacuated chamber. The electron beam energy was 20 kV. Scans were collected from multiple spots on several crystals. Energy-dispersive x-ray spectroscopy (EDS) analyses indicated that the powder samples were homogeneous and their elemental composition 1.0(1) Ca: 2.5(5) Ce: 4.0(2) S was in good agreement with values expected from the compound stoichiometry.

2.2.3 *Differential Scanning Calorimetry/Thermogravimetric Analysis (DSC/TGA)*

DSC/TGA analyses were performed on a SDT Q600 equipment (TA Instruments) in an alumina crucible. Ten milligrams of finely dispersed powder were heated from 80°C to 800°C at a $10°C \cdot min^{-1}$ heating rate, under constant airflow ($100\ mL \cdot min^{-1}$).

2.2.4 *Optical and Electrochemical/Photoelectrochemical Property Measurements*

2.2.4.1 Diffuse Reflectance Spectroscopy

The optical bandgap of the synthesized powder determined by diffuse reflectance spectroscopy (DRS) coupled with Tauc analyses. [21, 25] The DRS data were collected from 300 to 1000 nm using a PerkinElmer Lambda 35 spectrophotometer equipped with an integrating sphere accessory. The absorption spectrum was calculated from the reflection spectrum via the Kubelka-Munk function: $\alpha/S = (1-R)2/2R$, in which α is the absorption coefficient, S is the scattering coefficient, and R is the reflectance. [21]

2.2.4.2 Colorimetry

A Konica Minolta CM-700d Spectrophotometer (Standard illuminant D_{65}) was used to measure *L*, a*, b** color coordinates.

2.2.4.3 Photoelectrochemistry and Electrochemistry

Firstly, a porous film of $CaCe_2S_4$ particles (geometric area = 1.0 cm²) was deposited on a Ti substrate from an aqueous suspension consisted of $CaCe_2S_4$ particles, which was obtained by grinding the sulfide particles in an agate mortar together with a polyethylene glycol (PEG - MW= 20000) water solution. The sulfide:PEG:water mass ratio of the resulting suspension was 1:1:5. A small aliquot of the obtained suspension was spread using a glass rod onto previously cleaned and etched 3.3 x 1.0 cm titanium foil piece. The geometrical area was delimited by adhesive tape. After drying at room temperature, the electrode was heated at 350°C for 30 min and then at 450°C for 30 min to promote sample annealing together with PEG and water removal. This process resulted in a uniform, homogeneous film of $CaCe_2S_4$ adhered to the titanium substrate. The electrochemical measurements were performed using a three-electrode, single-compartment electrochemical cell and a CH Instruments potentiostat (Model CHI720C). A Pt wire and Ag/AgCl/KCl (4 M) were used as the counterelectrode and reference electrode, respectively. All potentials are quoted with respect to Ag/AgCl reference unless otherwise specified. Deaerated aqueous 0.1 M Na2SO4 was used as the supporting electrolyte, with 0.1 M Na_2SO_3 added as a hole scavenger. Aqueous polysulfide (1 M Na_2S, 1 M S and 1 M NaOH) was used in other experiments. For photovoltammetry, the potential was swept at a low scan rate (5 mV.s-1) starting at -0.3 V up to +1.0 V with the dark/illuminated cycles alternated in 5s intervals with a manual chopper. A 400 W Xe-arc lamp (Newport) was used as the radiation source. The electrochemical cell was placed ~20 cm away from the radiation source. The nominal photon flux at the electrode surface was 300 mW/cm^2 (measured using a radiant power meter (Newport 70260) combined with a probe (Newport, 70268)).

2.3 Results and Discussion

2.3.1 *X-ray Diffraction*

Figure 2-1 shows the crystal structure of $CaCe_2S_4$, and Table 2-1 summarizes the crystallographic results obtained from Rietveld refinements. $CaCe_2S_4$ adopts the Th_3P_4 structure type where Ca^{2+} and Ce^{3+} ions occupy the 12a site. The Ca^{2+}/Ce^{3+} ions form a triangular dodecahedron with eight S^{2-}. The average bond length between Ca^{2+}/Ce^{3+} and S^{2-} is 2.98(5) Å.

Each $(Ca,Ce)S_8$ dodecahedron shares one triangular face or edge with another dodecahedron, creating a distorted S_4 tetrahedron vacancy. Our results agree with the previously reported structure determined from samples made by heating elemental Ce and CaS with H_2S flow. [16, 26-27] The diffraction pattern and refinement model of $CaCe_2S_4$ are presented in Figure 2-2. Five peaks at 2θ = 6.85, 6.91, 7.67, 9.73 and 13.7° were found to match the most intense peaks of Ce_2O_2S. By comparing intensities of the most intense peak (2θ ~ 7.67°) of Ce_2O_2S to the most intense peak of $CaCe_2S_4$ (2θ ~ 8.72 °), it is estimated that ~0.10% of the sample was due to the presence of Ce_2O_2S.

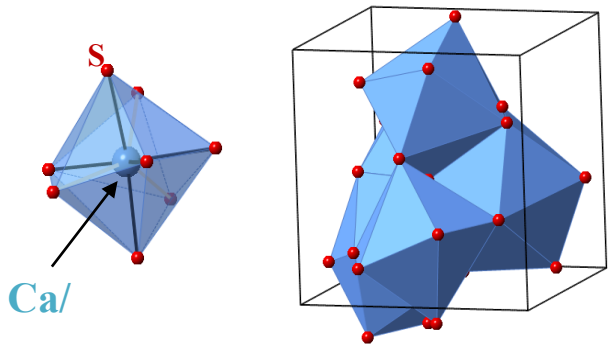

Figure 2-1 The crystal structure of $CaLn_2S_4$ consists of S_8 dodecahedra (blue). Ca/Ce and S are shown as blue and red spheres, respectively. The cubic unit cell is shown as a solid black line. One dodecahedron is enlarged on the left hand side for clarity.

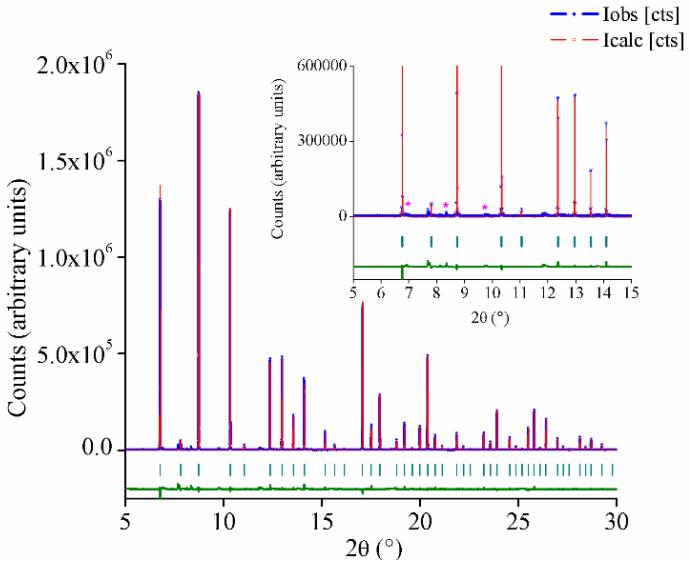

Figure 2-2. XRD data (black line) and Rietveld model (red line) for $CaCe_2S_4$. The calculated Bragg reflections (green tick marks) and the curve for the difference between experimental data and calculated profiles (green line) are also indicated. Inset: A portion of the powder diffraction pattern with impurity peaks marked with asterisks.

Table 2-1. Structure refinement results for powder X-ray diffraction of $CaCe_2S_4$

$CaCe_2S_4$						
R_p: 5.232 R_{wp}: 7.893 R_{exp}: 2.36 χ^2: 6.62						
a = 8.614804 (3) Å						
Atom	Wycoff	*x*	*y*	*Z*	B_{iso} (Å^2)	Occupancy
Ca	12*a*	1/8	0	¼	0.4950(2)	0.3340(3)
Ce	12*a*	1/8	0	¼	0.4647(2)	0.6659(3)
S	16*c*	0.0714(1)	0.0714(1)	0.0714(1)	0.4840(5)	1

2.3.2 *Diffuse Reflectance Spectroscopy (DRS)*

Data collected from DRS measurements on $CaCe_2S_4$ were fit to a Kubelka-Munk function. [28] The original DRS data are shown in Figure 2-3 and the Tauc plots, [29] shown in Figure 3 (inset), derived from these, indicate the presence of both direct and indirect optical transitions with corresponding band gap values, E_g = 2.17 eV and 2.13 eV, respectively. These values are smaller than the E_g of CaS (4.6 eV) [30-31] but comparable to that of Ce_2S_3 (2.0 eV).[18] The latter trend is consistent with the similar band structures of $CaCe_2S_4$ and Ce_2S_3. [18, 32] Presumably, the observed optical transitions in $CaCe_2S_4$ (and in Ce_2S_3) may be regarded as originating from electronic transitions involving localized Ce 4*f* electrons. The presence of both direct and indirect optical transitions within the same material at very close energies, must not be considered as unusual, especially for ternary compound semiconductors. For example, there is recent precedence for such optical behavior for $BiVO_4$. [33]

2.3.3 *Thermal Stability*

As mentioned at the outset of this work, the stability of photoactive chalcogenides remains as a challenging drawback to overcome for technological applications. Aside from the PEC stability of $CaCe_2S_4$ addressed in the preceding section, thermal stability is equally important in applications related to thermochromics or in scenarios involving concentrated sunlight. To probe

this, DSC/TGA analyses were performed; the data are shown in Figure 2-4. Significantly, no oxidation/decomposition processes take place at temperatures up to 450°C, indicating the remarkable thermal stability of $CaCe_2S_4$. In contrast, the binary counterpart, Ce_2S_3 promptly reacts with atmospheric oxygen and water even at room temperature. [34]

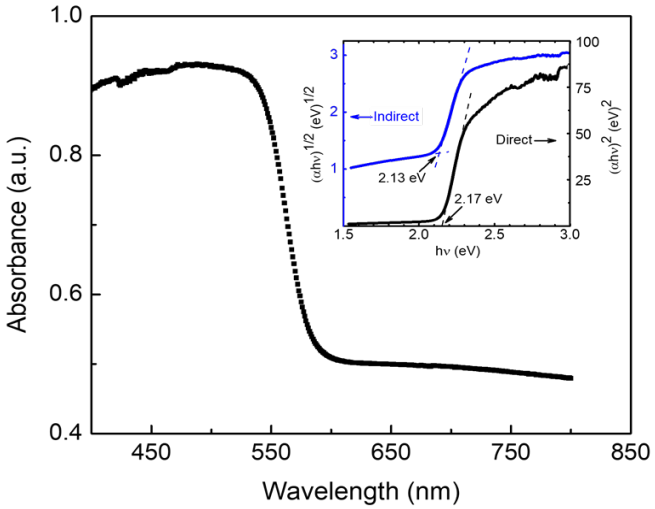

Figure 2-3. DRS data and Tauc plots (inset) considering direct (a) and indirect (b) band gap electronic transitions for $CaCe_2S_4$ powder. The band gap value (Eg) is indicated in each case.

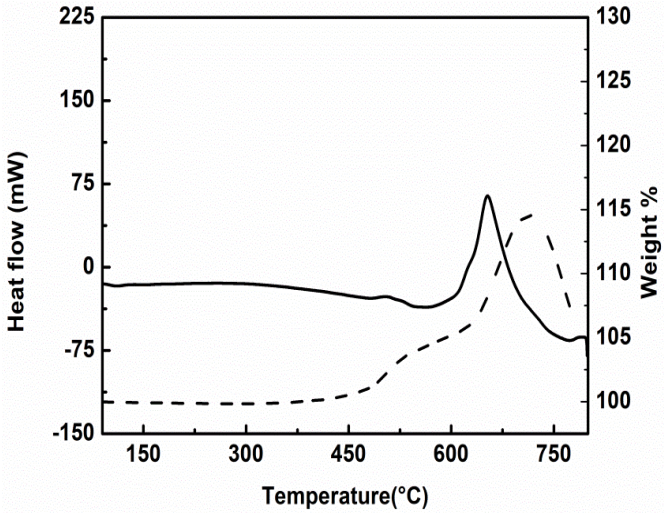

Figure 2-4. Thermal stability of $CaCe_2S_4$ as demonstrated by DSC/TGA analyses. The scans are for a first heating curve to 800°C at 10°C.min-1, under 100 mL.min-1 airflows. The solid and dashed lines represent DSC and TGA curves, respectively.

2.3.4 *Electrochemical and Photoelectrochemical Behavior*

To further assess the semiconductor characteristics beyond what is seen in the optical data (Figure 2-3), photocurrent response measurements were performed using a Ti-supported $CaCe_2S_4$ thin film electrode as a photoanode in a three-electrode electrochemical cell. Figure 2-5a shows a linear sweep photovoltammetry scan with the excitation light manually interrupted. A positive (anodic) photocurrent is seen along the entire scan, indicating that the material shows n-type semiconductor behavior[35] in the potential range: -0.3 → +1.0 V. The non-flat ("dark") baseline, at potentials positive of ~0.3V, may be assigned to electrochemical oxidation of sulfite ions in solution on the n-$CaCe_2S_4$ surface. Support for this notion accrues from a comparison of cyclic voltammetry (CV) data on n-$CaCe_2S_4$ in the presence and absence of SO_3^{2-} ions in the dark (Figure 2-S1).

Note the anodic dark current flow observed when the sulfite redox species were dosed into the Na_2SO_4 supporting electrolyte (Figure 2-5a, red trace). Note also that, as expected, the spiked transient profile in Figure 2-5a associated with charge carriers recombination reverted to a rectangular one as the sample was increasingly reverse-biased in the positive potential regime, indicating that charge carrier (e^- - h^+) recombination is suppressed at higher overpotentials. These data also shed useful light (no pun intended) on the quality of the electrical contact between the $CaCe_2S_4$ film and the underlying Ti substrate. For instance, if this contact had substantial Ohmic resistance, the dark voltammogram part of the envelope in Figure 2-5a (as well as the CV scans in Figure 2-S1) would have been characterized by a steep slope instead of being reasonably horizontal.

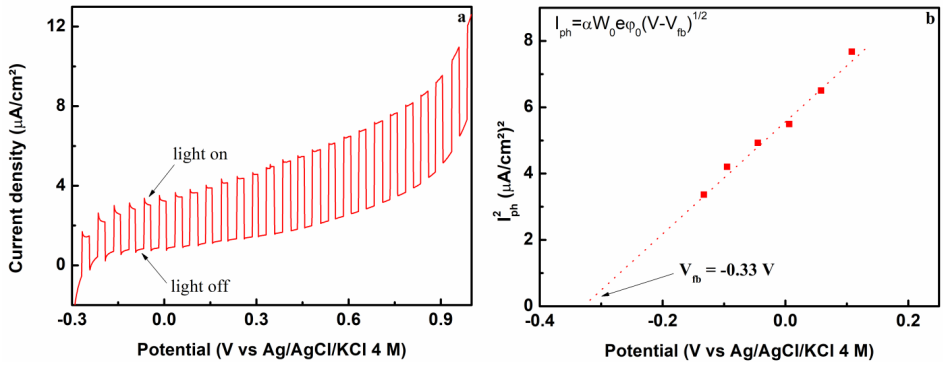

Figure 2-5. Ti|$CaCe_2S_4$ electrode in 0.1 mol L^{-1} Na_2SO_4 aqueous solution containing 0.1 mol L^{-1} Na_2SO_3 as hole scavenger under intermittent irradiation: (a) Photovoltammetry measurement performed at a potential scan rate of 5 mV s^{-1} and (b) Variation of the square of photocurrent as a function of applied potential (Butler-Gärtner plot).

Location of the flat band potential (V_{fb}) can be inferred from such data using the Butler-Gärtner model[29, 35-36], which correlates the photocurrent (I_{ph}) with the applied potential V via the following equation:

$$I_{ph} = \alpha W_0 e \varphi_0 (V - V_{fb})^{1/2}$$

where α is the light absorption coefficient of the material (as defined earlier), W_0 is the width of the depletion layer at the semiconductor/solution interface, and φ_0 is the photon flux. By plotting the square of the photocurrent *versus* the applied potential, one can obtain V_{fb} as the value in which I_{ph}^2 equals zero. [29, 35-36] Figure 2-5b shows a so-called Butler-Gärtner plot for the $CaCe_2S_4$ electrode, with V_{fb} = -0.33 V *vs* Ag/AgCl/KCl 4 M.

Although the flat-band potential refers to location of the semiconductor Fermi level,[35] for reasonably doped n-type semiconductors, this value is a good approximation for the conduction band edge. Combining the V_{fb} value with the E_g values obtained from Tauc plots (see above), it is possible to estimate the band edge positions for a given semiconductor. These band locations then may be visualized relative to selected redox potentials on a *common* scale.[35] This is shown in Figure 2-6 for the *n*-$CaCe_2S_4$ sample, considering both direct and indirect electronic transitions. Redox potentials for water oxidation and reduction half-reactions are also shown on this diagram along with the redox potential for the sulfite/sulfate couple, [37] used in the experiments in Figures 2-5 and 2-6 above. As the norm for such diagrams,[35] all the redox potentials were converted to the normal hydrogen electrode (NHE) scale and at a common solution pH.

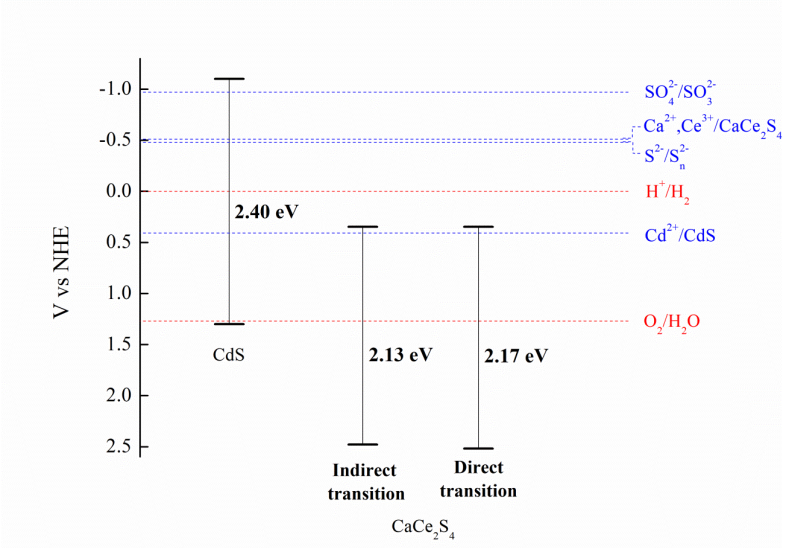

Figure 2-6. Valence band edge and conduction band edge locations for n-$CaCe_2S_4$ (as derived from the DRS and photocurrent measurement data in Figures 2-3 and 2-5). Red lines indicates redox potentials for the half reactions involved in the water splitting process at pH = 0. Band edge locations for a benchmark chalcogenide semiconductor, n-CdS, are also shown (see text). Corresponding hole (oxidative) decomposition potentials (see text for derivation of these values) are also depicted on the same diagram for both n-CdS and n-$CaCe_2S_4$.

From Figure 2-6, it may be concluded that the photogenerated holes in *n*-$CaCe_2S_4$ are thermodynamically capable of oxidizing water (to O_2). On the other hand, the photogenerated electrons are not able to reduce water and instigate the HER because the conduction band edge lies positive of the water reduction potential. It is also seen from Figure 2-6 that there is a very large driving force for the sulfite/sulfate redox couple to donate electrons to the valence band edge of *n*-$CaCe_2S_4$ (i.e., to sustain the oxidation of sulfite to sulfate.). However, the data in Figures 2-5 and 2-6 show the interfacial *kinetics* of this process is rather slow because both the dark oxidation current (red trace, Figure 2-S1) and the photocurrent in Figure 2-5 are rather low (only less than ~10 μA/cm^2).

Further research, beyond the scope of this exploratory study would be needed to unravel the factors behind this observation. Undoubtedly, co-catalysts would be needed on the *n*-$CaCe_2S_4$ surface to drive multi-electron redox reactions such as water oxidation.

Consistent with the above trend, *powder suspensions* of *n*-$CaCe_2S_4$ were tested for their (heterogeneous) photocatalytic activity for oxidation of an azo dye, methyl orange [38]. Disappointingly, no decoloration of the dye was noted even after several minutes of irradiation. Clearly, the hole transfer kinetics on the *as-synthesized n*-$CaCe_2S_4$ are far from optimal.

2.3.4.1 A Note on Doping

The PEC data in Figure 2-5a (and in Figure 2-7a below) diagnose the as-synthesized $CaCe_2S_4$ to be an *n*-type semiconductor. It is worth underlining that in all the PEC experiments in this study, the material did not undergo a thermal pre-anneal. The semiconductor nature of metal chalcogenides is notoriously sensitive to thermal pre-history. They also generally exhibit compositional doping in that, whether the compound is an *n*- or a *p*-type semiconductor, is dictated by whether the metal or the chalcogen is in excess respectively. A case in point is CdTe; thus *n*-CdTe has Cd in slight excess while *p*-CdTe has an excess of Te in it, beyond the exact 1:1 stoichiometry for the intrinsic semiconductor.[39] Further studies are needed to determine the presence of excess Ca and Ce in the $CaCe_2S_4$ samples used here. Nonetheless, the preparation method used here (see Experimental) and the avoidance of H_2S or CS_2 gas, could conspire to create a situation where any slight loss of the sulfide component in the precursor mixture (via evaporative losses during the prolonged heating) would yield a metal-excess stoichiometry. The EDS data were not sufficiently sensitive to probe slight departures from stoichiometry. Also unfortunately, it is worth noting that none of the other previous studies on this compound [16, 18-19]shed light on its semiconductor behavior to enable possible trends on the effect of preparation history to be established.

2.3.4.2 Photoelectrochemical Stability

Aqueous polysulfide redox electrolyte is commonly used to kinetically stabilize metal chalcogenide photoanodes from undergoing anodic corrosion.[28] For example, the band edges of a benchmark compound, CdS, is compared against the sulfide/polysulfide redox potential and the decomposition potential of CdS in Figure 2-6. The latter was calculated from thermochemical data [40-41] for the various species in the reaction:

$$Cd^{2+}_{(aq)} + S_{(s)} + 2e^- \rightarrow CdS_{(S)} \qquad E^0 = +0.41 \text{ V vs NHE}$$

As also discussed by previous authors,[28, 42] the relative dispositions of the two redox couples (Figure 2-6) suggest that hole transfer to polysulfide kinetically offsets the (presumably slow) hole attack of the semiconductor itself leading to suppression of photocorrosion. Our computed value of the decomposition potential for CdS is in reasonable agreement with values reported by previous authors.[12, 43]

The relative ordering of the decomposition potential and the sulfite and polysulfide redox couples is shown for *n*-$CaCe_2S_4$ (Figure 2-6). The decomposition potential for the ternary chalcogenide was also calculated from the 8-electron reaction:

$$Ca^{2+}_{(aq)} + 2\ Ce^{3+}_{(aq)} + 4\ S_{(s)} + 8\ e^- \rightarrow CaCe_2S_{4(S)} \qquad E^0 = -0.51\ V\ vs\ NHE$$

Unfortunately, however, thermochemical data are non-existent for this compound. Nonetheless, the structural similarity of *n*-$CaCe_2S_4$ and another *binary* chalcogenide, namely Ce_3S_4, may be exploited; both belong to the Th_3P_4 structure type (see above). Thermochemical data indeed are available for Ce_3S_4 and were accordingly used above in substitution for the missing literature data.[40-41] The relative location of the *n*-$CaCe_2S_4$ decomposition potential, relative to the compound bandedges, is shown in Figure 2-6. While this compound is certainly *thermodynamically* susceptible to anodic photocorrosion, our data (see below) suggest that both the sulfite and poysulfide redox couples are able to *kinetically* suppress it. Note that in both the corrosion reactions shown above, the heat of formation of elemental sulfur is zero.

It is worth noting that energy diagrams such as those in Figure 2-6 have at best only a *thermodynamic* predictive utility. They are useful for assessing whether a given reaction will even take place and if it does, the extent of the thermodynamic driving force. The reaction *kinetics* are a whole different matter altogether. We are also aware that cases where the semiconductor band edges bracket the redox potentials for water oxidation and HER must not be construed to translate to efficient and sustained splitting of water. In fact, it is quite unlikely that a single semiconductor can drive this difficult process.

Figure 2-7 contains PEC data bearing on the photostability of *n*-$CaCe_2S_4$ in aqueous sulfite and polysulfide media. Firstly, the hole transfer kinetics are significantly improved in polysulfide as compared to the sulfite redox electrolyte. Compare the relative photocurrent levels

in the photovoltammetry data in Figure 2-7a. Thus the photocurrents in polysulfide (blue trace) are ~2-fold higher relative to sulfite (red line), underlining the faster kinetics in the former case. Figure 2-7b contains photocurrent-time profiles for the Ti|$CaCe_2S_4$ photoanode at a fixed reverse bias potential in the two electrolytes. The photocurrents are stable and horizontal with respect to time (after an induction period of ~2 min) indicating that the photoanode surface is not undergoing significant photocorrosion. An induction period is commonly observed in such experiments [44] and is attributable to surface exchange of sulfide with solution species.

Further measurements, both via electrochemical quartz crystal microgravimetry (EQCM) [45] as well as via solution analyses for the presence of metal ions (see reactions above) will conclusively establish the veracity of our PEC stability claim. Once again, such pending experiments are beyond the scope of this exploratory study.

Aqueous polysulfide used a mixture of 1 M Na2S, 1 M S and 1 M NaOH. For sulfite redox, 0.1 M Na_2SO_4 was used as supporting electrolyte together with 0.1 M Na_2SO_3 added as hole scavenger. (b) Anodic photocurrent versus time in the two electrolytes with the photoanode poised at 0.6 V vs. Ag/AgCl/KCl 4 M. In all the cases, nitrogen gas was purged through the solutions for de-aeration, and the noise from this is visible on the upper trace in Figure 2-7b. The Ti data (black) in Figure 2-7a constitute a blank, demonstrating that the incipient native oxide layer on Ti has negligible photoactivity under the irradiation conditions relevant to this study.

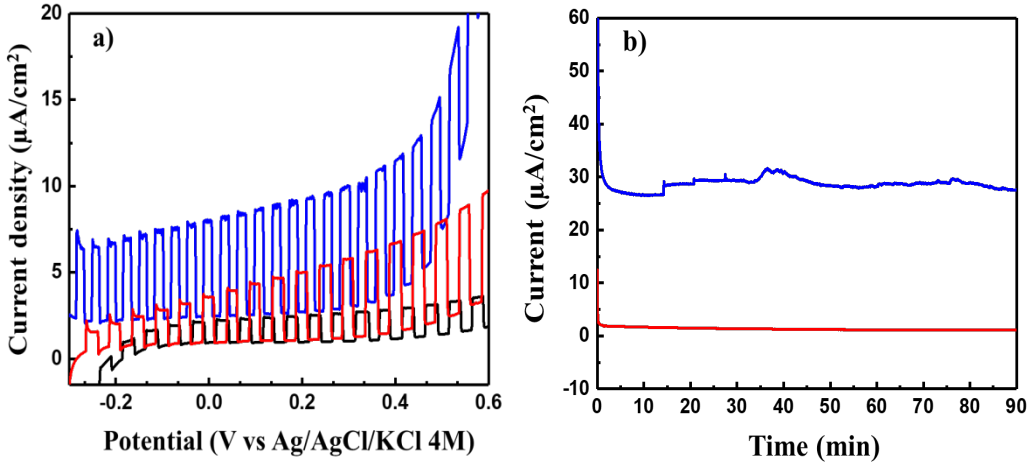

Figure 2-7(a) Photovoltammetry of Ti|$CaCe_2S_4$ electrode at 5 $mV.s^{-1}$ scan rate with intermittent irradiation in polysulfide (blue) and sulfite (red and black) redox electrolytes.

2.3.4.3 Colorimetry

Colorimetry measurements were performed to support optical measurements. The chromatic properties of $CaCe_2S_4$ were evaluated based on the International Commission on Illumination (CIE) 1976 color space.[46] Results are summarized in Table 2-2. In the CIE color coordinate system, *L** or lightness, refers to a numerical scale from 0 to 100 where 0 is black and 100 is white. Red and green colors are defined as *a** and *-a**, respectively; blue and yellow colors are defined as *b** and *-b**, respectively. Chroma, *C**, represents the saturation of color and the hue angle, *h*, represents the angle on a circular axis where the color ranges from 0 (red) through 90 (yellow), 180 (green), 270 (blue) and back to 0.[46]

Although the observed band gaps of γ-Ce_2S_3 and $CaCe_2S_4$ are quite similar, they can be differentiated by their chromatic properties. Compared to its parent compound, γ-Ce_2S_3, $CaCe_2S_4$ exhibits significantly higher *a** and *b** values, illustrating enhancement in the redness of $CaCe_2S_4$. Because $C^* = [(a^*)^2+(b^*)^2]^{1/2}$, the larger *C** of $CaCe_2S_4$ compared to Ce_2S_3 indicates that $CaCe_2S_4$ possesses a richer color saturation than Ce_2S_3.

Table 2-2. Chromatic Properties of γ-Ce_2S_3 and $CaCe_2S_4$

Parameter	**γ-Ce_2S_3**	**$CaCe_2S_4$**
L*	42.68	46.04
a*	27.87	35.72
b*	12.44	36.68
C*	30.52	51.20
h°	24.05	45.76

2.4 Conclusions

A greener solid-state synthesis method, not necessitating the flow of noxious gases, was demonstrated and applied for the synthesis of $CaCe_2S_4$. The structural details of this compound were established via powder X-ray diffraction; the compound/phase purity being corroborated via Rietveld refinement of the diffraction data. Optical analyses via diffuse reflectance revealed the presence of both direct and indirect transitions with closely overlapping band gap energies – a behavior reminiscent of a ternary oxide, $BiVO_4$. Photoelectrochemical (PEC) experiments showed the material to be an *n*-type semiconductor; further work is needed to establish the defect chemistry of *n*-$CaCe_2S_4$ as synthesized. Thermal analyses suggest the compound to be stable to temperatures as high as ~450 °C, suggesting thermal anneal to be a viable strategy for modifying dopant profiles and improving PEC performance such that photocurrents in the mA/cm^2 regime can be secured. The as-synthesized powder revealed disappointingly low interfacial hole transfer kinetics to acceptor redox species such as water and sulfite although the behavior was somewhat improved in aqueous polysulfide electrolyte. It should also be noted that no co-catalyst was used on the *n*-$CaCe_2S_4$ surface for the experiments in Figures 2-5,2- 6, and 2-8 nor was the material thermally annealed to improve its morphology. Such strategies will be deployed in planned studies addressing the applicability of *n*-$CaCe_2S_4$ (and similar ternary chalcogenides) for solar water splitting, heterogeneous photocatalysis, and solar fuel generation in general.

References

1. Zhang, K.; Guo, L., Metal sulphide semiconductors for photocatalytic hydrogen production. *Catal. Sci. Technol.* **2013,** *3*, 1672-1690.
2. Yang, L.; Hong, H.; Fu, Q.; Huang, Y.; Zhang, J.; Cui, X.; Fan, Z.; Liu, K.; Xiang, B., Single-crystal atomic-layered molybdenum disulfide nanobelts with high surface activity. *ACS Nano.* **2015,** *9*, 6478-6483.
3. Gao, M.-R.; Chan, M. K. Y.; Sun, Y., Edge-terminated molybdenum disulfide with a 9.4-Å interlayer spacing for electrochemical hydrogen production. *Nat. Commun.* **2015,** *6*, 7493.
4. Voiry, D.; Yamaguchi, H.; Li, J.; Silva, R.; Alves, D. C. B.; Fujita, T.; Chen, M.; Asefa, T.; Shenoy, V. B.; Eda, G.; Chhowalla, M., Enhanced catalytic activity in strained chemically exfoliated WS_2 nanosheets for hydrogen evolution. *Nat. Mater.* **2013,** *12*, 850-855.
5. Huang, X.; Zeng, Z.; Zhang, H., Metal dichalcogenide nanosheets: preparation, properties and applications. *Chem. Soc. Rev.* **2013,** *42*, 1934-1946.
6. Faber, M. S.; Jin, S., Earth-abundant inorganic electrocatalysts and their nanostructures for energy conversion applications. *Energy Environ. Sci.* **2014,** *7* , 3519-3542.
7. Nicolosi, V.; Chhowalla, M.; Kanatzidis, M. G.; Strano, M. S.; Coleman, J. N., Liquid exfoliation of layered materials. *Science* **2013,** *340*, 1420-1438.
8. Vesborg, P. C. K.; Seger, B.; Chorkendorff, I., Recent development in hydrogen evolution reaction catalysts and their practical implementation. *J. Phys. Chem. Lett.* **2015,** *6*, 951-957.
9. Rajeshwar, K., Materials aspects of photoelectrochemical energy conversion. *J. Appl. Electrochem.* **1985,** *15*, 1.
10. Rajeshwar, K.; McConnell, R. D.; Licht, S., Solar Hydrogen Generation: Toward a Renewable Energy Future. *Springer*: New York, **2008**.
11. Rajeshwar, K.; Ibanez, J. G., Environmental Electrochemistry. Academic Press: San Diego, **1997**, 15-16.
12. Ellis, A. B.; Kaiser, S. W.; Bolts, J. M.; Wrighton, M. S., Study of n-type semiconducting cadmium chalcogenide-based photoelectrochemical cells employing polychalcogenide electrolytes. *J. Am. Chem. Soc.* **1977,** *99*, 2839-2848.
13. Meissner, D.; Memming, R.; Kastening, B., Photoelectrochemistry of cadmium sulfide. 1. Reanalysis of photocorrosion and flat-band potential. *J. Phys. Chem.* **1988,** *92*, 3476-3483.
14. Weber, A.; Mainz, R.; Schock, H., On the Sn loss from thin films of the material system Cu-Zn-Sn-S in high vacuum. *J. Appl. Phys.* **2010,** *107*, 013516, pp. 1-6.
15. Zegkinoglou, I.; Zendegani, A.; Sinev, I.; Kunze, S.; Mistry, H.; Jeon, H. S.; Zhao, J. Y.; Hu, M. Y.; Alp, E. E.; Piontek, S.; Smialkowski, M.; Apfel, U. P.; Kormann, F.; Neugebauer, J.; Hickel, T.; Cuenya, B. R., Operando phonon studies of the protonation mechanism in highly active hydrogen evolution reaction pentlandite catalysts. *J. Am. Chem. Soc.* **2017,** *139*, 14360-14363.
16. Flahaut, J.; Domange, L.; Patrie, M., Combinaisons formees par les sulfures des elements du group des terres rares. 5. vue densemble sur les systems formes part le sulfure dyttrium avec les sulfures des elements divalents. *Bull. Soc. Chim. Fr.* **1962,** *35*, 159.
17. Perrin, M. A.; Wimmer, E., Color of pure and alkali-doped cerium sulfide: A local-density-functional study. *Phys. Rev. B.* **1996,** *54*, 2428-2435.
18. Mauricot, R.; Gressier, P.; Evain, M.; Brec, R., Comparative study of some rare-earth sulfides - doped gamma AM_2S_3 (M=La,Ce and Nd, A=Na,K and Ca) and unoped gamma M_2S_3 (M=La,Ce and Nd). *J. Alloys Compd.* **1995,** *223*, 130-138.
19. Laronze, H.; Demourgues, A.; Tressaud, A.; Lozano, L.; Grannec, J.; Guillen, F.; Macaudiere, P.; Maestro, P., Preparation and characterization of alkali- and alkaline earth-based rare earth sulfides. *J. Alloys Compd.* **1998,** *275*, 113-117.

20. Zhukov, V.; Mauricot, R.; Gressier, P.; Evain, M., Band electronic structure study of some doped and undoped gamma-Ln_2S_3 (Ln=La, Ce, Pr, and Nd) rare earth sulfides through LMTO-TB calculations. *J. Solid State Chem.* **1997,** *128*, 197-204.
21. Murphy, A. B., Band-gap determination from diffuse reflectance measurements of semiconductor films, and application to photoelectrochemical water-splitting. *Sol. Energy Mater Sol. Cells.* **2007,** *91*, 1326-1337.
22. Degen, T.; Sadki, M.; Bron, E.; Konig, U.; Nenert, G., The HighScore suite. *Powder Diffraction.* **2014,** *29*, S13-S18.
23. Caglioti, G.; Paoletti, A.; Ricci, F. P., Choice of collimators for a crystal spectrometer for neutron diffraction. *Nucl. Instr. Meth. Phys. Res.* **1958,** *3*, 223-228.
24. David, W. I. F., Powder diffraction peak shapes -Parameterization of the pseudo-voigt as a voigt function. *J. Appl. Cryst.* **1986,** *19*, 63-64.
25. Ohtani, B., Photocatalysis A to Z—What we know and what we do not know in a scientific sense. *J. Photochem. Photobio.* **2010,** *11* , 157-178.
26. Yim, W. M.; Fan, A. K.; Stofko, E. J., Preparation and properties of II-Ln_2-S_4 sulfides. *J. Electrochem. Soc.* **1973,** *120*, 441-446.
27. Zolotova, E. S.; Belyaeva, E. I.; Kamarzin, A. A., Synthesis and properties of cerium and alkaline-earth metal double sulfides MIICe_2S_4. *Zh. Neorg. Khim.* **2001,** *46*, 1795-1797.
28. Bard, A. J.; Wrighton, M. S., Thermodynamic potential for the anodic dissolution of n-type semiconductors. *J. Electrochem. Soc.* **1977,** *124*, 1706-1710.
29. Gärtner, W. W., Depletion-layer photoeffects in semiconductors. *Phys. Rev.* **1959,** *116*, 84-87.
30. Jia, D.; Wetzer, R. S.; Yen, W. M., Ce^{3+} energy levels relative to the band structure in CaS: evidence from photoionization and electron trapping. *J. Lumin.* **2002,** *99*, 1-6.
31. Choi, H.; Kim, C.-H.; Pyun, C.-H., Structure and luminescence properties of $Ca_{1-x}La_xS$ (x = 0-0.3). *J. Solid State Chem.* **1997,** *131*, 101-107.
32. Windiks, R.; Wimmer, E.; Pourovskii, L.; Biermann, S.; Georges, A., Structure and optical properties of α- and γ-cerium sesquisulfide. *J. Alloys Cmpd.* **2008,** *459*, 438-446.
33. Cooper, J. K.; Gul, S.; Toma, F. M.; Chen, L.; Liu, Y.-S.; Guo, J.; Ager, J. W.; Yano, J.; Sharp, I. D., Indirect bandgap and optical properties of monoclinic bismuth vanadate. *J. Phys. Chem. C* **2015,** *119*, 2969-2974.
34. Sulfide, C. I. https://www.alfa.com/en/catalog/043646/. (accessed October 23, 2017).
35. Rajeshwar, K., Fundamentals of Semiconductor Electrochemistry and Photoelectrochemistry. In *Enyclopedia of Electrochemistry*, Licht, S., Ed. Wiley-VCH: Weinheim, 2001; *3*, 3-53.
36. Butler, M. A., Photoelectrolysis and physical properties of the semiconducting electrode WO_2. *J. Appl. Phys.* **1977,** *48*, 1914-1920.
37. Bard, A. J.; Parsons, R.; Jordan, J.; International Union of, P.; Applied, C., *Standard Potentials in Aqueous Solution*. 1st ed.; M. Dekker: New York, **1985**.
38. Rajeshwar, K.; Osugi, M. E.; Chanmanee, W.; Chenthamarakshan, C. R.; Zanoni, M. V. B.; Kajitvichyanukul, P.; Krishnan-Ayer, R., Heterogeneous photocatalytic treatment of organic dyes in air and aqueous media. *J.Photochem. Photobiol. C: Photochem. Rev.* **2008,** *9*, 171-192.
39. Kröger, F. A., Cathodic deposition and characterization of metallic or semiconducting binary alloys or compounds. *J. Electrochem. Soc.* **1978,** *125*, 2028.
40. Dean, J. A.; Lange, N. A., *Lange's Handbook of Chemistry*. 11 ed.; McGraw-Hill: New York, 1978, *6*, 2028-2034.
41. Lide, D. R., *CRC Handbook* CRC: Boca Ratón, Florida, 2003.
42. Gerischer, H., On the stability of semiconductor electrodes against photodecomposition. *J.Electroanal. Chem.* **1977,** *82* , 133-143.
43. Kohl, P. A.; Bard, A. J., Semiconductor electrodes. 13 Characterization and behavior of n-type zinc oxide, cadmium sulfide, and gallium phosphide electrodes in acetonitrile solutions. *J. Am. Chem. Soc.* **1977,** *99*, 7531-7539.
44. Bouroushian, M., *Electrochemistry of Metal Chalcogenides*. Springer: Berlin, **2010**.

45. Myung, N.; Kim, S.; Lincot, D.; Lepiller, C.; de Tacconi, N. R.; Rajeshwar, K., The deposition of Group 6A-derived inorganic semiconductor films as studied by quartz crystal microgravimetry. *Electrochim. Act.* **2000,** *45* , 3749-3756.
46. L'Eclairage, C. I. d., Recommendations on uniform color spaces, color-difference equations, psychometric color terms. *Color Res Appl*. 1977, 2, 5-6.

Chapter 3 The role The Role of f-Electrons on the Optical and Photoelectrochemical Behavior of $Ca(La_{1-x}Ce_x)_2S_4$ ($0 \leq x \leq 1$)

Abstract

This study focuses on a solid solution series, $Ca(La_{1-x}Ce_x)_2S_4$ ($0 \leq x \leq 1$), where the *f*-electron density is absent in $CaLa_2S_4$ and is progressively increased until it is maximized in $CaCe_2S_4$. Correspondingly, these samples synthesized by a sealed ampoule method, showed progressive variations in color ranging from grey for $CaLa_2S_4$ to orange-red for $CaCe_2S_4$. The crystal structural nuances of both the end members and three solid solutions with x = 0.25, 0.50, 0.75 were established with the complementary use of synchrotron X-ray diffraction and neutron scattering. Interestingly, these data were consistent with a two-phase composition centered around each nominal solid-solution stoichiometry. Optical characterization via diffuse reflectance spectroscopy and Tauc analyses showed a shrinking of the energy band gap (from the UV to visible range) when Ce was progressively introduced into the host $CaLa_2S_4$ structure. These data were in concert with electronic band structure calculations, using density functional theory, which showed the progressive formation of an intermediate *f* band when Ce was introduced intro the structure. Photoelectrochemical measurements in an aqueous redox electrolyte, as well as surface photovoltage and Kelvin probe measurements, revealed all samples to be *n*-type semiconductors. The valence and conduction band edge positions of the end members and the three solid solutions could be mapped, on both the redox and vacuum reference energy scales, by combining these measurements with the optical data.

3.1 Introduction

Metal chalcogenides have long been of interest to chemists because of their applicability in diverse technologies including thermoelectrics, photovoltaics, nonlinear optics, and even superconductors and topological insulators.[1-6] The scientific community continues to explore rare-earth chalcogenides with new structures; synthetic techniques such as molten polychalcogenide fluxes, and characterization of these materials using in-situ diffraction (panoramic synthesis) have contributed to the fast-growing expansion of chalcogenide materials in general.[1]

Rare-earth chalcogenides are particularly interesting because of their wide array of crystal structures and physical properties.[2-3] As examples of notable discoveries of new rare-earth chalcogenides in recent years, $Ce_8Sb_2S_{15}$ exhibits a red color due to a 4*f* to 5*d* electronic transition and crystallizes in a noncentrosymmetric space group.[4] The choice of rare earth metal can profoundly impact structure; for example, Ce_4GaSbS_9 crystallizes in non-centrosymmetric space group, but attempts at producing a La-analog yielded a new compound, $La_2Ga_{0.33}SbS_5$, which crystallizes in a centrosymmetric space group.[5]

Quaternary rare-earth chalcogenides have also been recently found through exploratory syntheses, including Nd_7FeInS_{13} and Pr_7CoInS_{13}[6] and selenides, such as $Ba_2LnGaSe_5$ and $Ba_2LnInSe_5$, which are part of the larger Ba_2LnMCh_5 (M = Ga, In; Ch = S, Se, or Te) family that covers four different structure types.[7] $BaLnSn_2Q_6$ (Ln = Ce, Pr, or Nd, Q = S, or Se) exhibits mixed-valent Sn sites,[8] Ba_3LnInS_6 (Ln = Pr, Sm, Gd, or Yb) consists of LnS_6 distorted triangular prisms in a new structure type, and Ba_2NdGaS_5 possesses a band gap corresponding to its observed red color.[9] The chiral chalcogenide, La_4InSbS_9, contains a stereochemically-active lone pair from Sb^{3+} and demonstrates strong potential as a non-linear optical material in the infrared range.[10]

Rare-earth chalcogenides with the Th_3P_4-type are particularly intriguing as they can exhibit metallic to insulating behavior as well as magnetic or superconducting properties.[11] Its structure can be understood by considering the structure of Ce_3S_4, which adopts the cubic Th_3P_4-type. With metal vacancies, the chemical formula can be rewritten as $Ln_{2.67}S_4$. When the vacancies are occupied by an alkaline earth metal, $CaLn_2S_4$ (Ln = La, Ce) is the resultant stoichiometry when one-third of the Ln sites are substituted by Ca. $CaCe_2S_4$ is a red-orange compound that was eventually patented as a coating. $CaLa_2S_4$ shares the same structure, but its optical absorption edge in the UV-range and chemical stability makes it applicable as a ceramic window coating.[12]

One distinguishing feature of rare-earth chalcogenides chalcogenides is the localized nature of the 4*f* band. In CeSF, the localized nature of the Ce atom and the low dimensional crystal structure of CeSF results in an optical transition between S 3*p* → Ce 4*f* states.[13] Band structure

calculations show that the Ce 4*f* → Ce 5*d* electronic transition in alkali-earth doped-Ce_2S_3[14] is responsible for their observed red color. Additionally, the *f* → *d* electronic transitions are *intraband* in nature as opposed to the interband transitions responsible for colors in other well-known metal chalcogenide pigments, CdS and CdSe.[14] The observed red-orange color of $CaCe_2S_4$ is intrinsically caused by the presence of the rare-earth element, Ce, and hence, the presence of *f*-electron density.

To better understand the role of *f*-electrons in optical rare-earth based chalcogenides, we strategically chose to investigate a solid solution series, $Ca(La_{1-x}Ce_x)_2S_4$ ($0 \le x \le 1$), where the *f*-electron density is absent in $CaLa_2S_4$ and is progressively increased until it is maximized in $CaCe_2S_4$. The effects of increasing *f*-electron density in $Ca(La_{1-x}Ce_x)_2S_4$ ($0 \le x \le 1$) are presented below with respect to structural, optical, and photoelectrochemical behavior. When we initially synthesized compounds in this series, the colors of the samples ranged from orange-red in $CaCe_2S_4$ to green in $Ca(La_{0.75}Ce_{0.25})_2S_4$, as shown in Figure 3-1. This tangible progression motivated further a detailed study of structure and photoelectrochemical behavior of these solid solutions, as presented in this article.

Figure 3-1. Photographs of $Ca(La_{1-x}Ce_x)_2S_4$ ($0 \le x \le 1$) samples show the color variation of x = 0.0, 0.25, 0.50, 0.75 and 1.00 compositions.

3.2 Materials and Methods

3.2.1 *Synthesis*

Powder samples of $Ca(La_{1-x}Ce_x)_2S_4$ ($0 \le x \le 1$) were prepared by grinding a stoichiometric ratio of CaS, Ce_2S_3 and La_2S_3 with an agate mortar and pestle. The powders were ground and placed in tantalum foil inside a dry box filled with circulating ultra-high purity argon. The foil and its contents were placed inside a fused silica ampoule and sealed under vacuum. Ampoules were heated at 7 °C/h to 1100 °C, where it dwelled for 100 h, and then cooled to 25 °C

at 20 °C/min. Typical yields based on mass were ~99%. The most common impurity was identified as Ce_2O_2S.

3.2.2 *X-Ray Diffraction*

High resolution X-Ray powder diffraction data were collected using Beamline 11-BM at the Advanced Photon Source, Argonne National Laboratory using an average wavelength of 0.414555 Å for $Ca(La_{0.25}Ce_{0.75})_2S_4$ and $Ca(La_{0.75}Ce_{0.25})_2S_4$ and 0.41273 Å for $Ca(La_{0.50}Ce_{0.50})_2S_4$. Discrete detectors covering an angular range from -6 to 16° in 2θ were scanned over a 2θ range of 34°, with data points collected every 0.001° in 2θ at a scan speed of 0.01 °/s. Data were collected at room temperature.

X'Pert Plus software package [15] was employed to analyze synchrotron data. A previously established structural model of $CaLn_2S_4$ (Ln = La,Ce)[16] was used as a starting model for the refinement of $CaLa_2S_4$ and $CaCe_2S_4$. Global profile refinement parameters included a scale factor, a specimen displacement parameter and peak shape function (U, V, W)[17]. The peak shape was fit using a pseudo-Voigt function[18] and the background was manually determined. Unit cell parameters, site occupancies, and anisotropic/isotropic displacement parameters were refined.

3.2.3 *Neutron Diffraction*

Time-of-flight neutron diffraction data were collected for $Ca(La_{1-x}\ Ce_x)_2S_4$ (x = 0.25, 0.50, 0.75) using the POWGEN powder diffractometer at Oak Ridge National Laboratory. Time of flight data were collected at 300 K using a 60 Hz frequency at with a frame at a center wavelength of 1.066 Å, covering a d-spacing range of 0.2 to 5.0 Å. The collected neutron diffraction data were analyzed by a full pattern Rietveld refinement, using the JANA software package.[19] The convolution pseudo-Voigt function with back-to-back exponential functions was used as a peak shape function.

3.2.4 *Electron Microscopy*

Electron dispersive spectroscopy measurements were performed with a Hitachi S-3000N FE scanning electron microscope. Polycrystalline samples were mounted on carbon tape and placed into an evacuated chamber. The electron beam energy was 20 kV. Scans were collected from multiple spots on several crystals. Energy-dispersive x-ray spectroscopy (EDS) analyses

indicated that elemental composition was in good agreement with expected stoichiometric ratios. These results can be found in Supporting Information.

3.2.5 *Diffuse Reflectance Spectroscopy*

Optical band gaps of $Ca(La_{1-x}\ Ce_x)_2S_4$ ($0 \leq x \leq 1$) were determined by diffuse reflectance spectroscopy (DRS) coupled with Tauc analyses.[20-21] DRS data were collected from 300 to 1000 nm using a PerkinElmer Lambda 35 spectrophotometer equipped with an integrating sphere accessory. The absorption spectrum was calculated from the reflection spectrum via the Kubelka-Munk function: $\alpha/S = (1-R)^2/2R$, where α is the absorption coefficient, S is the scattering coefficient, and R is the reflectance.[20]

3.2.6 *Photoelectrochemistry*

Films of $Ca(La_xCe_{1-x})_2S_4$ were prepared by depositing a suspension of $Ca(La_xCe_{1-x})_2S_4$, polyethylene glycol (PEG - MW:20,000) and water in a 1:1:5 ratio by mass. Suspensions were deposited on a 1.0 cm^2 Ti substrate. Prior to film deposition, the Ti substrates were cut into 3.0×1.0 cm pieces and chemically etched in 36% HCl to remove organic contaminants.

To improve adhesion of the sulfide compound to the Ti substrate, films were dried in ambient temperature and further annealed in a box furnace at 350 $^{\circ}$C for 30 min and subsequently at 450 $^{\circ}$C for 30 min.

Electrochemical measurements were carried out using a three-electrode cell with Pt foil as a counterelectrode and Ag/AgCl/KCl 4 M as reference electrode in a standard single-compartment electrochemical cell and a CH Instruments potentiostat (Model CHI720C). Additionally, 0.1 M Na_2SO_4 used as a supporting electrode, with 0.1 M Na_2SO_3 added as a hole scavenger. The electrolyte solutions were purged with ultrapure N_2 for 15 min prior to the photovoltammetry measurements.

Photovoltammetry measurements were recorded at a low scan rate of 5 mVs^{-1} in which a sweep potential was applied from -0.6 V up to +1.0 V. A manual chopper was used to create a 5s interval dark/illuminated cycles. Throughout the measurements, a radiation source (400 W Xe lamp) was kept at fixed distance from the cell (20 cm). The nominal incident photon flux at the

location of the photoelectrode was 300 mW/cm^2, measured on a Newport model 70260 Radiant Power/Energy meter combined with a probe (Newport, 70268).

3.2.7 *Kelvin-probe Measurements and Surface Photovoltage Spectroscopy*

Measurements were performed using a KP Technology APS04 instrument.[21] First, the Fermi level of the gold alloy-coated tip was determined by measuring the Fermi level of a Ag target ($E_{Fermi,Au\text{-}tip}$ = -4.61 eV). Thin film samples were studied as in the case of the photoelectrochemical experiments. A 2 mm diameter gold alloy-coated tip was vibrated above the sample surface at a fixed height (~1 mm) and amplitude (0.2 mm), with a constant frequency (70 Hz). Contact potential difference (CPD) was measured between the sample and the Kelvin probe tip after electric equilibrium was reached. Surface photovoltage (SPV) spectroscopy was performed under ambient conditions. The gold-coated Kelvin probe tip served as the reference electrode. The samples were illuminated with monochromatic light (Fiber-Lite® DC950 150W quartz halogen lamp, coupled to a monochromator).

3.2.8 *Computational Methodology*

The present calculations were performed on the framework of spin polarized density functional theory (DFT)[22-23] as implemented in the Vienna ab initio simulation package (VASP).[24-25] The exchange and correlation were treated via the generalized gradient approximation (GGA) formalized by Perdew-Burke-Ernzerhof (PBE).[26] The projector augmented plane wave (PAW) method[6] was used to describe the interaction between the core and valence electrons. The electronic basis set was expanded in terms of plane wave and a plane wave kinetic energy cutoff, E_{cut} of 600 eV was used throughout the calculation. VASP supplied standard PAW potentials were applied for La, Ce, S atoms and Ca_sv version of PAW potential for Ca atom for geometric optimization and electronic structure calculations.

The Monkhorst-Pack (MP) scheme was used to generate the k-points mesh within the first Brillouin zone. In this present calculation, a 3×3×3 k-point mesh was used for geometric optimization which gave a well converged calculation. During the geometrical optimization, the atoms in the unit cell were fully relaxed until the residual forces among the constituent atoms become less than 0.01 eV Å^{-1}. Methfessel-Paxton smearing was also used with a width of 0.002

eV for geometric optimization and tetrahedron method with Blöch corrections for density of state (DOS) calculation. Apart from using the DFT method to calculate the lattice parameters, the rotationally invariant DFT+U method[7] was also deployed. For DFT+U calculation of lattice parameters, U values of 5 eV were used for La d state and Ce f state simultaneously.

3.3 Results and Discussion

3.3.1 *Crystal Structure*

The series, $Ca(La_{1-x}Ce_x)_2S_4$, adopt the cubic Th_3P_4 structure type, which has been described previously for the end members, x = 0 and 1.[27] Neutron diffraction was employed as La and Ce cannot be easily distinguished using X-ray sources. Indeed, neutron coherent scattering cross sections of the most abundant isotopes of La, Ce, and Ca are ~8.24, 4.84, and 4.20 bm, respectively; hence, La can be easily distinguished from the other elements present.[28] The neutron diffraction patterns, shown in Figure 3-2, show that the Th_3P_4 structure type is maintained throughout the solid solution, $Ca(La_{1-x}Ce_x)_2S_4$. Furthermore, refined unit cell dimensions obey Vegard's Law with cell parameters of 8.6391(4), 8.6579(4) and 8.6717(3) Å for members with x = 0.75, 0.50 and 0.25, respectively.

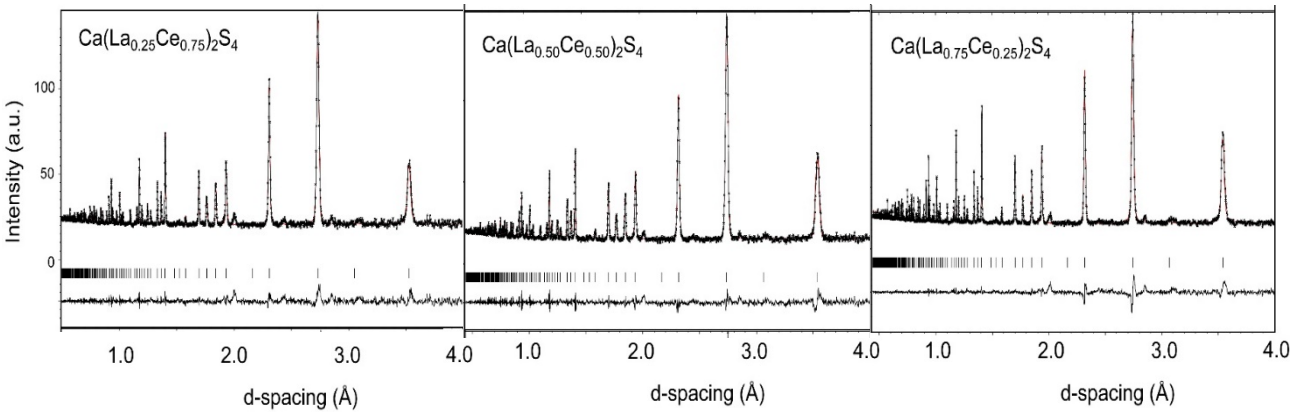

Figure 3-2. Rietveld refinements of neutron diffraction data for $Ca(La_{1-x}Ce_x)_2S_4$, x = 0.25, 0.50, 0.75. Black tickmarks and red lines represent experimental data and structural model, respectively. Calculated peaks are shown as vertical dashed lines and the difference plot is shown as black line at bottom.

Splitting of diffraction peaks was immediately observed upon analyzing synchrotron data (Figure 3-3), which has a higher resolution than neutron data. Such peak splitting is typically indicative of multiphase samples. It is important to note that

lattice parameters refined do not correspond to end members", and hence, the synthesized materials are not simply proportional mixtures of $CaLa_2S_4$ and $CaCe_2S_4$. Rather, the La and Ce mixing is chemically intrinsic for each sample. For each nominal composition, at least two phases with two unique set of unit cell parameters can be refined using synchrotron diffraction data. This two-phase model yielded reasonable statistical fits with goodness-of-fit between 1 and 2.

For the x = 0.25, 0.50 and 0.75 samples, two distinct compositional domains could be observed and assigned to a specific set of diffraction peaks. Diffraction data reveal one major and one minor domain for $Ca(La_{0.25}Ce_{0.75})_2S_4$ and $Ca(La_{0.75}Ce_{0.25})_2S_4$ whereas two quantitatively identical crystallographic domains are observed for $Ca(La_{0.50}Ce_{0.50})_2S_4$. Figures 3-3 and 3-4 present representative diffraction data collected as well as the cell parameters refined, respectively.

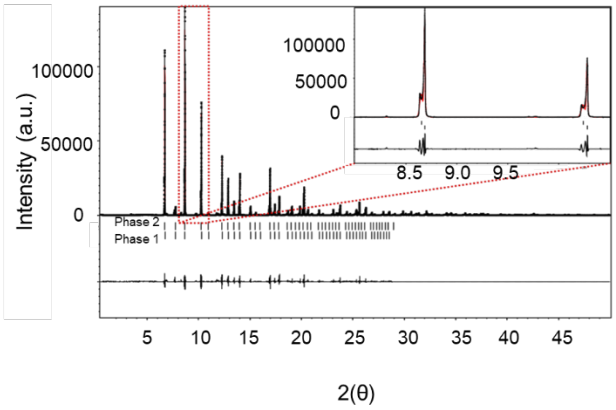

Figure 3-3. Refinement of synchrotron diffraction data for $Ca(La_{0.25}Ce_{0.75})_2S_4$. Inset: Data between 2θ are enlarged for ease of viewing peak splitting.

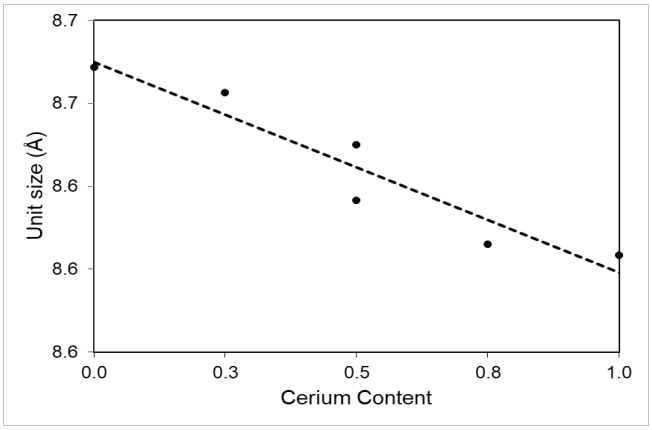

Figure 3-4. Cell parameters for $Ca(La_{1-x}Ce_x)_2S_4$ as a function of cerium content for x= 0, 0.25, 0.50, 0.75,1.0; values based on refinement of synchrotron data. For x = 0.25 and 0.75, only the major phase is included. For x = 0.50, both phases, equally intense, are included. Additional information is provided in Supporting Information (Tables 3-S1 and 3-S2).

3.3.2 *Optical Properties*

Diffuse reflectance spectroscopy (DRS) was utilized to map progressive changes in the optical properties of $CaLa_2S_4$ as Ce was introduced into the structural framework. Figure 3-5a contains the DRS data; the parent transition in the lanthanum compound centered ca. 400 nm shifts to longer wavelengths (~500-550 nm) as Ce is introduced. Tauc plots were constructed from Kunbelka-Munk transformation of the DRS data; these plots for $Ca(La_{1-x}Ce_x)_2S_4$ (Figure 3-5b), clearly show that the optical band gap is dependent upon Ce substitution, x. Although the shift from 2.15 eV in $CaCe_2S_4$ to 2.27 eV in $Ca(La_{0.25}Ce_{0.75})_2S_4$ is small, these values correspond to the visibly different colors of the corresponding materials (Figure 3-1).

To further clarify whether the x = 0.25 – 0.75 samples were simply physical mixtures of $CaCe_2S_4$ and $CaLa_2S_4$ or if the Ce and La in the materials were truly and chemically mixed at the atomic level, equal amounts of $CaCe_2S_4$ and $CaLa_2S_4$ end members were ground and pressed into a pellet. This physical mixture exhibited different optical behavior as evidenced in the DRS data in Figure3-5a. The Tauc plot shows that the band gap of the $Ca(La_{0.50}Ce_{0.50})_2S_4$ solid solution measures 2.39 eV (Figure3-5b) whereas the band gap of the physical mixture (labeled as

$CaLa_2S_4$ + $CaCe_2S_4$ – PM) clearly exhibits two peaks corresponding to 2.32 and 3.20 eV which are similar to the band gaps of $CaCe_2S_4$ and $CaLa_2S_4$, respectively (Figure 3-5a).

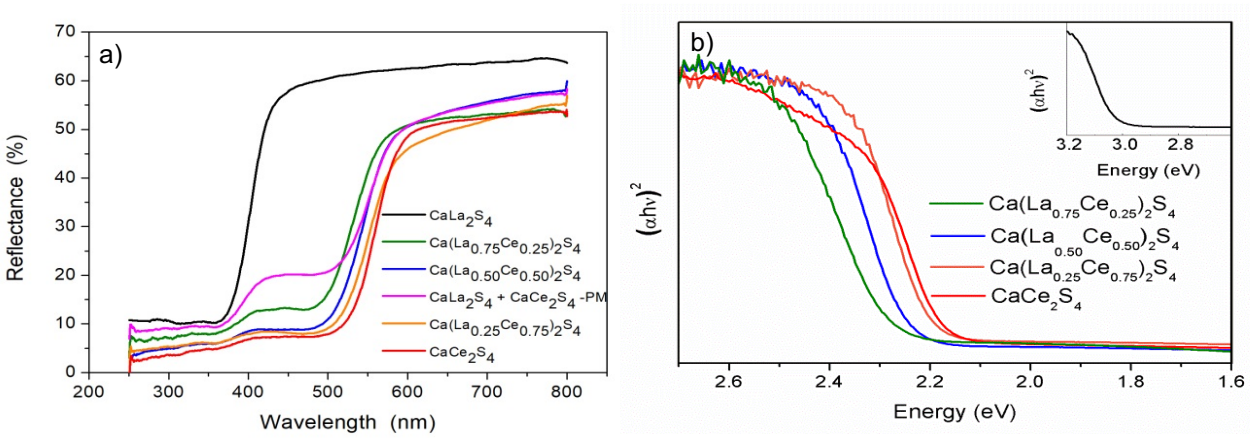

Figure 3-5. a) Diffuse reflectance data and b) Tauc plotsfor $Ca(La_{1-x}Ce_x)_2S_4$ (x = 0.25, 0.50, 0.75 and 1.0) powder, inset in b) contains the Tauc plot for $CaLa_2S_4$.

3.3.3 *DFT Results*

Table 3-S1 lists the crystallographic lattice parameters of the geometrically relaxed structures; for comparison, both the DFT and DFT+U lattice parameters are presented. Figure 3-6 shows the band structure and partial density of state of $CaLa_2S_4$. The calculated band gap is 2.06 eV and is direct. The main contribution to the valence band is from S p state and the dominant contribution to the conduction band minima is from La f states. There is hybridization between La f and d states at the bottom of the conduction band. Thus electronic transitions in $CaLa_2S_4$ will originate from the occupied S p state to unoccupied La f state. Just above the conduction band minima, there are localized bands created by La f states. The localization of La f states is indicated as a sharp peak in the partial density of states plot.

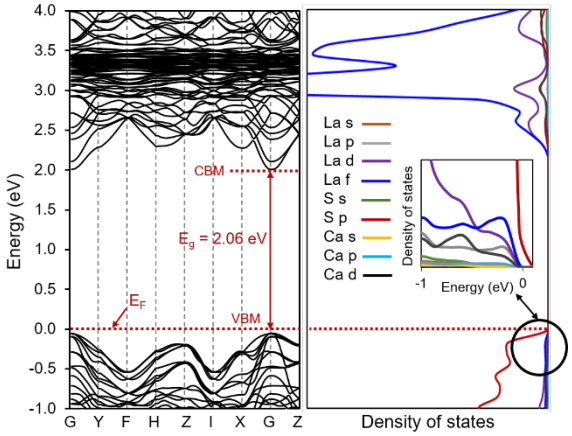

Figure 3-6.Band structure and partial density of states for $CaLa_2S_4$. The contribution of different electronic states near the Fermi level is shown in the inset. VBM and CBM correspond to valence band minimum and conduction band minimum, respectively.

Figure 3-7 presents the DFT-derived electronic band structures for the progression from x = 0, 0.25, 0.50, 0.75 and culminating in the Ce compound, $CaCe_2S_4$. The leftmost frame is reproduced from Figure 3-6, simply for comparison. The valence band maxima clearly remain unchanged from $CaLa_2S_4$. The Ce *f* states become the main contribution to the conduction band minima as this element is introduced into the $CaLa_2S_4$ structure. The Ce *f* states create a localized band at the bottom of the conduction band. The localization is indicated as a sharp peak in the partial density of states plot (not shown). Due to the introduction of Ce within $CaLa_2S_4$, the Fermi level shifts to the conduction band minima, consistent with *n*-type semiconductor behavior (see below). Cerium incorporation also creates occupied states at the bottom of the conduction band and the number of occupied states at the conduction band minima increases as the Ce level increases.

Optical transitions in Ce containing $Ca(La_{1-x}Ce_x)_2S_4$ will occur from occupied S p states to unoccupied Ce *f* states. Accordingly, the shift in the transitions see in the DRS data (Figure 3-5a) in $Ca(La_{1-x}Ce_x)_2S_4$ for x = 0.25, x = 0.50, x = 0.75 and x = 1.0 are 1.68 eV, 1.63 eV, 1.57 eV and 1.52 eV respectively and the nature of the band gap is direct. These values are lower than those derived from DRS data (see above) and also from other measurements (see below). However, such discrepancy is not uncommon between DFT and experimentally-derived band gap energies.

What is important than the absolute DFT-derived values is the trend with x. Importantly both theory and experiment yield similar trends with composition.

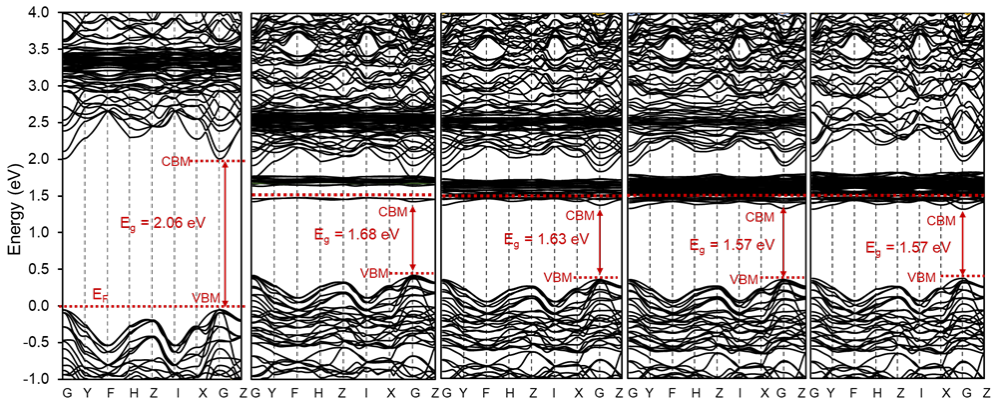

Figure 3-7. Band structure and partial density of states for x = 0.0, 0.25, 0.50, 0.75 and 1.0 of $Ca(La_{1-x}Ce_x)_2S_4$.

3.3.4 *Kelvin Probe and Surface Photovoltage Spectroscopy Results*

To determine the Fermi levels of $Ca(La_{1-x}Ce_x)_2S_4$, Kelvin-probe measurements were performed (see Figure 3-S1 for the CPD data).[22] The Fermi levels (E_F) fall close to the E_{CB} values of all four compounds (Table 3-1), which is characteristic for n-type semiconductors.[23] The E_F of $CaLa_2S_4$ is less negative, compared to the alloyed samples, which are in the same range. To better understand the optoelectronic properties, surface photovoltage (SPV) measurements were also performed. SPV is a sensitive tool to probe the wavelength-dependence of light-driven charge separation, thus it can deliver information about the bandgap, majority carrier type, defect states.[24-25] All samples gave negative photovoltage values (Figure 3-8), indicating that they behave as *n*-type semiconductors.[24-26-29] Bandgap values were calculated from the onset of the SPV spectra (Table 3-1). These values are slightly smaller, compared to those obtained from DRS measurements. The reason behind this difference is that SPV is inherently much more sensitive to *sub-bandgap* effects (such as the Franz-Keldysh effect and the photo-assisted charge transfer between shallow states extending from the bandgap 'tail states').[24] After reaching a maximum, the SP signal decreases at the lower wavelengths (except in the case of the $CaLa_2S_4$ sample where this maximum cannot be measured due to the wider bandgap) since the

top layer absorbs all the light, which no longer can penetrate to the bottom of the films to generate photovoltage.[25]

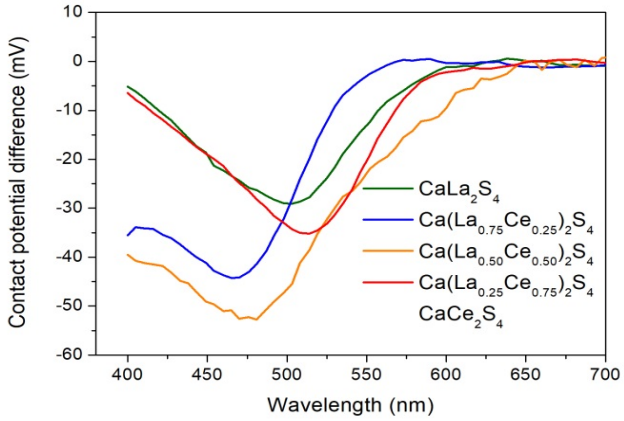

Figure 3-8. Surface photovoltage spectra recorded for $Ca(La_{1-x}Ce_x)_2S_4$ (x = 0.25, 0.50, 0.75 and 1.0) thin films on Ti substrate

Table 3-1. Bandgap (EBG) and Fermi-level (EF) values of $Ca(La_{1-x}Ce_x)_2S_4$ (x = 0.25, 0.50, 0.75 and 1.0) from DRS, KP and SPV measurements.

Sample	EBG,DRS (eV)	EBG,SPS (eV)	E_F (eV)
$CaLa_2S_4$	3.20	2.76	-4.31
$Ca(La_{0.75}Ce_{0.25})_2S_4$	2.27	2.10	-4.47
$Ca(La_{0.50}Ce_{0.50})_2S_4$	2.22	2.29	-4.56
$Ca(La_{0.25}Ce_{0.75})_2S_4$	2.20	2.13	-4.59
$CaCe_2S_4$	2.15	2.11	-4.56

3.3.5 *Photoelectrochemical Behavior*

The photoelectrochemical properties of $Ca(La_{1-x}Ce_x)_2S_4$ thin film electrodes were evaluated by means of linear sweep voltammetry under intermittent light incidence, and compared to the two end members. As shown in Figure 3-9, anodic photocurrent was observed for all samples when polarized at $E > E_{eq}$ in the presence of Na_2SO_3 as hole scavenger in solution, consistent with *n*-type semiconductor behavior (see above). While the lowest current density was observed for

$CaLa_2S_4$ (inset in Figure3-9), higher current densities were measured for cerium-containing samples. As Ce is progressively substituted for La, higher current densities were measured. The highest current density (at a fixed potential, 1.23 V vs. RHE) was observed for x = 0.50 (Figure 3-10).

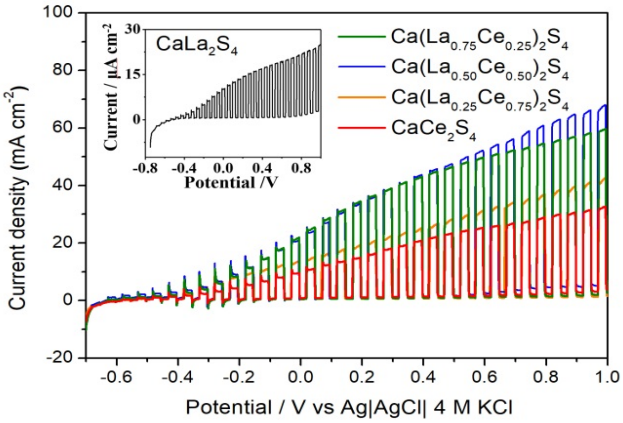

Figure 3-9. Photocurrent measurements under intermittent light incidence of thin film electrodes polarized at E > Eeq, immersed in aqueous 0.1 M Na_2SO_4 solution containing 0.1 M Na_2SO_3 as hole scavenger. Pt wire was the counterelectrode.

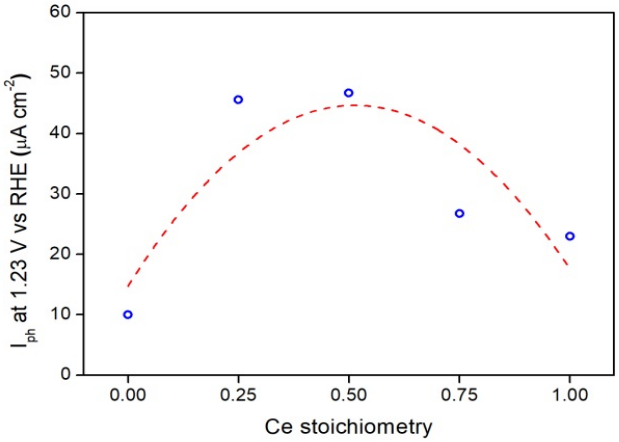

Figure 3-10. Relationship between photocurrent at 1.23 V vs RHE and cerium stoichiometry of $Ca(La_xCe_{1-x})_2S_4$ compounds. The dashed line was simply drawn as a guide to the data trend.

While incorporation of Ce was beneficial up to a point, higher amounts were clearly deleterious, and in fact, $CaLa_2S_4$ exhibited inferior activity relative to the other samples in Figures 3-8 and 3-10. Clearly, other factors (bulk carrier transport, surface electrocatalytic activity) must

play a role here; a delineation of these will require further study beyond the scope of the present one. It is also tempting to attribute the localized nature of *f* electronic states in limiting carrier transport and these states are maximally expressed in $CaLa_2S_4$ relative to the other samples. In other words, the shrinking of the energy band gap exerts a beneficial effect as Ce is first introduced. Progressive incorporation results in the manifestation of *f*-band limitations arising from their localized nature.

Butler-Gärtner plots[23] were constructed from the photoelectrochemical data and flat-band potentials were extracted from these curves (Figure 3-S2). Band positions can be estimated by combining this information with optical band gaps (Figure 3-11a). Interestingly, both optical band gaps and band positions are similar for all cerium-containing samples. Finally, Figure 3-11b combines the information derived from the Kelvin probe and photoelectrochemical measurements for mapping the band edge locations as a function of Ce content in $Ca(La_{1-x}Ce_x)_2S_4$. This energy band diagram is shown both on the vacuum and electrochemical (i.e., RHE) reference scales.

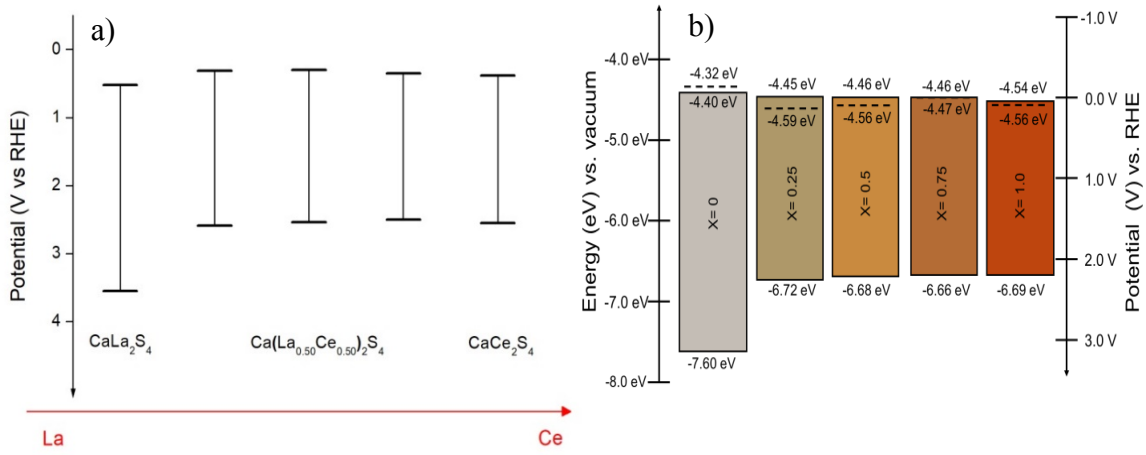

Figure 3-11. Band edge positions of $Ca(La_{1-x}Ce_x)_2S_4$ obtained by combining: (a) flat-band potentials and optical band gaps, and (b) Kelvin probe and photoelectrochemical data.

3.4 Conclusions

The new data presented here on the two end members and three solid solutions in the series, $Ca(La_{1-x}Ce_x)_2S_4$, demonstrate an effective structural framework and chemical architecture to

explore the optoelectronic role of adding *f* electrons. Clearly, the effect was striking on the first incorporation as exemplified by the x = 0.25 sample. The valence band edge immediately shifted upward resulting in a shrinking of the energy band gap from the UV range to the visible. Subsequent incorporation of Ce resulted in incremental (rather than drastic) changes in the optoelectronic behavior and electronic band structure. The photoelectrochemical data (including SPV and Kelvin probe measurements) revealed all samples to be *n*-type semiconductors regardless of the chemical composition. The location of the conduction band edge was relatively insensitive to the compound stoichiometry. However, the measured photocurrents in a redox electrolyte did vary with compound stoichiometry, peaking at a Ce level of x = 0.50.

References

1. Kanatzidis, M. G., Discovery-Synthesis, Design, and Prediction of Chalcogenide Phases. *Inorg. Chem.* **2017,** *56*, 3158-3173.
2. Flahaut, J., *Handbook on the Physics and Chemistry of Rare Earths*. Elsevier: New York, 1979; Vol. 4.
3. Cotton, S., *Lanthanide and Actinides*. Oxford University Press: New York, 1991.
4. Zhao, H.-J.; Zhong, X.-A., Synthesis, crystal structure, and optical properties of the noncentrosymmetric sulfide $Ce_8Sb_2S_{15}$. *J. Solid State Chem.* **2017,** *251*, 65-69.
5. Zhao, H.-J., Centrosymmetry vs noncentrosymmetry in $La_2Ga_{0.33}SbS_5$ and Ce_4GaSbS_9 based on the interesting size effects of lanthanides: Syntheses, crystal structures, and optical properties. *J. Solid State Chem.* **2016,** *237*, 99-104.
6. Iyer, A. K.; Yin, W.; Stoyko, S. S.; Rudyk, B. W.; Mar, A., Quaternary rare-earth sulfides Nd_7FeInS_{13} and Pr_7CoInS_{13}. *J. Solid State Chem.* **2017,** *251*, 50-54.
7. Yin, W.; Zhang, D.; Zhou, M.; Iyer, A. K.; Pöhls, J.-H.; Yao, J.; Mar, A., Quaternary rare-earth selenides $Ba_2REGaSe_5$ and $Ba_2REInSe_5$. *J. Solid State Chem.* **2018,** *265*, 167-175.
8. Feng, K.; Zhang, X.; Yin, W.; Shi, Y.; Yao, J.; Wu, Y., New Quaternary Rare-Earth Chalcogenides $BaLnSn_2Q_6$ (Ln = Ce, Pr, Nd, Q = S; Ln = Ce, Q = Se): Synthesis, Structure, and Magnetic Properties. *Inorg. Chem.* **2014,** *53*, 2248-2253.
9. Feng, K.; Shi, Y.; Yin, W.; Wang, W.; Yao, J.; Wu, Y., Ba_3LnInS_6 (Ln = Pr, Sm, Gd, Yb) and Ba_2LnGaS_5 (Ln = Pr, Nd): Syntheses, Structures, and Magnetic and Optical Properties. *Inorg. Chem.* **2012,** *51*, 11144-11149.
10. Zhao, H.-J.; Zhang, Y.-F.; Chen, L., Strong Kleinman-Forbidden Second Harmonic Generation in Chiral Sulfide: La_4InSbS_9. *J. Am. Chem. Soc.* **2012,** *134*, 1993-1995.
11. Holtzberg, F.; Methfessel, S., Rare-earth compounds with the Th_3P_4-Type structure. *J. Appl. Phys.* **1966,** *37*, 1433-1435.
12. White, W. B.; Chess, D.; Chess, C. A.; Biggers, J. V., $CaLa_2S_4$: Ceramic window mateirals for the 8 to 14 mm region. *Proc. SPIE 0297, Emerging Optical Materials* **1982**, 38-43.
13. Tomczak, J. M.; Pourovskii, L. V.; Vaugier, L.; Georges, A.; Biermann, S., Rare-earth vs. heavy metal pigments and their colors from first principles. *Proc. Natl. Acad. Sci. U. S. A.* **2013,** *110*, 904-907.
14. Perrin, M. A.; Wimmer, E., Color of pure and alkali-doped cerium sulfide: A local-density-functional study. *Phys. Rev. B* **1996,** *54*, 2428-2435.
15. Degen, T.; Sadki, M.; Bron, E.; Konig, U.; Nenert, G., The HighScore Suite. *Powder Diffraction* **2014,** *29*, S13-S18.
16. Flahaut, J.; Domange, L.; Patrie, M., Combinaisons formees par les sulfures des elements du group des terres rares. 5. vue densemble sur les systems formes part le sulfure dyttrium avec les sulfures des elements divalents. *Bull. Soc. Chim. Fr.* **1962,** *35*, 159.
17. Caglioti, G.; Paoletti, A.; Ricci, F. P., Choice of collimators for a crystal spectrometer for neutron diffraction. *Nucl. Instr. Meth. Phys. Res.* **1958,** *3*, 223-228.
18. David, W. I. F., Powder diffraction peak shapes - Parameterization of the pseudo-voigt as a voigt function. *J. Appl. Cryst.* **1986,** *19*, 63-64.
19. Petricek, V.; Dusek, M.; Palatinus, L., Crystallographic Computing System JANA2006: General F eatures. *Z. Kristallogr.* **2014,** *229*, 345-352.
20. Murphy, A. B., Band-gap determination from diffuse reflectance measurements of semiconductor films, and application to photoelectrochemical water-splitting. *Sol. Energy Mater Sol. Cells* **2007,** *91*, 1326-1337.
21. Ohtani, B., Photocatalysis A to Z—What we know and what we do not know in a scientific sense. *Journal of Photochem. Photobiol. C: Photochem. Rev.* **2010,** *11*, 157-178.
22. Baikie, I. D.; Grain, A. C.; Sutherland, J.; Lawkp, J., Ambient Pressure Photoemission Spectroscopy of Metal Surfaces. *Appl. Surf. Sci.* **2014,** *323*, 45-53.
23. Rajeshwar, K., *Electron Transfer in Chemistry*. Wiley-VCH: New York;Weinheim;, 2001.
24. Kronik, L.; Shapira, Y., Surface Photovoltage Spectroscopy of Semiconductor Structures: at the Crossroads of Physics, Chemistry and Electrical Engineering. *Surf. Interface Anal.* **2001,** *31*, 954-965.

25. Wu, P.; Wang, J. R.; Zhao, J.; Guo, L. J.; Osterloh, F. E., Structure Defects in g-C_3N_4 Limit Visible Light Driven Hydrogen Evolution and Photovoltage. *J. Mater. Chem. A* **2014,** *2*, 20338-20344.
26. Zhao, J.; Osterloh, F. E., Photochemical Charge Separation in Nanocrystal Photocatalyst Films: Insights from Surface Photovoltage Spectroscopy. *J. Phys. Chem. Lett.* **2014,** *5*, 782-786.
27. Sotelo, P.; Orr, M.; Galante, M. T.; Hossain, M. K.; Firouzan, F.; Vali, A.; Li, J.; Subramanian, M.; Longo, C.; Rajeshwar, K.; Macaluso, R. T., Ternary Rare Earth Sulfide $CaCe_2S_4$: Synthesis and Characterization of Stability, Structure, and Photoelectrochemical Properties in Aqueous Media. *J. Solid State Chem.* **2018,** *262*, 149-155.
28. Langevin, I. L., *Neutron Data Booklet*. Old City Publishing Group: 2003.
29. Kwolek, P.; Szacilowski, K., Photoelectrochemistry of n-type Bismuth Oxyiodide. *Electrochim. Acta* **2013,** *104*, 448-453.

Chapter 4 Synthesis, structure and optical properties of the solid solution series β-$(La_{1-x}Ce_x)_{10}OS_{14}$ $(0<x<1)$

Abstract

Members of the β-$(La_{1-x}Ce_x)_{10}OS_{14}$ $(0 < x < 1)$ solid solution were successfully synthesized by solid-state reaction. Rietveld refinement of single crystal samples showed a stoichiometry with 10-12% less oxygen than previously reported structure for the end members. All samples showed sharp absorption edges with band gaps ranging from 1.76 to 2.5 eV and exhibit photoluminescence with red emissions lines.

4.1 Introduction

Rare-earth oxysulfides are materials of interest from both the theoretical and the technological points of view. Their main applications lie in the optical field: laser crystals,[1] X-ray phosphors,[2] long-lasting phosphorescent materials,[3] red-emitting phosphors for TV screens,[4] etc. However, investigations on these materials have centered attention on Ln_2OS_2 and $Ln_2O_2S_3$. [5-7]

As was mentioned in previuos chapters, rare earth sulfides of the Ln_2S_3 (Ln=rare earth) family adopt five different polymorphs (α, β, γ, δ, and ε). Among these, the β polymorph ($Ln_{10}OS_{14}$) – the only one to contain oxygen – has not been characterized as with detail like the other polymorphs. In this vein and as a continuation of the study of compounds of the Ln_2S_3 family, the synthesis and optical characterization of a solid solution series of β-$(La_{1-x}Cex)_{10}OS_{14}$ $(0 < x < 1)$ are discussed in this chapter. Because lanthanum and cerium have similar oxidation states of +3 and ionic radii, it is expected that Ce^{3+} can replace La^{3+} in $La_{10}OS_{14}$ structure to form the solid solution containing both ions.

4.2 Materials and Methods

4.2.1 *Synthesis of powder samples*

Powder samples of β-$(La_{1-x}Ce_x)_{10}OS_{14}$ ($0 \leq x \leq 1$) were prepared by grinding stoichiometric ratios of α-Ce_2S_3 and α-La_2S_3 with an agate mortar and pestle. The powders were ground and placed in a graphite crucible inside of a glove box filled with circulating ultra-high purity argon. The crucibles and their contents were placed inside a fused silica ampoule and sealed under vacuum. Ampoules were heated at 7 °C/h to 900 °C, where it dwelled for 100 h, and then cooled to 25 °C at 20 °C/min. Typical yields based on mass were ~99%. Figure 4-1 shows the range of colors from lime-yellow for x = 0.0 to red burgundy for x = 1.00.

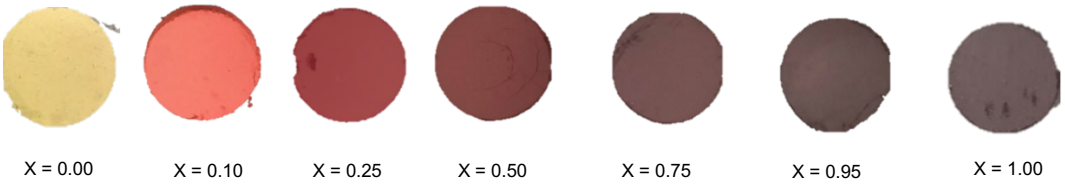

Figure 4-1 Photographs of β-$(La_{1-x}Ce_x)_{10}OS_{14}$ ($0 \leq x \leq 1$) samples showing the color variation for x = 0.00, 0.10, 0.25 0.50, 0.75, 0.95 and 1.00 compositions.

4.2.2 *Synthesis of single crystals*

Single crystals of β-$(La_{1-x}Ce_x)_{10}OS_{14}$ were prepared from the reaction of α-Ce_2S_3 and α-La_2S_3 in stoichiometric ratios. KBr flux was used to promote crystal growth. Staring materials were ground together into quartz tubes and placed in a graphite crucible that were evacuated to approximately 10^{-4} Torr and sealed. Samples were heated at 3 °C/h to 650°C, and kept at this temperature for 12 h, then heated at same rate to 950 °C where it dwelled for 96 h, and finally cooled to 25 °C at 3 °C/h.

4.2.3 *X-Ray Diffraction*

The X'Pert Plus software package[8] was employed to analyze powder X-ray diffraction data of $(La_{1-x}Ce_x)O_{10}S_{14}$ for x = 0.00, 0.10, 0.25 0.50, 0.75, 0.95 and 1.00. A previously established structural model of $LaO_{10}S_{14}$ (Ln = La-Pr)[9-10] was used as a starting model for the refinement. Global profile refinement parameters included a scale factor, a specimen displacement parameter and peak shape Cagliotti functions (U, V, W).[11] Peak shapes were fit using a pseudo-Voigt function.[12] Unit cell parameters, site occupancies, and isotropic atomic displacement parameters were refined.

Single crystal X-ray diffraction data were collected on $(La_{1-x}Ce_x)_{10}OS_{14}$ for x = 0.50. Crystals were cut to suitable sizes for data collection and mounted onto a glass fiber with epoxy. The fiber was then placed on a Bruker Apex Kappa CCD diffractometer equipped with Mo Kα radiation (λ = 0.71073 Å). Data were collected up to θ = 66.1° at 298 K. The crystal structure was solved by using the JANA2006[13] software package, data collection parameters are presented in Table 4-1.

4.2.4 *Electron Microscopy*

Electron dispersive spectroscopy measurements were performed with a Hitachi S-3000N FE scanning electron microscope. Polycrystalline samples were mounted on carbon tape and placed into an evacuated chamber. The electron beam energy was 20 kV. Scans were collected from multiple spots on several crystals. Energy-dispersive x-ray spectroscopy (EDS) analyses indicated that elemental composition was in good agreement with expected stoichiometric ratios of La and Ce. Sulfur ratio was much lower than expected; however, Rietveld refinement of powder and single X-ray diffraction data

resulted in the expected values. These results can be found in Supporting Information Table 4-S2.

4.2.5 *Diffuse Reflectance Spectroscopy*

Optical band gaps of β-$(La_{1-x}Ce_x)_{10}OS_{14}$ ($0 \leq x \leq 1$) were determined by diffuse reflectance spectroscopy (DRS) coupled with Tauc analyses.[14-15] DRS data were collected from 300 to 1000 nm using a PerkinElmer Lambda 35 spectrophotometer equipped with an integrating sphere accessory. The absorption spectrum was calculated from the reflection spectrum via the Kubelka-Munk function: $\alpha/S = (1-R)^2/2R$, where α is the absorption coefficient, S is the scattering coefficient, and R is the reflectance.[14]

4.2.6 *Photoluminescence*

Photoluminescence (PL) spectra of β-$(La_{1-x}Ce_x)_{10}OS_{14}$ ($0 \leq x \leq 1$) solid-solutions were acquired using an Ocean Optics 2000+ spectrometer with a HeCd continuous laser beam excitation (λ_{exc} = 442 nm).

4.3 Results and discussion

4.3.1 *X-Ray Diffraction*

The solid solution series β-$(La_{1-x}Ce_x)_{10}OS_{14}$ ($0 \leq x \leq 1$) crystallize in the tetragonal system with the $I4_1/acd$ space group, which has been described previously for the end members.[5, 9-10] Refinements on powder and single crystal that included a fixed La:Ce ratio produced similar statistical results, this because La and Ce possess similar atomic numbers (La = 57 and Ce = 58) to be differentiated by X-ray sources, for this reason only La was used for the purpose of Rietveld refinement analysis. However, further experiments will be the use of neutron scattering to contrast between La and Ce in the crystal structure. Figure 4-2 shows the XRD patterns of β-$(La_{1-x}Ce_x)_{10}OS_{14}$ (x = 0.00,

0.25, 0.50 and 1.00). A shift towards higher 2θ angles was observed as cerium is introduced in the structure, which can be attributed to lanthanide contraction. Unit cell dimensions obey Vegard's Law, which is shown in Figure 4-3.

Interestingly, single crystal refinement of β-$(La_{1-x}Ce_x)_{10}OS_{14}$ for x = 0.50 using a model similar to that obtained from powder X-ray diffraction refinements converged to reliability factors of R under 3%, indicating agreement of structures between the powder and single crystal samples. One significant feature was the negative values of the isotropic atomic displacement parameter (ADP) for oxygen was negative, although oxygen is the lightest atom in the compound. Therefore, the occupation of oxygen was allowed to be refined. This led to an unreasonable occupation of over 100%. Hence, we considered a mixed occupation of the 8a position with both oxygen and sulfur. The sum of their occupancies was constrained to 100% and their ADPs parameters were constrained to be equivalent. Under these conditions, the least-squares refinement resulted in reasonable and positive ADP values with 10-12% of sulfur for a final composition of $La_{10}S_{14.135}O_{0.865}$. This stoichiometry contains lower oxygen content than previously reported.[5.9]

Refining a mixed occupancy of the 8a site also satisfies interatomic distances in XRD. The expected La-S distance based on ionic crystal radii is 2.874 Å (r_{La3+} = 1.032 Å and rS^{2-} = 1.84 Å), whereas the La-O distance is calculated to be 2.382 Å (r_{O2-} = 1.35 Å).[16] By doing these some residues were observed and the refinement stabilized in a location which better satisfy the Ln-S distances corroborating the O/S mixed position in the structure.

The experimentally derived stoichiometry in this investigation gives credit to the existence of the solid solution $Ln_{10}S_{15-x}O_x$ earlier reported.[10] Atomic positions and crystallographic parameters are reported in Table 4.1

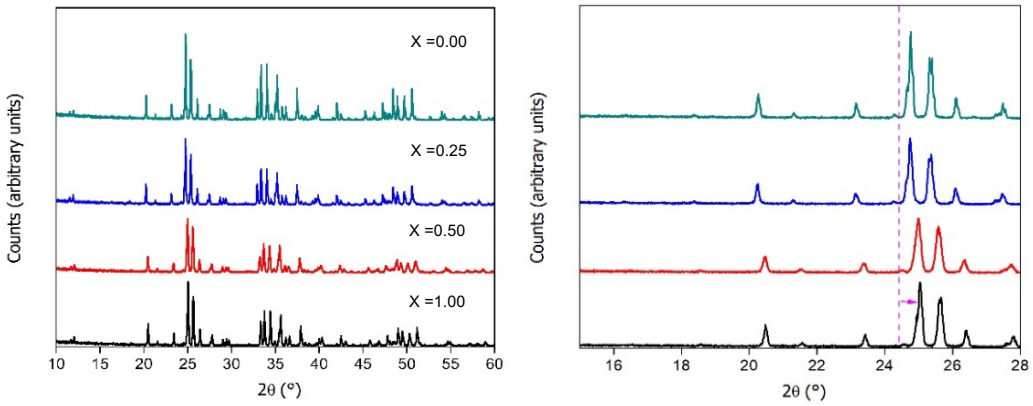

Figure 4-2. XRD patterns of β-$(La_{1-x}Ce_x)_{10}OS_{14}$ (x = 0.00, 0.25, 0.50 and 1.00), on the right a zoom in between 2θ 15° and 28°, showing a shifting to higher angles with increasing x.

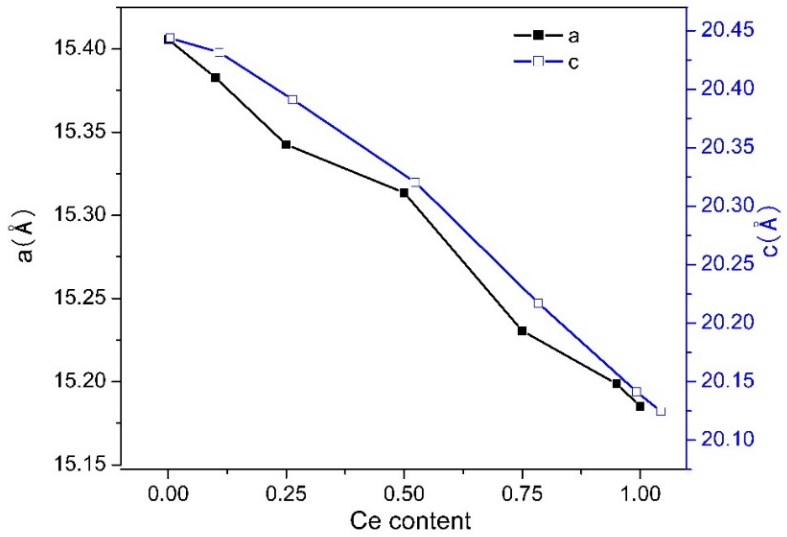

Figure 4-3. Cell parameters for β-$(La_{1-}xCex)_{10}OS_{14}$ as a function of cerium content for x= 0.00, 0.10, 0.25, 0.50, 0.75, 0.95 and 1.00; values based on refinement of powder X-ray

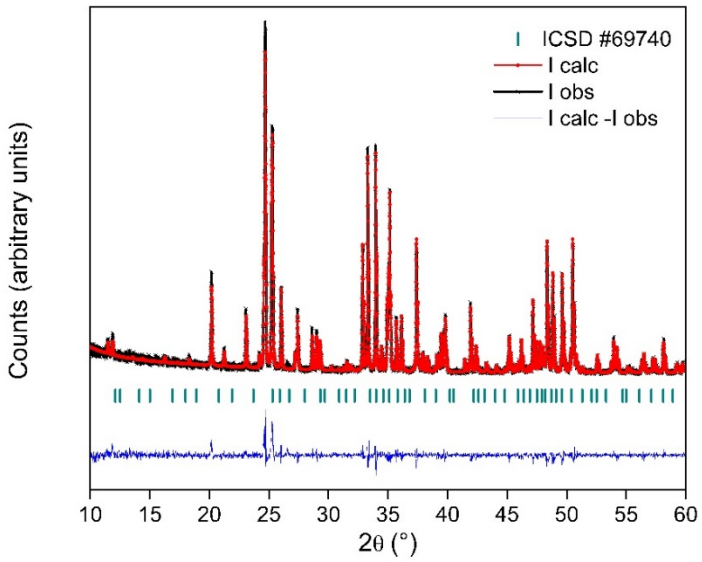

data.

Figure 4-4.Rietveld refinements of β-$La_{10}OS_{14}$. Black tickmarks and red lines represent experimental data and structural model, respectively. Calculated peaks are shown as vertical dashed lines and the difference plot is shown as a blue line.

Table 4-1. Crystallographic parameters from Rietveld refinement of single crystal for β-$(La_{1-x}Ce_x)_{10}OS_{14}$ (x = 0.50)

Chemical formula	**$La_{10}O_{0.863}S_{14.137}$**
Formula weight (g/mol)	1856.1
Temperature (K)	298
λ	0.71073 Å
Crystal dimension (mm^3)	0.01 x 0.015 x 0.01
Crystal color	Red

θ range (°)	5.2-66.1
Crystal system	Tetragonal
Space Group (No.)	$I4_1/acd$ (142)
***a* (Å)**	15.3156 (2)
***c* (Å)**	20.3169 (2)
α = β = γ (°)	90
***V* (Å)^3**	4765.7 (7)
Z	8
Density (g/cm3)	10.35
***R*[F^2>2σ(F^2)]^a**	0.0219
w*R*(F^2)^b	0.0513
GOF	1.02

$^a R_1 = \Sigma||F_o| - |F_c||/\Sigma|F_o|$

$^b wR_2 = [\Sigma [w(F_o^2 - F_c^2)^2]/\Sigma [w(F_o^2)^2]]^{1/2}$; $w = 1/[\sigma^2(F_o^2) + (0.0123\ P)^2 + 7.4140\ P]$, $[\Sigma [w(F_o^2 - F_c^2)^2]/\Sigma [w(F_o^2)^2]]^{1/2}$

Table 4-2 Final atomic coordinates of β-$La_{10}OS_{14}$ (x = 0.50), site occupancy factors and displacement parameters, with estimated standard deviations in parentheses.

Atom	Position	s.o.f.	*x*	*y*	*z*	U_{eq} (Å^2)^a
La1	32g	1	0.627 (2)	0.221 (2)	0.078 (1)	0.064 (1)
La2	16f	1	0.344 (2)	0.135 (2)	0	0.058 (1)
La3	32g	1	0.364 (2)	0.006 (2)	0.181 (1)	0.069 (2)
O	8a	0.764 (4)	0	0.5	0.25	0.030 (2)
S	8a	0.231 (2)	0	0.5	0.25	0.030 (2)
S1	32g	1	0.675(6)	0.342 (7)	-0.032 (6)	0.079 (2)
S2	32g	1	0.475(6)	0.134 (8)	0.120 (1)	0.080 (2)
S3	16e	1	0.25	0.146 (9)	0.125	0.059 (1)
S4	32g	1	0.679 (6)	0.037 (7)	0.044 (5)	0.068 (1)

The crystal structure of β-$La_{10}OS_{14}$ contain three unique La atoms (La1, La2, La3), each coordinated by eight anions to form bicapped-trigonal prisms. La1 and La2 are coordinated only to sulfur, forming LaS_8 while the local coordination environment of La3 is best described as $LaOS_7$. Figure 4-5 shows the local coordination environment of the La atoms.

Each La2 is coordinated to eight S atoms at distances between 2.891(6) Å – 3.108(1) Å, comparable to bond distance found in La_2O_2S at around 3.0252(6) Å.[17] La1 is also surrounded by eight S atoms: 7 La-S distances ranging between 2.824 Å and 3.008 Å and 1 longer La-S distance of 3.5109(7) Å, which is longer than previously observed La-S distance of ~3.02 Å.[5-6] La3 is coordinated to 7 seven S atoms in a range between 2.9601(6) - 3.512(6) Å and to one mixed O/S site by 2.516(3) Å, which is comparable to the expected La-O distance based on ionic crystal radii (2.54 Å). A similar La-O distance 2.454(1) Å has also been observed in $La_{10}OSe_{14}$.[6] The angles of La–O/S–La vary from 107.93(1)° to 112.61(2)°, close to those from 108.05° to 112.34°in $Ln_{10}OS_{14}$ (Ln = La-Nd, Sm) reported compouds.[5]

Each oxygen/sulfur atom is bound to four La atoms forming an $[(O/S)La_4$ tetrahedron, Figure 4-6 shows O/S coordination environment and the distribution of the isolated tetrahedra on the tetragonal unit cell. The $[(O/S)La]_4$ tetrahedron has been also observed in other lanthanide oxychalcogenides, such as La_2O_2S[18] and LaCuOQ for Q = S, Se and Te .[19]

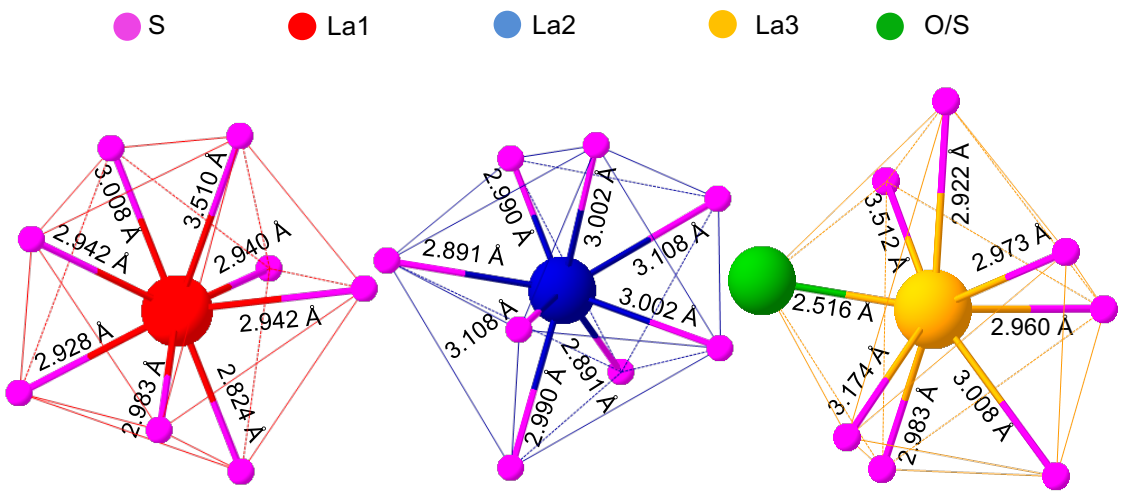

Figure 4-5. Local coordination environment of the La1, La2 and La3 forming bicapped trigonal prisms.

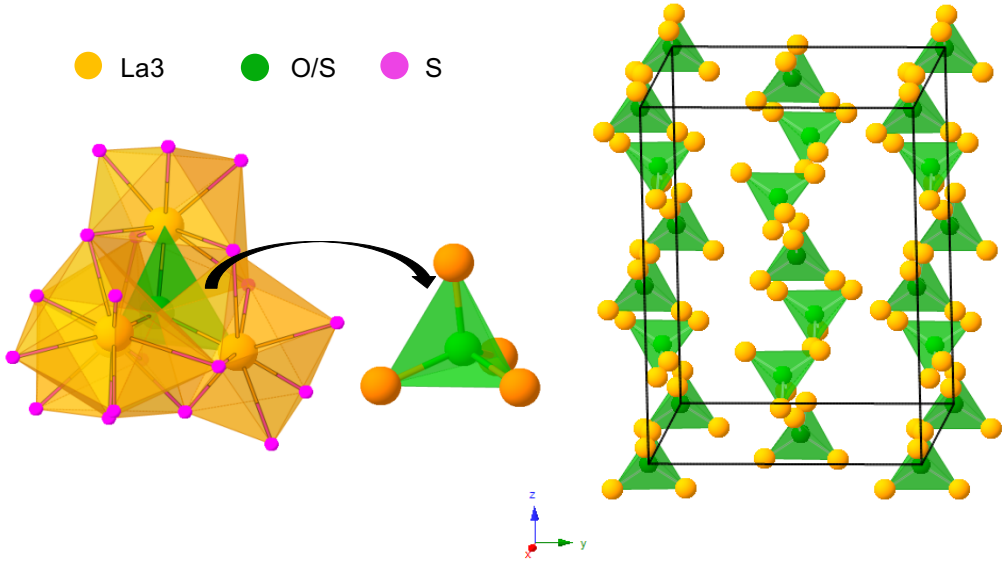

Figure 4-6. Local environment of the mixed position (O/S) forming a tetrahedron of $[(O/S)La]_4$. On the right isolated tetrahedra on the tetragonal unit cell of β-$La_{10}OS_{14}$.

4.3.2 *Optical Properties*

Diffuse reflectance spectroscopy (DRS) was utilized to observe the progressive change in the optical properties of β-$La_{10}OS_{14}$ as Ce was introduced into the structural framework. Figure 4-7 (left) contains DRS data which were used to construct Tauc plots (Figure 4-7 right) from the Kubelka-Munk function. The Tauc plots clearly show that the optical band gap decreases with increasing Ce substitution, x. Additionally, it can be observed that a small amount of Ce doping shifts the band gap from 2.52 eV in β-$La_{10}OS_{14}$ to 2.02 eV in β-$CeLa_9OS_{14}$. Band gaps values of β-$La_{10}OS_{14}$ (0<x<1) are reported in Table 4-3. Experimentally-determined band gap values obtained for the end members (x = 0.0 and x = 1.0) are in agreement with literature values[20] The band gap values obtained for the entire solid solution correspond to the visibly different colors of the corresponding materials (Figure 4-1),

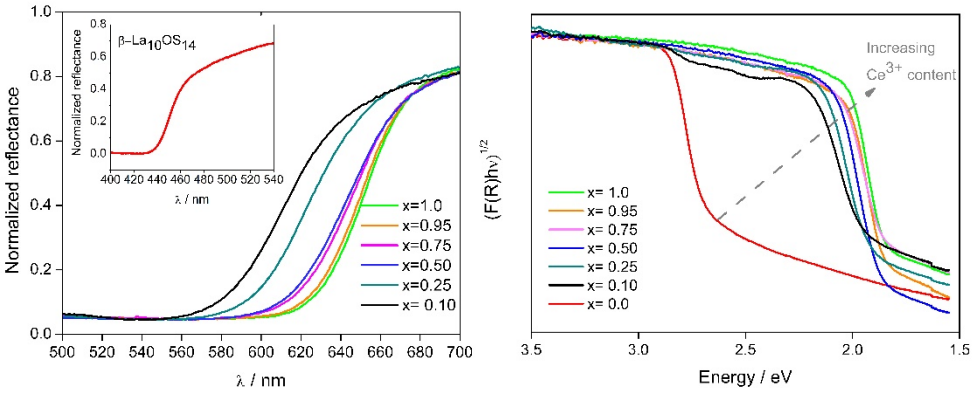

Figure 4-7. a) Diffuse reflectance data, inset in a) contains the DRS plot for β-$La_{10}OS_{14}$ and b) Tauc plots for β-$(La_{1-x}Ce_x)_{10}OS_{14}$ at different amounts of cerium doping.

Table 4-3. Bandgap (EBG) values of β-$(La_{1-x}Ce_x)_{10}OS_{14}$ from DRS measurements

x	E_{BG} (eV)
0.00	2.50
0.10	2.02
0.25	1.99
0.50	1.92
0.75	1.90
0.95	1.88
1.00	1.76

4.3.3 *Photoluminescence Results*

Photoluminescence (PL) spectra of β-$(La_{1-x}Ce_x)_{10}OS_{14}$ solid-solutions as a function of cerium content is shown in Figure 4-8. Two phosphorescence emission bands were observed for the β-$Ce_{10}OS_{14}$ green-curve in the Figure 4-8, centered at λ_{PL} = 540 nm and 660 nm, which can be assigned to charge transfer (CT) processes between oxygen (O^{2-}) 2p and sulfur (S^{2-}) 3p and Ce^{3+} 4*f* orbitals in the valence and conduction bands, respectively.[20] These results obtained were in good agreement with the strong phosphorescence emission observed between the green (λ_{PL} ≈ 515 nm)[21-22] and red (λ_{PL} ≈ 630 nm)[22-23] on cerium oxide (Ce_2O_3) and cerium sulfide (Ce_2S_3) compounds observed by other authors.

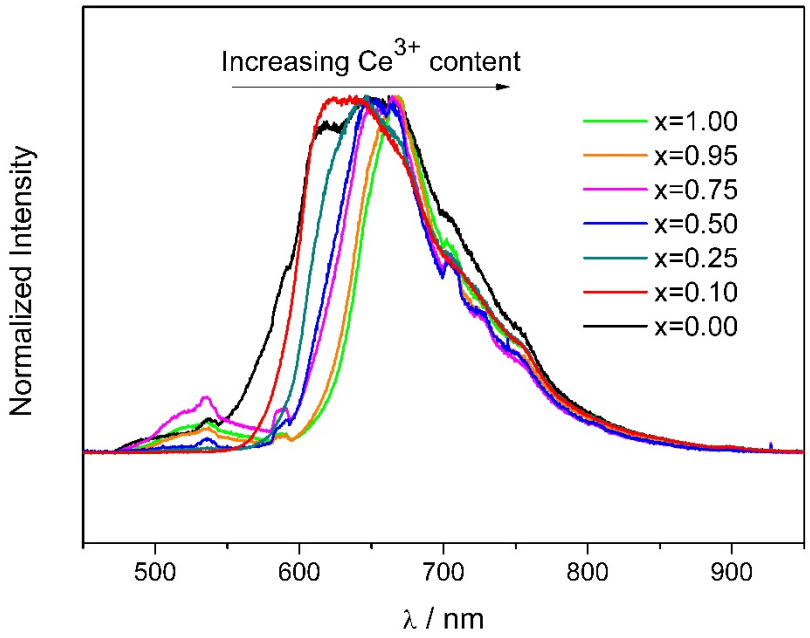

Figure 4-8. Normalized photoluminescence spectra of β-$(La_{1-x}Ce_x)_{10}OS_{14}$ as a function of cerium content for x= 0.00, 0.10, 0.25, 0.50, 0.75, 0.95 and 1.00; supported in glass (λ_{exc} = 442 nm).

In general a red-shift of the lowest energy PL band and a narrowing of its bandwidth were observed as Ce content was incorporated into the structure, which can be directly linked to changes on the materials electronic structure. The same trend on the photophysical properties was observed in the DRS and band gaps. This could be correlated to the increase of *f*-electron density in the system by Ce doping, however, further investigation needs to be done to understand the role of *f*-electron in this system.

4.4 Conclusions

Powder and single crystal samples of β-$(La_{1-x}Ce_x)_{10}OS_{14}$ solid solution series were systematically prepared via solid state reaction at a temperature of 950 ° C. Compared to previous structure determinations, Rietveld refinement of single crystals showed a lower oxygen content in the structure. Nevertheless, Neutron scattering is suggested for a clear determination of La and Ce in the crystal structure. Diffuse reflectance spectroscopy and photoluminescence analyses indicated that Ce^{3+} incorporation into the structure framework has an effect in the electronic structure, however, for a complete interpretation of these results, time-resolved optical techniques (time-correlated single-photon counting and transient absorption) and DFT calculation need to be employed in order to understand the correlation between the photophysical behavior with the composition of the La/Ce mixed-oxysulfides.

References

1. R.V. Alves, R.A. Buchanan, K.A. Wickersheim, E.A.C. Yates. Neodymium‐activated lanthanum oxysulfide: a new high gain laser material *J. Appl. Phys*.,**1971,** *42,* 3043-3048.
2. M. Nikl Scintillation detectors for x-ray.Meas. Sci. Technol., **2006**, *17*, R37-R54
3. B. Liu, C.S. Shi, Z.M. Qi J. White-light long-lasting phosphorescence from Tb^{3+}-activated Y_2O_2S phosphor.*Phys. Chem. Solids*, **2006**, *67,* 1674-1677
4. A. Abdelkader, M.M. Elkholy. Application studies on red-light emitting ZnS-CdS and $Y_2O_2S:Eu^{3+}$ phosphors used in cathode-ray tube screens for television *J. Mater. Sci.: Mater. Electron*., **1990,** *1,* 95-99
5. Schleid, T.; Lissner, F., $M_{10}S_{14}O$-Type oxysulfides (M = La, Ce, Pr, Nd, Sm) as an oxygen trap in oxidation reactions of reduced lanthanide chlorides with sulfur. *J Less Common Met*. **1991**, *175,* 309-319.
6. Zachariasen, W. H., Crystal chemical studies of the 5f-series of elements . On the crystal chemistry of uranyl compounds and of related compounds of transuranic elements. *Acta Cryst.* **1954,** *7*, 795-799.
7. Ostorero, J.; Leblanc, M., Room-temperature structure of La_2O_2S. Acta Cryst. C 1990, *46,* 1376-1378.
8. Degen, T.; Sadki, M.; Bron, E.; Konig, U.; Nenert, G., *The HighScore suite. Powder Diffraction*. **2014**, *29,* S13-S18.
9. Besancon, P., Oxygen content and exact formula of a family of compounds usually called beta-variety or complex phase of rare-earth sulfides. *J. Solid State Chem.* **1973,** *7,* 232-240.
10. Besancon, P.; Carre, D.; Laruelle, P., Mechanism of solid-solutions of rare-earth oxysulfides $La_{10}S_{15-x}O_X$. *Acta Cryst.* B **1973**, *29 ,* 1064-1066.
11. Caglioti, G.; Paoletti, A.; Ricci, F. P., Choice of collimators for a crystal spectrometer for neutron diffraction. Nucl. Instr. Meth. *Phys. Res.* **1958,** *3,* 223-228.
12. David, W. I. F., Powder diffraction peak shapes -Parameterization of the pseudo-voigt as a voigt function. *J. Appl. Cryst.* **1986,** *19,* 63-64.
13. Petricek, V.; Dusek, M.; Palatinus, L., Crystallographic Computing System JANA2006: *General F eatures. Z. Kristallogr.* **2014,** *229,* 345-352.
14. Murphy, A. B., Band-gap determination from diffuse reflectance measurements of semiconductor films, and application to photoelectrochemical water-splitting. *Sol. Energy Mater Sol. Cells*. **2007,** *91*, 1326-1337.
15. Ohtani, B., Photocatalysis A to Z—What we know and what we do not know in a scientific sense. *J. of Photochem. Photobiol*. Rev. **2010,** 11, 157-178.
16. Shannon, R. D. and Prewitt, C. T. Effective ionic radii in oxides and fluorides. *Acta Cryst.* **1969**, *25,* 925-946.
17. Ikeue, K.; Ando, S.; Mitsuyama, T.; Ohta, Y.; Arayama, K.; Tsutsumi, A.; Machida, M., Photocatalytic property and electronic structure of lanthanide-based oxysulfides. *Top. Catal*. **2008,** *47,* 175-180.
18. Morosin, B.; Newman, D. J.: La_2O_2S structure refinement and crystal field. *Acta Cryst*. **1973**, *4*, 2647-2648.

19. Popovkin, B. A.; Kusainova, M. A.; Dolgikh, V. A.; Akselrud, L. G.: New layered phases of the $MOCu_X$ (M = Ln, Bi; X = S, Se, Te) Family ageometric approach to the explanation of phase stability. *Russ. J. Inorg. Chem.* **1998,** *43*, 1471-1475.
20. Yuan, H. B.; Zhang, J. H.; Yu, R. J.; Su, Q., Synthesis of rare earth sulfides and their UV-vis absorption spectra. *J. Rare Earths.* **2009,** *27*, 308-311.
21. Deus, R. C.; Cortés, J. A.; Ramirez, M. A.; Ponce, M. A.; Andres, J.; Rocha, L. S.
22. R.; Longo, E.; Simões, A. Z. Photoluminescence Properties of Cerium Oxide Nanoparticles as a Function of Lanthanum Content. Mater. Res. Bull. 2015, *70,* 416–423.
23. Deus, R. C.; Foschini, C. R.; Spitova, B.; Moura, F.; Longo, E.; Simões, A. Z. Effect of soaking time on the photoluminescence properties of cerium oxide nanoparticles. Ceram. Int. 2014, *40*, 1–9.
24. Ephraim, B.; Ward, R. Luminescence and conduction in solid solutions of cerium sulfide in strontium sulfide. J. Electrochem. Soc. 1949, *96*, 297–303.

Chapter 5 General Summary

In this work, we targeted two solid solution materials that were promising candidates for photocatalysis and photoluminescence applications. A more environmentally friendly synthetic method, utilizing a solid state route, without the use of corrosive gases is reported.

Chapters 2 and 3 describe the study of the rare earth sulfides $Ca(La_{1-x}Ce_x)_2S_4$. Chapter 4 describes the rare earth of oxysulfides β-$(La_{1-x}Ce_x)_{10}OS_{14.}$ The structural details of the studied solid solutions were established via X-ray and neutron diffraction and are described in their relevant chapters.

All the rare earth sulfides of the $Ca(La_{1-x}Ce_x)_2S_4$ system maintained the cubic Th_3P_4 structure type, that was previously reported for the end members. Photoelectrochemical experiments on $Ca(La_{1-x}Ce_x)_2S_4$ revealed all samples to be *n*-type semiconductors regardless of the La/Ce ratio present in the structure. However, measured photocurrents in a redox electrolyte did vary with compound stoichiometry, suggesting that other factors such as bulk carrier transport, surface electrocatalytic activity or limitations arising from the localized nature of *f*-electrons could play a role.

On the other hand, the crystal structure of the oxysulfides β-$(La_{1-x}Ce_x)_{10}OS_{14}$, revealed by single crystal X-ray analysis, resulted in 10-12% lower oxygen content than previous structure determinations on end members. Photoluminescence analyses showed a red emission and a shift of the emitted line at 660 nm to shorter energies as more Ce^{3+} was incorporated into the structure. Nevertheless, further experiments such as time-resolved optical techniques and DFT calculations are needed to better understand the correlation between the photophysical behavior observed with La:Ce ratio.

This investigation shows that a solid solution between lanthanum and cerium in rare earth sulfide and oxysulfide systems can be exploited to understand how to control and tune energy bands based on density of *f*-electrons for optoelectronic applications.

Appendix A

Publication Information and Contributing Authors

Chapter 2. A manuscript published in Journal of Solid State Chemistry. Sotelo, P.; Orr, M.; Galante, M. T.; Hossain, M. K.; Firouzan, F.; Vali, A.; Li, J.; Subramanian, M.; Longo, C.; Rajeshwar, K.; Macaluso, R. T. 2018**,** *262*, 149-155,

Chapter 3. A manuscript published in Journal of Inorganic Chemistry. Sotelo, P; Orr, M; Galante, MT; Hossain, MK; Firouzan, F; Longo, C; Kormanyos, A; Sarker, H; Janaky, C; Huda, MN; Rajeshwar, K; Macaluso, R.T. 2019, *58*, 4553-4560. Reprinted with permission from Copyright 2019 American Chemical Society.

Chapter 4. A manuscript in preparation.

Apendix D. A manuscript published in Journal of Solid State Chemistry. Baumbach, R: Balicas L: McCandless, GT; Sotelo, P; Zhang, QR; Evans, J; Camdzic, D; Martin, TJ; Chan, JY. 2019, *269,*553-557.

Appendix B

List of abbreviations

Å: Angstrom

ADP: atomic displacement parameter

Calc: calculated

CBM: conduction gap minimum

C: Celsius

CIE: commission on Illumination

CPD: contact potential difference

CV: cyclic voltammetry

DFT: density functional theory

DRS: diffuse reflectance spectroscopy

DSC: differential scanning calorimetry

E_{BG}: energy bandgap

EDS: energy-dispersive x-ray spectroscopy

E_F: fermi level

Eg: energy gap

EQCM: electrochemical quartz crystal microgravimetry

FWHM: peak full-width at half-maximum

g: gram

IR: infrared

Min: Minute

MP: Monkhorst-Pack

NLO: nonlinear optical

NHE: normal hydrogen electrode

Obs: observed

PEC: photoelectrochemical

PEG: polyethylene glycol

PL: photoluminescence

RHE: reversible hydrogen electrode

SDT: simultaneous thermal analyzer

SPV: surface photovoltage

T: temperature

TE: thermoelectricity

TGA: thermogravimetric Analysis

UV-Vis: Ultraviolet-visible

VBM: valence band minimum

XRD: X-ray diffraction

Appendix C Supporting information

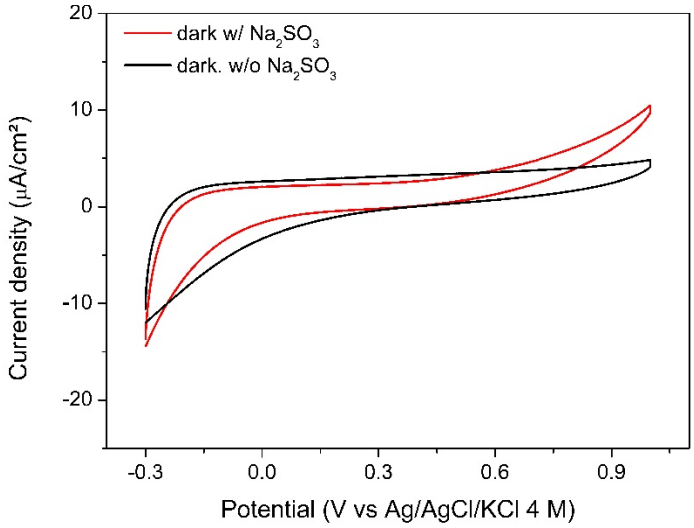

Figure 2-S1. Cyclic voltammograms registered in the dark (20 mV· s^{-1}) for the thin film Ti|$CaCe_2S_4$ electrode in 0.1 mol L^{-1} Na_2SO_4 aqueous solution (supporting electrolyte) and in supporting electrolyte containing Na_2SO_3 hole scavenger.

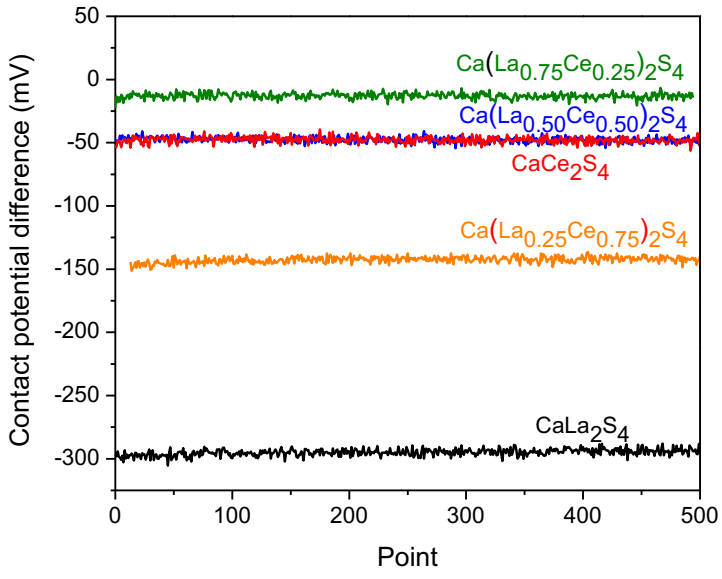

Figure 3-S1 CPD data for $CaLa_2S_4$, $Ca(La_{0.75}Ce_{0.25})_2S_4$, $Ca(La_{0.50}Ce_{0.50})_2S_4$, $Ca(La_{0.25}Ce_{0.75})_2S_4$ and $CaCe_2S_4$ samples.

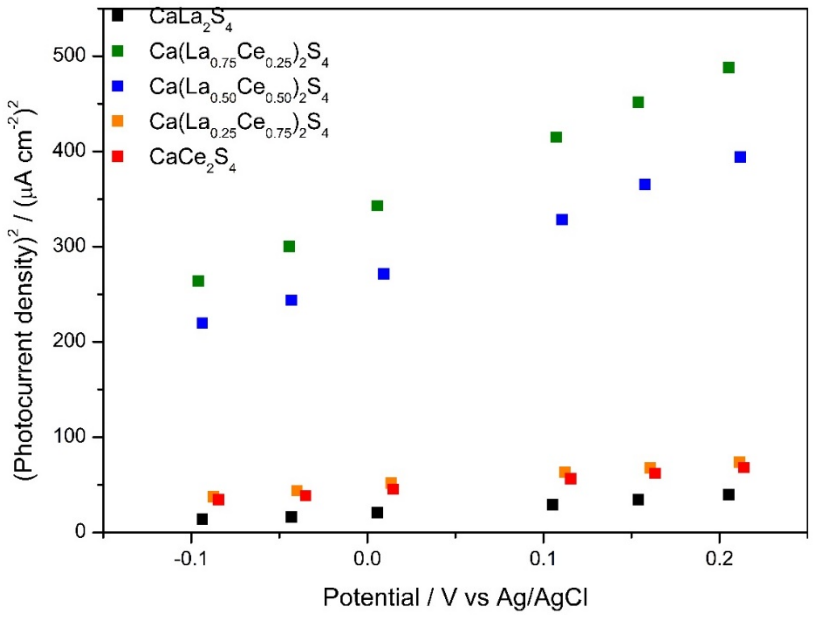

Figure 3-S2. Butler-Gärtner plots obtained from photocurrent measurements for the various $Ca(La_{1-x}Ce_x)_2S_4$ samples

Table 3-S1. Refined Unit Cell Parameters and Ratios of $Ca(La_{1-x}Ce_x)_2S_4$ (Space group $I\bar{4}3d$)

		Phase 1	Phase 2
x = 0.25	*a* (Å)	8.6489 (2)	8.674(11)
	Quantitative Ratio	6.66	93.34
x = 0.50	Quantitative Ratio	8.6364(2)	8.665(2)
	a (Å)	52.02	47.98
x= 0.75	*a* (Å)	8.62265(9)	8.670(2)
	Quantitative Ratio	88.09	11.91

Table 3-S2. EDS Results for $Ca(La_{1-x}Ce_x)_2S_4$

	$CaLa_2S_4$	**$Ca(La_{0.75}Ce_{0.25})_2S_4$**	**$Ca(La_{0.50}Ce_{0.50})_2S_4$**	**$Ca(La_{0.25}Ce_{0.75})_2S_4$**	**$CaCe_2S_4$**
Ca	1.0(1)	0.9(2)	0.9(3)	0.9(2)	1.0(7)
La	2.3(4)	1.2(3)	1.1(5)	0.7(3)	--
Ce	--	0.4(3)	0.7(5)	1.2(3)	2.4(3)
S	3.6(1)	4.0(3)	4.0(5)	4.0(3)	3.9(1)

Table 3- S3. Results from Synchrotron Powder Diffraction Data

Radiation Source	**Synchrotron, X-ray**		
Chemical formula	$Ca(La_{0.25}Ce_{0.75})_2S_4$	$Ca(La_{0.50}Ce_{0.50})_2S_4$	$Ca(La_{0.75}Ce_{0.25})_2S_4$
Formula weight (g/mol)	447.953	447.348	446.743
Temperature (K)	298		
Wavelength (Å)	0.414555	0.41273	0.414555
Crystal system	Cubic		
Space group (No.)	*I4̄3d (220)*		
a = b = c (Å)	Phase 1: 8.06489(2) Phase 2: 8.6742(1)	Phase 1: 8.06364(2) Phase 2: 8.6658(2)	Phase 1: 8.62265(9) Phase 2: 8.6709(2)
α = β = γ	90	90	90
V (Å)^3	Phase 1: 524.56021(2) Phase 2: 652.66195(2)	Phase 1: 524.31634(2) Phase 2: 650.76769(2)	Phase 1: 641.98744(9) Phase 2: 651.91734(2)
Z	4	4	4
***d*-space range (Å)**	0.4-4.5		
χ^2	2.07	2.74	2.12
Rp	7.69	8.57	6.92
Rwp	7.81	8.89	7.34

$Rp = \Sigma\ |y_{io} - y_{ic}| / \Sigma\ y_{io}$

Table 3-S4. Results from Neutron Powder Diffraction Data

Radiation Source	**Neutron**		
Chemical formula	$Ca(La_{0.25}Ce_{0.75})_2S_4$	$Ca(La_{0.50}Ce_{0.50})_2S_4$	$Ca(La_{0.75}Ce_{0.25})_2S_4$
Formula weight (g/mol)	447.953	447.348	446.743
Temperature (K)		298	
Wavelength (Å)		1.066	
Crystal system		Cubic	
Space group (No.)		*$I\bar{4}3d$ (220)*	
***a* = *b* = *c* (Å)**	8.6390(3)	8.6576(4)	8.6716(3)
α = β = γ (°)	90	90	90
***V* (Å)^3**	644.7486(3)	648.9221(4)	652.0752(3)
Z	4	4	4
***d*-space range (Å)**		0.4-4.5	
χ^2	1.98	2.09	1.78
Rp	3.59	4.42	3.14
Rwp	3.20	4.62	2.65

$Rp = \Sigma\ |y_{io} - y_{ic}| / \Sigma\ y_{io}$

Table 4-S1. Crystallographic parameters from Rietveld refinement on powder samples of β-$(La_{1-x}Ce_x)_{10}OS_{14}$ (x = 0.00, 0.1, 0.25, 0.50, 0.75, 0.95, 1.00)

Chemical formula	**$La_{10}OS_{14}$**	**X=0.10**	**X=0.25**	**X=0.50**	**X=0.75**	**X=0.95**	**$Ce_{10}OS_{14}$**
Formula weight (g/mol)	1853.9	1955.16	1856.97	1860.00	1863.03	1865.45	1866.06
Temperature (K)	298						
Crystal system	Tetragonal						
Space Group (No)	*I*41 /acd (142)						
***a* (Å)**	15.405 (8)	15.382 (7)	15.342 (5)	15.313 (6)	15.230 (6)	15.198 (7)	15.185 (2)
***c* (Å)**	20.443 (3)	20.431 (1)	20.391 (2)	20.320 (4)	20.217 (1)	20.141 (2)	20.124 (5)
α =β = γ (°)	90	90	90	90	90	90	90
***V* (Å)^3**	4852.08 (8)	4834.09	4799.56	4764.79	4689.37	4652.15	4640.27
Rp	3.37	6.48	4.72	5.64	3.89	4.71	3.54
wRp	10.11	10.26	11.65	11.337	12.35	10.47	9.12
GOF	1.22	0.82	0.99	0.96	0.85	1.17	0.99

Table 4-S2. EDS Results for β-$(La_{1-x}Ce_x)_{10}OS_{14}$ (x = 0.00, 0.1, 0.25, 0.50, 0.75, 0.95, 1.00),

	β-$(La_{1-x}Ce_x)_{10}OS_{14}$													
	$La_{10}OS_{14}$		x = 0.10		x = 0.25		x = 0.50		x = 0.75		x = 0.95		$Ce_{10}OS_{14}$	
	mol	DS	mol	DS	mol	DS	mol	DS	mol	DS	mol	DS	mol	DS
S	14	± 0.02	15	± 0.05	10.7	± 0.07	9.5	± 0.04	8.8	± 0.05	9.5	± 0.03		± 0.05
La	9.7	± 0.03	9.0	± 0.09	7.83	± 0.03	5.0	± 0.01	1.8	± 0.06		± 0.04	9.82	
Ce					2.44		5.2	± 0.07	7.5	± 0.03	9.7	± 0.04	14.5	± 0.05

Apendix D Other projects: One-dimensional tellurium chains: Crystal structure and thermodynamic properties of $PrCu_xTe_2$ (x ~ 0.45)

Abstract

X-ray diffraction, crystal structure, magnetization, and heat capacity results are presented for the rare earth – chalcogenide ternary system $PrCu_{0.45}Te_2$ and its non-4*f* analogue $LaCu_{0.40}Te_2$. The crystal structure of $PrCu_{0.45}Te_2$ is characterized by chains of edge and corner-sharing $CuTe_4$ tetrahedra and Pr centered in polyhedra comprised of Cu and Te. The Cu site is partially occupied and exhibits signatures of local disorder. Magnetic susceptibility measurements show a Curie-Weiss temperature dependence consistent with a Pr^{3+} state. No magnetic ordering is observed down to 1.8 K, but the negative Curie-Weiss temperature suggests an antiferromagnetic exchange interaction. Importantly, the low temperature heat capacity of $PrCu_{0.45}Te_2$ is strongly enhanced by comparison to $LaCu_{0.40}Te_2$, suggesting that there is a build-up of entropy that is associated with the 4*f*-electrons from the Pr^{3+} ions. These features reveal possible spin frustration behaviour and introduce this family of materials as a template for studying new phenomenon.

Introduction

The study of low-dimensional solids is of recent interest due to their fascinating electrical, magnetic, optical and thermal properties. The vast bonding motifs of chalcogenides offer a platform to investigate the relationships between dimensionality and physical properties.[1-5] Tellurium-containing intermetallic compounds are known for their charge density waves[6-8] and are strong candidates for mixed conductor, phase switching materials[2,9] and thermoelectrics.[10-12] Recently, WTe_2 has been shown to exhibit extremely large magnetoresistance (452,000%)[13] and superconductivity upon application of pressure[14], and more recently, dichalcogenides such as WTe_2, γ-$MoTe_2$, and $PdTe_2$, to correspond to realizations of Weyl and Dirac semiconductors.[15-19]

The covalent nature of one-dimensional telluride chains can lead to low-dimensional, anisotropic behavior,[4] and reversible redox switching by electrochemical routes.[20] Quasi one-dimensional structural $PdTe_4$ units in $Ta_4Pd_3Te_{16}$ leads to superconductivity.[21] Other examples of one-dimensional Te chains include $Ba_2Cu_{4-x}Te_5$[22], $CsTiUTe_5$,[23] $CsTh_2Te_6$[24] and $Gd_3Cu_2Te_7$[25]. One-dimensional Te chains are expected to result in metallic behavior; however, many compounds such as $LnCu_xTe_2$ (Ln = La, Nd, Sm, Gd, Dy; $x < 0.4$),[26] exhibit semiconducting behavior. Many such materials are also rich environments to study the influence of the *f*-electron state on electrical transport and thermodynamic properties. For instance, both CeSb[27]and CeSbSe,[28] which crystallize in distinct structures, exhibit devil's staircase magnetic behavior that results from a complex interplay between the f-states and the low charge carrier densities of these systems. In addition, the recent work on CeSbTe has been shown to be a first nonsymmorphic magnetic topological semimetal.[29]

In this work, we present the synthesis, crystal structure, magnetic properties, and heat capacity of $PrCu_{0.45}Te_2$. The crystal structure is characterized by $CuTe_4$ tetrahedral

units that are connected along the *c*-axis through a quasi-one dimensional network of Te atoms. The lanthanide atoms are arranged in bicapped trigonal prisms that are composed of Te atoms, where the nearest neighbor lanthanide distance is ~ 4.5 Å, i.e., larger than the Hill limit. There is strong disorder on the Cu site that is associated with partial filling. A Curie-Weiss temperature dependence is observed in magnetic susceptibility measurements, revealing that the Pr ions are in the magnetic trivalent state. No magnetic ordering is observed down to 1.8 K, but the negative Curie-Weiss temperature suggests an antiferromagnetic exchange interaction. The low temperature heat capacity of $PrCu_{0.45}Te_2$ is strongly enhanced in comparison to $LaCu_{0.40}Te_2$, suggesting that there is a build-up of entropy that is associated with the free spins of the 4*f*-electrons from the Pr^{3+} ions. This reveals possible spin frustration behaviour and brings new interest to this family of materials.

Experimental

Synthetic Procedures

Single crystals of $PrCu_{0.45}Te_2$ and $LaCu_{0.40}Te_2$ were grown from their constituent elements. Pr/La (rod, 99.9 %) were filed inside of a N_2-filled glove box while Cu (shot, 99.999 %), and Te (shot, 99.5 %) were used as received. The crystal growth was accomplished in two steps. In the first step, a mixture of 1 mol Pr : 2 mol Cu : 3 mol Te were placed in an alumina crucible. The crucible and its contents were subsequently placed in an amorphous silica tube, evacuated and backfilled with of Ar three times before a final evacuation and sealing using a hydrogen torch. The sealed vessel was then heated to 950 °C at a rate of 0.4 °C/min and dwelled there for 1 h before being cooled to room temperature at a rate of 0.1 °C/min. The resulting powder was then ground with excess KI in an agate mortar and pestle for the second step. The mixture was placed in an amorphous silica tube, evacuated and backfilled with of Ar three times

before a final evacuation and sealing using a hydrogen torch. The sealed vessel was then heated to 950 °C at a rate of 0.4 °C/min and dwelled there for 72 h before being cooled to 300 °C at a rate of 0.1 °C/min. The sample was removed from the furnace after dwelling at 300 °C for at least 24 h. The synthesis produced black single crystals of $PrCu_{0.45}Te_2$ with lengths ranging from ~ 0.75 to ~ 2.0 mm and a yield of approximately 60 % and black single crystals of $LaCu_{0.40}Te_2$ single crystals with dimensions < 1 mm. Crystals were soaked in distilled water to remove excess KI.

Alternatively, powders of $LaCu_{0.40}Te_2$ were produced by placing a mixture of 1 mol La : 2 mol Cu : 2 mol Te in an alumina crucible and subsequently into an amorphous silica tube. The tube was then evacuated and backfilled with of Ar three times before a final evacuation and sealing using a hydrogen torch. The sealed vessel was then heated to 1050 °C at a rate of 0.8 °C/min and dwelled there for 24 h before being cooled to 600 °C at a rate of 0.1 °C/min.

Elemental Analysis

Single crystals of $PrCu_{0.45}Te_2$ were characterized by electron dispersive spectroscopy (EDS) using a JEOL JSM-6610LV microscope with JEOL GUI Software package and an Oxford Instruments INCA Energy 250 spectrometer with an X-Max 20 detector operated with Inca Micro Analysis Suite. Selected crystals were arranged on double-sided carbon tape adhered to an aluminum sample puck. Each crystal was cleaved to expose inner portions to acquire more accurate elemental analysis of the bulk sample and to avoid erroneous readings due to any surface impurities. Several spots on each crystal were analyzed for 45 s, the results from five measurements were averaged, and atomic ratios were normalized to praseodymium. The resulting elemental composition of the sample is $Pr_{1.00(1)}Cu_{0.47(8)}Te_{2.06(4)}$, similar to the composition obtained from single-crystal X-ray diffraction.

Powder and Single Crystal X-Ray Diffraction

Powder X-ray diffraction data was collected on ground single crystals of $LaCu_{0.40}Te_2$ using a Bruker D8 Advance powder X-ray diffractometer equipped with a LYNXEYE XE detector using a Cu Kα radiation source (λ = 1.54184 Å). The powder pattern is included in Supplementary Information.

A single-crystal fragment of $PrCu_{0.45}Te_2$ was cut into a suitable size (0.02 x 0.08 x 0.12 mm^3) and mounted on a glass fiber with epoxy. Data sets were collected on a Bruker D8 Quest Kappa single crystal X-ray diffractometer equipped with an IμS microfocus Mo Kα radiation source (λ = 0.71073 Å) operating at 50 kV and 1 mA. Initial models of the crystal structure were first obtained using SHELXT (intrinsic phasing method)[30] and refined using SHELXL2014. Final structure refinements include anisotropic displacement parameters and variable occupancy of the Cu site. Additional experimental details are shown in Table 1.

Magnetism and Heat Capacity

The temperature dependent DC Magnetic susceptibility $\chi = M/H$ and field dependent magnetization $M(H)$ were measured for a powder sample of $PrCu_{0.45}Te_2$ between T = 2 - 300 K using a field H = 5000 G and at T = 5 K for H < 7 T. Measurements were performed with a Quantum Design Magnetic Properties Measurement System. The temperature dependent heat capacities, C, for $LaCu_{0.40}Te_2$ and $PrCu_{0.45}Te_2$ were measured using the standard relaxation technique in a Quantum Design Physical Properties Measurement System. Measurements were performed under temperatures ranging between T = 0.4 – 50 K at zero magnetic field.

Table 1. Crystallographic data and structure refinement for $PrCu_{0.45}Te_2$

Space group	***Pbcm***
***a* (Å)**	7.652(2)
***b* (Å)**	8.451(4)
***c* (Å)**	6.234(1)

V (Å^3)	403.2(2)
Z	4
Crystal size (mm^3)	0.02 x 0.08 x 0.12
Temperature (K)	299
θ Range (°)	2.7 - 30.5
μ (mm^{-1})	28.30
Collected reflections	5471
Unique reflections	642
R_{int}	0.039
h	$-10 \leq h \leq 10$
k	$-10 \leq k \leq 11$
l	$-7 \leq l \leq 8$
$\Delta\rho_{max}$ (e Å^{-3})	2.05
$\Delta\rho_{min}$ (e Å^{-3})	-1.19
GoF	1.21
Extinction coefficient	0.0082(4)
[a]R_1 for $F^2 > 2\sigma(F^2)$	0.0195
[b]$wR_2(F^2)$	0.0476

[a]$R_1 = \Sigma||F_0| - |F_c|| / \Sigma|F_0|$

[b]$wR_2 = \{\Sigma[w(F_0^2 - F_c^2)^2]/\Sigma[w(F_0^2)^2]\}^{1/2}$

Results and Discussion

Crystal Structure

The ternary chalcogenide $PrCu_{0.45}Te_2$ is isostructural to $LnCu_xTe_2$ (*Ln* = La, Nd, Sm, Gd, Dy; $x \leq 0.4$).[26,31] The crystal structure of $PrCu_{0.45}Te_2$ from perspectives perpendicular to the *ab*- and *bc*-planes is shown in Figure 1. The Te2 atoms form quasi one-dimensional chains along the *c*-axis. Te2–Te2 bond distances decrease from 3.1558(5) Å to 3.0273(3) for $LaCu_{0.40}Te_2$ to $DyCu_{0.32}Te_2$, respectively.[26] The Te2–Te2 interatomic distance found in $PrCu_{0.45}Te_2$ is 3.1171(8) Å, which follows the Te2-Te2 distance trend in $LnCu_xTe_2$.

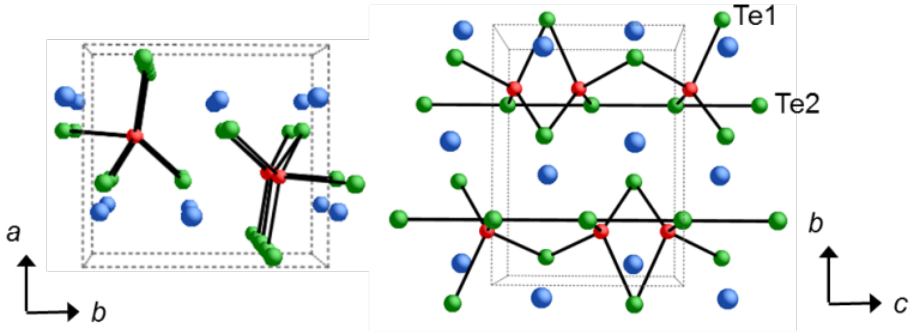

Figure 1. The structure of $PrCu_{0.45}Te_2$ down the *c*-axis on left and along the *bc*-plane on right. The one-dimensional Te chain runs along the *c*-axis. Blue, red and green spheres represent Pr, Cu, and Te, respectively.

With a cutoff distance of 3.3 Å, the Pr ions are centered in polyhedra comprised of 4 Cu, 4 Te1 and 4 Te2 atoms. The Pr-Cu distances range from 3.162(3) to 3.259(3) Å, which is similar to $PrCu_{13}$, featuring Pr-Cu distances of ~3.275 Å.[32] The 4 Pr-Te1 distances are 2 x 3.3175(7), 1 x 3.1620(10) and 1 x 3.1496(13) Å while Pr—Te2 interatomic distances measure 2 x 3.3080(8) and 2 x 3.2819(10) Å. These Pr–Te interatomic distances are similar to Pr–Te bond distances of 3.1537–3.2381 Å found in $PrTe_2$.[33]

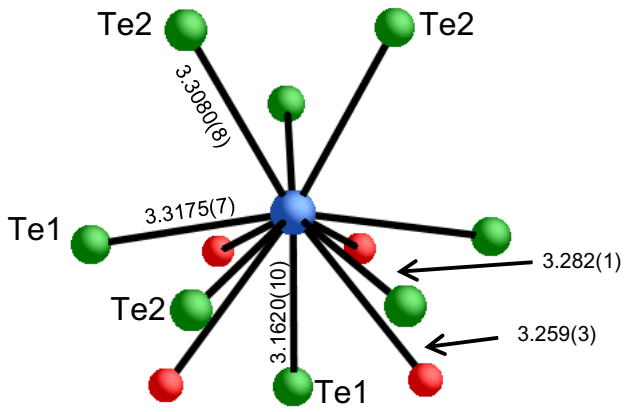

Figure 2. The coordination environment of Pr is comprised of 4 Cu, 4 Te1, and 4 Te2 atoms. Pr, Cu and Te are represented by blue, red and green spheres, respectively. Numbers represent interatomic distances in Å.

Table 2. Atomic coordinates, site occupancies, and equivalent isotropic displacement parameters for $PrCu_{0.45}Te_2$

Atom	Wyckoff Site	x	y	z	Occupancy	U_{eq}*
Pr	4*d*	0.2388(4)	0.5597(4)	¼	1.0	0.01293(13)
Cu	8*e*	0.4104(4)	0.2043(4)	0.067(6)	0.222(3)	0.0323(11)
Te1	4*d*	0.6169(5)	0.4088(5)	¼	1.0	0.01049(13)
Te2	4c	0.0793(5)	¼	0	1.0	0.01169(13)

*U_{eq} is defined as one third of the trace of the orthogonalized U_{ij} tensor

$CuTe_4$ tetrahedral units are connected by alternating edge and corner sharing Te1 atoms along the *c*-axis, as depicted in Figure 3. $CuTe_4$ tetrahedral coordination has been observed in many chalcogenides such as $RCuTe_2$ (R = Y, Gd-Lu),[10-12, 34-47] $CsCuUTe_3$,[23] $BaAg_\delta Cu_{2-\delta}Te_2$,[38] Cr_2CuX_4 (X = S, Se, Te)[39], $CsCuNd_2Se_4$[40] and $CsCuGd_2Te_4$.[41] Cu-Te bond distances in $PrCu_{0.45}Te_2$, shown in Figure 3, range from 2.595(3) Å to 2.751(3) Å, resulting in distorted $CuTe_4$ tetrahedra. These distances are similar to Cu-Te distances of 2.345 – 2.682 Å in $Ba_3Cu_{4-x}Te_5$,[42] 2.583-2.593 Å in $KCuZrTe_3$[43,] and 2.671 Å in $Cu_{0.66}EuTe_2$.[44] In $PrCu_{0.45}Te_2$ the shortest Cu-Cu interatomic distances between partially occupied, symmetry equivalent sites are only 1.145(8) and 2.273(8) Å. To the best of our knowledge, the shortest known Cu-Cu separation is 2.35 Å (in Cu(tolyl-NNNNN-tolyl)$_3$);[45] hence, it is plausible that the Cu atoms are geometrically constrained and that $CuTe_4$ tetrahedra share only corners in the local crystal structure.

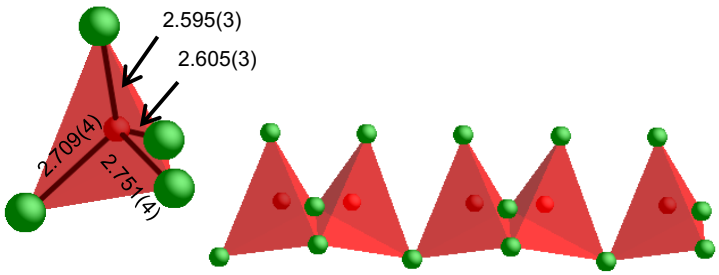

Figure 3. Left: A distorted $CuTe_4$ tetrahedron with bond distances shown in Å. Right: Edge and corner sharing $CuTe_4$ chain along the *c*-axis.

One significant observation to note is that the U_{eq} of Cu was three times larger than U_{eq} values of Pr and Te in single crystal X-ray diffraction experiments. The U_{eq} of Cu is highly anisotropic with U_{33} being approximately twice that of U_{11} and U_{22}. The ~3.21 and ~3.96 Å Cu···Cu distances in $PrCu_{0.45}Te_2$ are somewhat larger than Cu···Cu distances of ~2.8 – ~3.1 Å observed in NaCuTe[46] and $NaCu_3Te_2$[47], which contain ordered $CuTe_4$ tetrahedral chains and layers. The unusual atomic displacement parameter (ADP) of Cu may be due to the random variation of the Cu···Cu distances in the average structure. Further investigation of the local structure would provide insight into the nature of Cu bonding. It should be noted that the Cu ADP is large relative to other atoms only in $PrCu_{0.45}Te_2$. In other previously published rare-earth analogues of this structure type, the Cu ADP are similar to atomic displacement parameters of the rare-earth and Te atoms, except for the Gd and Dy analogues where the Cu ADP is approximately double the ADPs of the other atoms.[26]

Magnetic Susceptibility

The temperature dependent DC magnetic susceptibility $\chi = M/H$ and field dependent magnetization $M(H)$ were measured for a powder sample of $PrCu_{0.45}Te_2$ between T = 2 - 300 K using a field H = 5000 G and at T = 5 K for H < 7 T (Fig. 4). Across nearly the entire temperature range, the magnetic susceptibility data follow a Curie-Weiss

temperature dependence, $\chi = (C/(T-\theta))$, where C is the Curie constant and θ is the Curie-Weiss temperature (Fig. 4b). The weak deviation from this function only at low temperatures reveals that the impact of crystal electric field splitting on the magnetic state is weak. A fit to the data on the range T = 50 – 300 K yields the values C = 1.44 cm^3K/mol and θ = -11.4 K. From C, the effective magnetic moment μ_{eff} is calculated to be 3.4 μ_B, which is close to the theoretical value of 3.51 μ_B for Pr^{3+}. From this, it was concluded that the magnetism of this system is associated with the 4f-electrons of Pr and that the Cu 3d-electrons do not carry a localized moment. Although there is no evidence for magnetic ordering, the modest and negative θ has been found to provide evidence for antiferromagnetic exchange between the *f*-electron moments. The field dependence of the magnetization at T = 5 K (Fig. 4c) is consistent with this scenario, where a gradual increase with negative curvature is observed, to approach a moment near 0.9 μ_B/formula unit (F.U.) at H = 7 T.

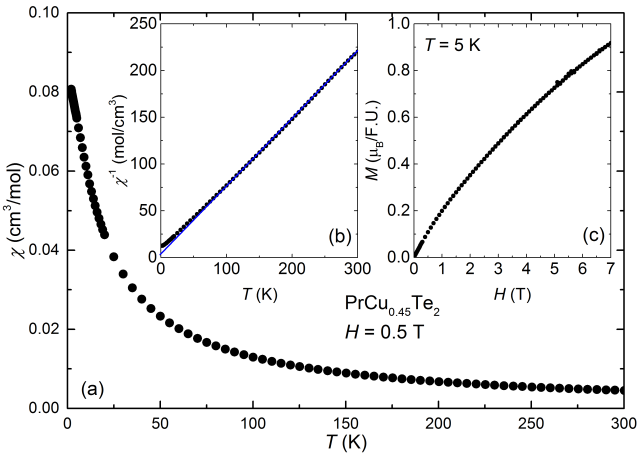

Figure 4. (a) The temperature dependent magnetic susceptibility $\chi = M/H$ vs temperature T collected in an applied magnetic field H = 0.5 T for $PrCu_{0.45}Te_2$. (b) Inverse magnetic susceptibility χ^{-1}(T). The straight blue line is a Curie-Weiss fit to the data, as described in the text. (c) Field dependent magnetization of $PrCu_{0.45}Te_2$ at 5 K.

Heat Capacity

The temperature dependence of the heat capacity divided by temperature C/T vs T for $PrCu_{0.45}Te_2$ and its nonmagnetic analogue $LaCu_{0.40}Te_2$ are shown in Fig. 5. $LaCu_{0.40}Te_2$ exhibits a typical temperature dependence, where the low T behavior follows the expression $C/T = \gamma + \beta T^2$ (γ and β are the electronic and phonon contributions to the heat capacity, respectively) with $\gamma_{La} = 3.1$ mJ/mol·K^2 and $\beta = 0.78$ mJ/mol·K^2 (Fig. 5 inset). From the non-zero value of γ_{La}, it has been concluded that there are an appreciable number of charge carriers near the Fermi energy. This is unexpected since earlier work shows that the chemical analogues exhibit semiconducting behavior, where γ would be close to zero. From the value of β, the Debye temperature has been calculated $\theta_D = 215$ K. In contrast, $PrCu_{0.45}Te_2$ exhibits a strong enhancement of C/T across the entire measured temperature range with nonmonotonic features. In particular, there is a clear but broad hump around $T_1 \approx 4$ K and a much weaker hump around $T_2 \approx 24$ K. These anomalies could indicate short range magnetic ordering. A linear extrapolation of the low temperature behaviour also suggests that $\gamma_{Pr} \approx 27$ mJ/mol·K^2, which is much larger than γ_{La}. It is natural to associate this difference with the unquenched entropy of the Pr f-moments, and similar anomalous behavior is frequently associated with the development of either spin glass states or correlated spin liquids.[48] In fact $C \propto T^2$ was reported for $Lu_2Mo_2O_7$ which is observed to display an anomalous spin glass state in the absence of any significant chemical or bond disorder.[49] Thermal transport measurements may help in understanding the nature of the heat capacity observed for $PrCu_{0.45}Te_2$.

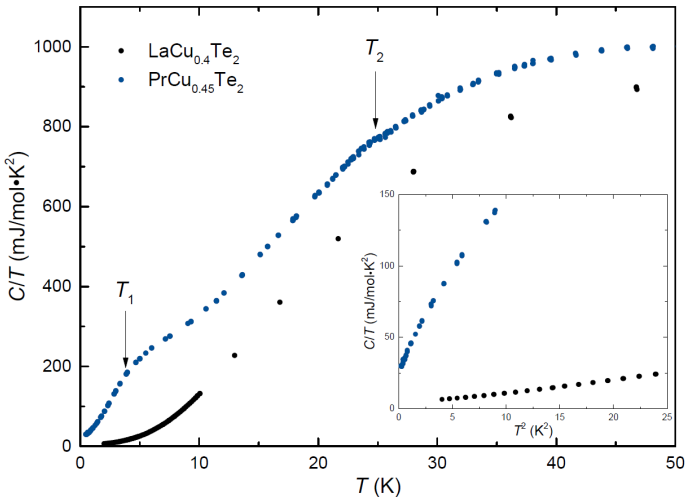

Figure 5. Comparison between the heat capacity divided by temperature C/T vs T for $LaCu_{0.40}Te_2$ and $PrCu_{0.45}Te_2$. Inset: C/T vs T^2 for both compounds.

Discussion and Conclusions

Taken together, these results expose $PrCu_{0.45}Te_2$ as a disordered magnetic semiconductor. Since the La analogue is also a semiconductor, it is clear that the electronic behaviour is a result of the band structure which does not seem to be influenced by the flat f-states which, in principle, could be near the Fermi energy. Instead, the Pr ions carry a localized trivalent moment indicating that they are well below the Fermi energy. From the viewpoint of the magnetic susceptibility, this produces a typical Curie-Weiss behaviour with a small antiferromagnetic exchange interaction on the order of θ = -11.4 K. This would lead us to expect magnetic ordering around this temperature, but instead we find no evidence for a phase transition. In its place, there is an unexpected build-up of the heat capacity that is centered around $T_1 \approx 4$ K. This may represent short range magnetic ordering resulting from magnetic frustration, but further work is needed to clarify the origin of this behaviour. It should be pointed out that theoretical calculations show that the Cu-Te interactions in $LaCu_xTe_2$ ($0.28 \leq x \leq 0.50$)

play an important role in its electronic band structure; distortions in the Te chain resulting from varying Cu concentrations resulted in a band gap opening at the Fermi energy.[50] In light of these calculations, the larger atomic displacement parameters of Cu site in our diffraction studies of $PrCu_{0.45}Te_2$ warrants further investigation into the local structure of Cu and its effects on magnetic frustration of the Pr network. It should be noted that preliminary transport measurements reveal very high resistivities suggesting that this system is also semiconducting.

References

1. Chivers, T., Tellurium compounds of the main-group elements: Progress and prospects. *Dalton Trans.* **1996,** *7,* 1185-1194.
2. Patschke, R.; Kanatzidis, M. G., Polytelluride compounds containing distorted nets of tellurium. *Phys. Chem. Chem. Phys.* **2002,** *4*, 3266-3281.
3. Seong, S.; Albright, T. A.; Zhang, X.; Kanatzidis, M., Te-Te bonding in copper tellurides. *J. Am. Chem. Soc.* **1994,** *116*, 7287-93.
4. Mitchell, K.; Ibers, J. A., Rare-earth transition-metal chalcogenides. *Chem. Rev.* **2002,** *102*, 1929-1952.
5. Mayasree, O.; Sankar, C. R.; Kleinke, K. M.; Kleinke, H., Cu clusters and chalcogen-chalcogen bonds in various copper polychalcogenides. *Coord. Chem. Rev.* **2012,** *256*, 1377-1383.
6. Malliakas, C.; Billinge, S. J. L.; Kim, H. J.; Kanatzidis, M. G., Square nets of tellurium: Rare-earth dependent variation in the charge-density wave of $RETe_3$ (RE = rare-earth element). *J. Am. Chem. Soc.* **2005,** *127*, 6510-6511.
7. Malliakas, C. D.; Kanatzidis, M. G., Charge density waves in the square nets of tellurium of $AMRETe_4$ (A = K, Na; M = Cu, Ag; RE = La, Ce). *J. Am. Chem. Soc.* **2007,** *129*, 10675-10677.
8. Snyder, G. J.; Toberer, E. S., Complex thermoelectric materials. *Nat. Mater.* **2008,** *7*, 105-114.
9. Patschke, R.; Heising, J.; Brazis, P.; Kannewurf, C. R.; Kanatzidis, M., $KCuCeTe_4$: A new intergrowth rare earth telluride with an incommensurate superstructure associated wth a distorted square net of tellurium. *Chem. Mater.* **1998,** *10*, 695-697.
10. Esmaeili, M.; Forbes, S.; Tseng, Y.-C.; Mozharivskyj, Y., Crystal structure, electronic and physical properties of monoclinic $RECuTe_2$ in contrast to $RECuSe_2$ (RE = Pr, Sm, Gd, Dy and Er). *Solid State Sci.* **2014,** *186*, 142-148.
11. Lin, H.; Chen, H.; Shen, J.-N.; Chen, L.; Wu, L.-M., Chemical modification and energetically favorable atomic disorder of a layered thermoelectric material $TmCuTe_2$ leading to high performance. *Chem. Eur. J.* **2014,** *20*, 15401-15408.
12. Lin, H.; Chen, H.; Ma, N.; Zheng, Y. J.; Shen, J. N.; Yu, J. S.; Wu, X. T.; Wu, L. M., Syntheses, structures, and thermoelectric properties of ternary tellurides: $RECuTe_2$ (RE = Tb-Er). *Inorg. Chem. Front.* **2017,** *4*, 1273-1280.
13. Ali, M. N.; Xiong, J.; Flynn, S.; Tao, J.; Gibson, Q. D.; Schoop, L. M.; Liang, T.; Haldolaarachchige, N.; Hirschberger, M.; Ong, N. P.; Cava, R. J., Large, non-saturating magnetoresistance in WTe_2. *Nature* **2014,** *514*, 205-208.
14. Kang, D.; Zhou, Y.; Yi, W.; Yang, C.; Guo, J.; Shi, Y.; Zhang, S.; Wang, Z.; Zhang, C.; Jiang, S.; Li, A.; Yang, K.; Wu, Q.; Zhang, G.; Sun, L.; Zhao, Z., Superconductivity emerging from a suppressed large magnetoresistant state in tungsten ditelluride. *Nat. Commun.* **2015,** *6*, 7804.
15. Belopolski, I.; Sanchez, D. S.; Ishida, Y.; Pan, X. C.; Yu, P.; Xu, S. Y.; Chang, G. Q.; Chang, T. R.; Zheng, H.; Alidoust, N.; Bian, G.; Neupane, M.; Huang, S. M.; Lee, C. C.; Song, Y.; Bu, H. J.; Wang, G. H.; Li, S. S.; Eda, G.; Jeng, H. T.; Kondo, T.; Lin, H.; Liu, Z.; Song, F. Q.; Shin, S.; Hasan, M. Z., Discovery of a new type of topological Weyl fermion semimetal state in $Mo_xW_{1-x}Te_2$. *Nat. Commun.* **2016,** *7*, 9.
16. Tamai, A.; Wu, Q. S.; Cucchi, I.; Bruno, F. Y.; Ricco, S.; Kim, T. K.; Hoesch, M.; Barreteau, C.; Giannini, E.; Besnard, C.; Soluyanov, A. A.; Baumberger, F.,

Fermi arcs and their topological character in the candidate type-II Weyl semimetal $MoTe_2$. *Phys. Rev. X* **2016,** *6*, 11.
17. Soluyanov, A. A.; Gresch, D.; Wang, Z. J.; Wu, Q. S.; Troyer, M.; Dai, X.; Bernevig, B. A., Type-II Weyl semimetals. *Nature* **2015,** *527*, 495-498.
18. Wang, Z. J.; Gresch, D.; Soluyanov, A. A.; Xie, W. W.; Kushwaha, S.; Dai, X.; Troyer, M.; Cava, R. J.; Bernevig, B. A., $MoTe_2$: A type-II Weyl topological metal. *Phys. Rev. Lett.* **2016,** *117*, 5.
19. Sun, Y.; Wu, S. C.; Ali, M. N.; Felser, C.; Yan, B. H., Prediction of Weyl semimetal in orthorhombic $MoTe_2$. *Phys. Rev. B* **2015,** *92*, 7.
20. Janek, J., Mixed conductors: The bridge to redox switches. *Nat. Mater.* **2009,** *8*, 88-89.
21. Jiao, W.-H.; Tang, Z.-T.; Sun, Y.-L.; Liu, Y.; Tao, Q.; Feng, C.-M.; Zeng, Y.-W.; Xu, Z.-A.; Cao, G.-H., Superconductivity in a layered $Ta_4Pd_3Te_{16}$ with $PdTe_2$ Chains. *J. Am. Chem. Soc.* **2014,** *136*, 1284-1287.
22. Mayasree, O.; Cui, Y.; Assoud, A.; Kleinke, H., Structure change via partial Se/Te substitution: Crystal structure and physical properties of the telluride $Ba_2Cu_{4-x}Te_5$ in contrast to the selenide-telluride $Ba_2Cu_{4-x}Se_yTe_{5-y}$. *Inorg. Chem.* **2010,** *49*, 6518-6524.
23. Cody, J. A.; Ibers, J. A., Uranium tellurides: New one- and two-dimensional compounds $CsUTe_6$, $CsTiUTe_5$, $Cs_8Hf_5UTe_{30.6}$, and $CsCuUTe_3$. *Inorg. Chem.* **1995,** *34*, 3165-3172.
24. Cody, J. A.; Ibers, J. A., Synthesis and structure of the layered thorium telluride $CsTh_2Te_6$. *Inorg. Chem.* **1996,** *35*, 3836-3838.
25. Huang, F. Q.; Ibers, J. A., $Gd_3Cu_2Te_7$ and $U_2Cu_{0.78}Te_6$: Two examples of linear Te chains. *J. Solid State Chem.* **2001,** *159*, 186-190.
26. Huang, F. Q.; Brazis, P.; Kannewurf, C. R.; Ibers, J. A., Syntheses, structures, physical properties, and theoretical study of $LaCu_{0.4}0Te_2$, $NdCu_{0.37}Te_2$, $SmCu_{0.34}Te_2$, $GdCu_{0.33}Te_2$, and $DyCu_{0.32}Te_2$. *J. Am. Chem. Soc.* **2000,** *122*, 80-86.
27. von Boehm, J.; Bak, P., Devil's stairs and the commensurate-commensurate transitions in CeSb. *Phys. Rev. Lett.* **979,** *42*, 122-125.
28. Chen, K. W.; Lai, Y.; Chiu, Y. C.; Steven, S.; Besara, T.; Graf, D.; Siegrist, T.; Albrecht-Schmitt, T. E.; Balicas, L.; Baumbach, R. E., Possible devil's staircase in the Kondo lattice CeSbSe. *Phys. Rev. B* **2017,** *96*, 014421.
29. Schoop, L. M.; Topp, A.; Lippmann, J.; Orlandi, F.; Müchler, L.; Vergniory, M. G.; Sun, Y.; Rost, A. W.; Duppel, V.; Krivenkov, M.; Sheoran, S.; Manuel, P.; Varykhalov, A.; Yan, B.; Kremer, R. K.; Ast, C. R.; Lotsch, B. V., Tunable Weyl and Dirac states in the nonsymmorphic compound CeSbTe. *Sci. Adv.* **2018,** *4*2, 67-70.
30. Sheldrick, G., Crystal structure refinement with SHELXL. *Acta Crystallogr., Sect. C* **2015,** *71*, 3-8.
31. Dung, N.-H.; Pardo, M.-P.; Boy, P., Single-crystal structure of copper lanthanum telluride $Cu_{0.28}LaTe_2$: a disordered tunnel structure. *Acta Cryst. Sect. C* **1983,** *39*, 668-670.
32. Bloch, J. M.; Shaltiel, D.; Davidov, D., Preparation and study of new intermetallic compounds with the $NaZn_{13}$ structure: $LaCu_{13}$, $PrCu_{13}$. *J. Less Common Met.* **1981,** *79*, 323-327.
33. Lashkarev, G. V.; Paderno, Y. B., Physical properties and chemical bond in rare-earth chalcogenides. *Izv. Akad. Nauk SSSR, Neorg. Mater.* **1965,** *1*, 1791-1802.

34. Shemet, V. Y.; Gulay, L. D.; Stepien-Damm, J.; Pietraszko, A.; Olekseyuk, I. D., Investigation of the Y_2Te_3–Cu_2Te–PbTe system at 870K and crystal structures of the $Y_7Cu_3Te_{12}$ and $YCu_{0.264}Te_2$ compounds. *J. Alloys Compd.* **2006,** *420*, 58-62.
35. Aydemir, U.; Pohls, J.-H.; Zhu, H.; Hautier, G.; Bajaj, S.; Gibbs, Z. M.; Chen, W.; Li, G.; Ohno, S.; Broberg, D.; Kang, S. D.; Asta, M.; Ceder, G.; White, M. A.; Persson, K.; Jain, A.; Snyder, G. J., $YCuTe_2$: a member of a new class of thermoelectric materials with $CuTe_4$-based layered structure. *J. Mater. Chem.* **2016,** *4*, 2461.
36. Godzhaev, E. M.; Aliev, O. M.; Mamedov, V. A.; Zarbaliev, M. M., Synthesis and study of copper lanthanide telluride ($CuLnTe_2$) compounds. *Izv. Akad. Nauk. SSSR, Neorg. Mater.* **1977,** *13*, 441-443.
37. Gulay, L. D.; Daszkiewicz, M.; Shemet, V. Y., Crystal structure of ~RCu_3S_3 and ~$RCuTe_2$ (R=Gd–Lu) compounds. *J. Solid State Chem.* **2012,** *186*, 142-148.
38. Assoud, A.; Cui, Y.; Thomas, S.; Sutherland, B.; Kleinke, H., Structure and physical properties of the new telluride $BaAg_2Te_2$ and its quaternary variants $BaCu_\delta Ag_{2-\delta}Te_2$. *J. Solid State Chem.* **2008,** *181*, 2024-2030.
39. Goodenough, J. B., Tetrahedral-site copper in chalcogenide spinels. *Solid State Commun.* **1967,** *5*, 577-580.
40. Babo, J.-M.; Strobel, S.; Schleid, T., *Z. anorg. allg. Chem.* **2010,** *636* (2), 349-355.
41. Zelinska, M.; Assoud, A.; Kleinke, H., Synthesis, crystal and electronic structure, and physical properties of the new lanthanum copper telluride $La_3Cu_5Te_7$. *J. Solid State Chem.* **2011,** *184*, 516-522.
42. Assoud, A.; Thomas, S.; Sutherland, B.; Zhang, H. Q.; Tritt, T. M.; Kleinke, H., Thermoelectric properties of the new polytelluride $Ba_3Cu_{14-d}Te_{12}$. *Chem. Mater.* **2006,** *18*, 3866-3872.
43. Mansuetto, M. F.; Keane, P. M.; Ibers, J. A., Synthesis, structure, and conductivity of the new group-IV chalcogenides, $KCuZrQ_3$ (Q = S, Se, Te). *J. Solid State Chem.* **1992,** *101*, 257-264.
44. Patschke, R.; Brazis, P.; Kannewurf, C. R.; Kanatzidis, M. G., $Cu_{0.66}EuTe_2$, KCu_2EuTe_4 and $Na_{0.2}Ag_{2.8}EuTe_4$: compounds with modulated square Te nets. *J. Mater. Chem.* **1999,** *9*, 2293-2296.
45. Beck, J.; Strahle, J., Complexes of 1,5-di(p-tolyl)-1,4-pentaazadien-3ide, crystal structures of $[Cu(tolyl\text{-}NNNNN\text{-}tolyl)]_3$ and $Ni[(tolyl(NNNNN\text{-}tolyl)_2]_2$ *Angew. Chem., Int. Ed. Engl.* **1985,** *24*, 409-410.
46. Savelsberg, G., Ternäre pnictide und chalkogenide von alkalimetallen und IB- bzw. IIB-elementen / On ternary pnictides and chalkogenides of alkaline metals and IB-resp. II B-elements. *Z. Naturforsch. B* **1978,** *33*, 370.
47. Klepp, K. O., Preparation and crystal structure of $NaCu_3Te_2$. *Z. Naturforsch. B* **1987,** *42*, 130-134.
48. Li, Y.; Liao, H.; Zhang, Z.; Li, S.; Jin, F.; Ling, L.; Zhang, L.; Zou, Y.; Pi, L.; Yang, Z.; Wang, J.; Wu, Z.; Zhang, Q., Gapless quantum spin liquid ground state in the two-dimensional spin-1/2 triangular antiferromagnet $YbMgGaO_4$. *Sci. Rep.* **2015,** *5*, 16419.
49. Clark, L.; Nilsen, G. J.; Kermarrec, E.; Ehlers, G.; Knight, K. S.; Harrison, A.; Attfield, J. P.; Gaulin, B. D., From spin glass to quantum spin liquid ground states in molybdate pyrochlores. *Phys. Rev. Lett.* **2014,** *113*, 117201.
50. Gladisch, F. C.; Steinberg, S., Revealing the nature of bonding in rare-arth transition-metal tellurides by means of methods based on first principles. *Eur. J. Inorg. Chem.* **2017,** *28,* 3395-3400.

Biographical Information

Adriana Paola Sotelo Munoz was born in Popayán, Colombia in 1987. She obtained his bachelor degree in Chemistry from Universidad del Cauca in 2009, the same year she moved to Medellin to pusue her Master Degree in Geomorphology and Soils (Soil Chemistry) in the Universidada Nacional de Colombia and graduated from here in 2012. After working in joint research projects between university and industry, She decided to pursue her doctoral degree in the United States and obtained her PhD in Chemistry from the University of Texas at Arlington in 2019. Her area of specialty is Solid State Chemistry and her research interests include: methodology development of new materials for optical and electronic applications. Her plans for the future are to work in the academy or industry to continue developing her research and solid state chemistry skills and apply them for the synthesis of new materials with significant applications.